Designing Bulk Metallic Glass Matrix Composites with High Toughness and Tensile Ductility

Thesis by

Douglas Clayton Hofmann

In Partial Fulfillment of the Requirements for the Degree of

Doctor of Philosophy

California Institute of Technology

Pasadena, California

2009

(Defended July 23, 2008)

Dedicated to my wife, Carrie.

No guilt in life, no fear in death—
This is the pow'r of Christ in me;
From life's first cry to final breath,
Jesus commands my destiny.
No pow'r of hell, no scheme of man,
Can ever pluck me from His hand;
Till He returns or calls me home—
Here in the pow'r of Christ I'll stand.

-Keith Getty & Stuart Townend

Acknowledgements

First and foremost, I could do nothing without my Lord and Savior, Jesus Christ. I am privileged to be a part of scientific research that reveals previously unknown aspects of His glorious creation.

I am forever indebted to my advisor, William Johnson, for everything that he has done to help me get to where I am. Bill is not only an amazing scientist with a thorough command of the natural world, he is also a caring advisor and a wonderful instructor. I will forever value our deep discussions on the roof of Keck.

The most under-appreciated member of our group, my officemate Jin-Yoo Suh, has been a vital part of my work at Caltech. Jin-Yoo is truly an amazing scientist with a broad range of expertise. With his background in metallurgy (specifically steel) his input has been crucial in my understanding of how to make BMG composites. Additionally, he is the only person who knows how to expertly operate and repair every piece of equipment in the lab. Jin-Yoo taught me how to use the SEM, which was the backbone of our paper in *Nature*, and the splat-quencher, which will result in our future success in iron-based BMGs. Most importantly, Jin-Yoo has done all of the fracture toughness measurements of my composites, which I consider to be the most difficult characterization method in materials science. His studious work is what has lead to the most important discoveries of our new alloys, ultra-high toughness. I am forever grateful for everything he has so selflessly done for me.

My colleague Aaron Wiest has been my closest friend in the group. He has assisted me in the lab countless times and we have done some amazing work together. I value our deep (non-scientific related) discussions in the lab.

Gang Duan and Mary-Laura Lind helped immensely with our work in Chapter 4. Gang's work on high fracture toughness BMGs was the backbone for our composite. We paired his alloy with soft crystalline dendrites to create the high toughness composites. Gang's drive to push the field in new directions was the foundation for my thesis. Mary-Laura was not only a great acquaintance, but also a very capable scientist. Her acoustical measurements are among the best data of its kind. Her work was vital in our understanding of how the dendrites need a low shear modulus.

I am also indebted to my other group members for their help in the lab and their deep discussion. Marios Demetriou has helped me edit and rewrite my papers but has also been invaluable in my scientific understanding of BMGs. I am proud to have worked with him in the lab. I also appreciate all of the technical help I have received from Joe Schramm, Glen Garrett, and Dale Conner throughout the years. I would also like to thank new graduate student Henry Kozachkov for his help with recent experiments. I could not have been so successful without the help of the entire Johnson group, past and present members. I also thank Carol Garland and Channing Ahn for their help with TEM.

I would like to acknowledge Paul Kim for his work in composites. My work in Chapter 4 was an extension of the alloys that he developed in his thesis work.

I am grateful for financial support from the Department of Defense through the NDSEG fellowship program. I also thank my committee: William Johnson, Brent Fultz, Guruswami Ravichandran, Harry Atwater, and Marios Demetriou. I appreciate the support and comments from my former advisor, Kenneth Vecchio.

I thank my entire family for supporting me through this long journey: my parents, Beth and Terry, my godmother Nancy, my sisters, Jennifer and Christy. I could not have done this without their love and support.

Last but not least, I thank my wife, the future Dr. Carrie Hofmann. Without her love and help, I would have been overwhelmed by despair on many occasions. She has helped me with my classwork, editing my thesis, and with technical problems. No one is as qualified in materials science as she is. "Behind every great man is a woman rolling her eyes."

Abstract

Metallic glasses have been the subject of intense scientific study since the 1960s, owing to their unique properties such as high strength, large elastic limit, high hardness, and amorphous microstructure. However, bulk metallic glasses have not been used in the high strength structural applications for which they have so much potential, owing to a highly localized failure mechanism that results in catastrophic failure during unconfined loading. In this thesis, bulk metallic glass matrix composites are designed with the combined benefits of high yield strengths and tensile ductility. This milestone is achieved by first investigating the length scale of the highly localized deformation, known as shear bands, that governs fracture in all metallic glasses. Under unconfined loading, a shear band grows to a certain length that is dependent on the fracture toughness of the glass before a crack nucleates and fracture occurs. Increasing the fracture toughness and ductility involves adding microstructural stabilization techniques that prevent shear bands from lengthening and promotes formation of multiple shear bands. To accomplish this, we develop in-situ formed bulk metallic glass matrix-composites with soft crystalline dendrites whose size and distribution are controlled through a novel semi-solid processing technique. The new alloys have a dramatically increased room-temperature ductility and a fracture toughness that appears to be similar to the toughest steels. Owing to their low modulus, the composites are therefore among the toughest known materials, a claim that has recently been confirmed independently by a fracture mechanics group. We extend our toughening strategy to a titanium-vanadium-based glass-dendrite composite system

with density as low as 4.97 g/cm^3. The new low-density composites rival the mechanical properties of the best structural crystalline Ti alloys. We demonstrate new processing techniques available in the highly toughened composites: room temperature cold rolling, work hardening, and thermoplastic forming. This thesis is a proven road map for developing metallic glass composites into real structural engineering materials.

Contents

List of Figures

List of Tables

Chapter 1
Why Should We Study Metallic Glasses?

1.1 Overview

The aim of this thesis is to ultimately understand and improve the tensile ductility and the fracture toughness of bulk metallic glass (BMG) composites. Much research has been done on BMGs and their composites and yet the new materials are still not being used in structural applications. Previous work has spanned many scientific fields from liquid theory to nanotechnology and yet currently BMGs are currently relegated primarily to niche applications. They are most useful in electronics for casings and small parts where expensive machining can be avoided through net shape casting. Herein, however, we report that significant toughening can be achieved by understanding the length scale of deformation in monolithic BMGs and then designing inclusions to exploit this length scale. Our discovery is that BMGs can be toughened on the microscale (as opposed to the nanoscale). This sharply contrasts with much of the current work in metallic glasses. Our hope is that with proper processing, BMGs will find structural applications that exploit their high strengths.

1.2 What is a Metallic Glass?

As we discuss extensively in this thesis, metallic glasses represent such a departure from traditional crystalline metals that their properties nearly defy description. A metallic glass is a metal alloy that contains an amorphous structure, rather than a crystalline structure, and is therefore a disordered solid. In a typical

crystalline metal, atoms are arranged in repeating crystalline lattices which extend until interrupted by another lattice at a different orientation, called a grain boundary. The bulk material is comprised of many grains and mechanical properties are connected to the size of these grains (at least in the case of low stacking fault energy materials [1]). To strengthen crystalline metal alloys, grain refinement methods have been used to reduce the overall grain size, creating nanocrystalline materials [1]. In the case where the grain size is sufficiently small (on the order of tens of nanometers) the difference in the definition between nanocrystalline metals and amorphous metals becomes ambiguous. For instance, an amorphous metal can be identified in X-ray diffraction experiments by observing broad diffuse haloes, in contrast to the sharp Bragg peaks observed in crystalline materials. However, if the grain size of a crystalline material is smaller than ~ 10 nm, a similar diffraction pattern is observed. One definition of an amorphous metal is a material that does not possess long range order; however nanocrystalline metals can sometimes satisfy this definition as well. From experimentation, metallic glasses contain short range order on the scale of about 2 nm. Although they don't have crystalline lattices, metallic glasses are comprised of loosely packed clusters containing approximately 200 atoms, which are usually referred to as "shear transformation zones." The mechanical properties and deformation mechanisms of a glass are inherently linked to these tiny clusters.

The previous definitions of short range order alloys allows us to refer to metallic glasses as "amorphous metals" and "disordered solids," but are they truly glasses? An amorphous metal can also be defined as a vitrified liquid; that is, a solid that has the structure of a liquid. Since the amorphous nature of the liquid is preserved

upon cooling to the solid state, amorphous metals can be further defined as "undercooled liquids" or more casually "liquid metals." We explore in the next section the glass transition, the characteristic feature of an amorphous metal, and the definition that allows us to refer to them as metallic "glasses."

1.3 Glass Transition

As we have seen, amorphous metals can be called disordered solids, undercooled liquids, vitrified liquids, non-crystalline solids, and liquid metals, among other terms. Much scientific research has been done to explore each of these unique definitions. In this section, we explore why amorphous metals are called metallic "glasses."

Conventional glasses contain many types of chemical bonding, which include covalent, ionic, hydrogen, van der Waals, and metallic. Obviously, amorphous metals, being comprised of metals and metalloids, exhibit metallic bonding.

If glasses are annealed at high enough temperatures, they will crystallize, indicating that they are metastable phases [2]. When a liquid cools, it will take the equilibrium state, minimizing the free energy. From thermodynamics, the free energy of a system can be defined as

$$G = H - TS\,, \tag{1.1}$$

where H is the enthalpy, T is the temperature, and S is the entropy. Several phases of one material exist so the equilibrium state that minimizes G is the stable form. Crystalline metals form close-packed structures and thus have lower enthalpy than amorphous metals, while the liquid state has more disorder and thus has higher

entropy. In a plot of Gibbs free energy versus temperature, both the liquid and the solid curves are concave down with negative slope. The melting temperature is defined as the point where the free energy of the crystal (x) and the liquid (l) are equal [3]. In other words, at T_m, $\Delta G_m = G_l - G_x = 0$. In addition, entropy is defined as $\Delta S_m = S_l - S_x = \Delta H_m / T_m$, where ΔH_m is the enthalpy of fusion. Above the melting temperature, the liquid has a lower free energy than the crystal and is the stable phase. Below the melting temperature, the crystal has the lower free energy and the liquid phase becomes metastable [2]. In the case where a liquid is undercooled so that it forms an amorphous solid, the structure is unstable. The difference in free energy between the undercooled liquid and the crystal is the driving force for crystallization. This can be defined as $\Delta G = \Delta G_m + \int_{T_m}^{T} (-\Delta S) dT = -\int_{T_m}^{T} \Delta S dT$. Therefore, all metallic glasses will crystallize if heated to sufficiently high temperatures.

The most prominent feature of a metallic glass is that it undergoes a glass transition, T_g, prior to crystallization [4]. Below T_g, a metallic glass can be thought of as an extremely viscous liquid. At T_g, the glass undergoes a transformation into liquid-like behavior marked by a rapid increase in the heat capacity (C_p), and several orders of magnitude decrease in the viscosity (η). Heat capacity is defined as the amount of heat energy it takes to raise the temperature of an object by a certain temperature, typically 1 °C. We can define T_g of a metallic glass by heating it at a rate of 20 K/min in a differential scanning calorimeter (DSC) until the increase in C_p is observed. With further heating, η continues to drop until the onset of crystallization at a temperature T_x. The temperature range between T_x and T_g is referred to as ΔT and represents a

thermal processing window. As we discuss in Chapter 5, between these two temperatures, a metallic glass has low viscosity and yet can still be vitrified, allowing for thermoplastic processing in some alloys.

1.4 Crystal Nucleation and Growth

This thesis primarily focuses on the formation and growth of specific crystalline phases in metallic glasses while simultaneously suppressing the nucleation of other, less desirable phases. It is therefore important to briefly discuss classical theory for nucleation and growth of crystals (see, for example [5]).

Both solidification and melting of metals occur by nucleation and growth. However, in the case of cooling a liquid, the process of nucleation is much more difficult than it is in the case of melting. As a result, metals do not significantly superheat, whereas almost all metals supercool to some extent. Depending on several factors, such as cooling rate and the presence of nucleation sites (called heterogeneous nucleation), liquid metals can be supercooled far below their solidification temperatures before nucleation and growth begin. Obviously, in the case where a liquid metal is supercooled below its glass transition temperature, nucleation will never occur and the supercooled liquid becomes a metallic glass. A supercooled liquid is in a metastable state and the free energy difference (ΔG) between the liquid and the crystal is the driving force for crystallization. As we have discussed, $\Delta G = 0$ at T_m, where $\Delta G_m = \Delta H_m - T_m \Delta S_m$. This leads to an equation for the change in entropy associated with crystallization, $\Delta S_m = \Delta H_m / T_m$. We can make the approximation that $\Delta G = \Delta H - T\Delta S \sim \Delta H_m - T\Delta S_m$. Plugging in for ΔS_m from above leads to another

expression for the nucleation driving force, $\Delta G = \Delta H_m \Delta T / T_m$. We notice that this expression is the approximate solution to the integral we presented in the previous section $\Delta G = -\int_{T_m}^{T} \Delta S dT$. Upon nucleation of crystals, the system's free energy changes as a result of the presence of the nuclei. The formation of a crystal is associated with a drop in free energy, which is a benefit in minimizing *G*, and is a function of the volume of the embryo. However, the formation of a crystal has a cost in *G* associated with creating a liquid-crystal interface. This increase in *G* is proportional to the surface area of the embryo. Therefore, if we assume a spherical shape for the nuclei, the free energy change associated with an undercooled liquid nucleating a crystal by homogeneous nucleation is defined as

$$\Delta G = 4\pi r^2 \sigma - \frac{4\pi}{3} r^3 \Delta G_v \tag{1.2}$$

where r is the radius of the nuclei, σ is the interfacial surface energy, and ΔG_v is the free energy difference between the crystal and the liquid per volume. As we have seen, the most stable form of a system is that which minimizes *G*, and yet there is a clear maximum in Equation 1.2. The increase in *G* associated with creating a new surface (which grows as r^2) is in competition with a decrease in *G* associated with crystallizing a volume element (which decreases as r^3). Above some critical radius r_c, crystal growth will be spontaneous because it lowers *G*. Below r_c, a crystal nuclei will not grow spontaneously because that would raise *G*. The critical nuclei size can be found by taking $\frac{d\Delta G}{dr}\Big|r_c = 0$. The critical nuclei and free energy maximum are

$$r_c = \frac{2\sigma}{\Delta G_v} \tag{1.3}$$

$$\Delta G_c = \frac{16\pi}{3}\left(\frac{\sigma^3}{\Delta G_v^{\,2}}\right). \tag{1.4}$$

Although it will not be discussed in detail here, further thermodynamic arguments are available to define crystal nucleation rate (I_v), crystal growth rate (u), volume fraction of the crystallized part of the undercooled liquid (f), and the time required to crystallize a certain volume of liquid (t). The crystal nucleation rate is defined as

$$I_v = \frac{A}{\eta}\exp\left(-\frac{16\pi\sigma^3}{3k_B T\Delta G_c^{\,2}}\right) \tag{1.5}$$

where A is a constant, η is viscosity, and k_B is the Boltzmann constant. Typically, the viscosity is defined as $\eta(T) = \eta_0 \exp\left(\frac{DT_0}{T - T_0}\right)$, where D is the diffusivity. Crystal growth rate can be defined as

$$u = \frac{k_B}{3\pi l^2 \eta}\left[1 - \exp\left(-\frac{n\Delta G_c}{k_B T}\right)\right] \tag{1.6}$$

where l is the average atomic diameter and n is the average atomic volume. The volume fraction of crystallized liquid can be written as

$$f = \frac{\pi}{3} u^3 t^4 I_v \tag{1.7}$$

where the time for a certain volume to crystallize, t, is found by solving this equation.

These few equations are the foundation for Time-Temperature-Transformation (TTT) diagrams, which are extremely useful for metallic glasses [6]. TTT diagrams indicate how long a liquid can be held at a specific temperature before crystallization occurs. For glass-forming alloys, the TTT diagram can be used to determine how fast the alloy must be cooled to avoid the onset (or nose) of crystallization (for creating bulk samples) and how long the sample can be held at a certain temperature before it crystallizes (which is useful for thermoplastic processing). A TTT diagram can be generated theoretically by solving the thermodynamic equations or it can be constructed experimentally by plotting multiple measurements of the time it takes to crystallize an alloy during an isothermal differential scanning calorimetry (DSC) scan. TTT diagrams are very interesting for alloy development and characterization but they fall outside the scope of this work.

1.5 Dendrite Growth

To accompany the section on crystal nucleation and growth, it is important to briefly discuss dendrite growth. The metallic glass composites making up the majority of this thesis form using dendrite growth, so it is important to explore their origin.

Dendrite growth is a type of crystalline growth that occurs when “the liquid-solid interface moves into a supercooled liquid whose temperature falls, or decreases, in advance of the interface” [7]. When the temperature falls in advance of a liquid-solid interface, the liquid becomes unstable, and crystals may grow from the solid interface into the liquid. This occurs when nucleation is poor, such that the liquid undercools before the solid forms. As the crystals grow, the latent heat of fusion is

conducted into the undercooled liquid, raising the liquid temperature towards the freezing point. The crystals will grow until the undercooled liquid increases in temperature to the solidification (or freezing) point. The structure of the crystals can be complex, with secondary and tertiary braches forming on the primary "trunk." The final structure resembles that of a pine tree and has been called *dendrite*, after the Greek word meaning "of a tree" [7]. The dendrite growth direction is <100> for the body centered cubic (b.c.c.) composites in this thesis. Dendrite growth occurs during the freezing of metals when the solid-liquid interface is able to move forward into sufficiently supercooled liquid. Typically, very large supercooling (about 100 K) is needed to freeze dendrites in pure metals. Dendrite nucleation and growth are both controlled by the cooling rate. For alloys cooled rapidly, dendrites are small and numerous (< 10 μm in size for some BMG composites). For alloys cooled slowly, dendrites are large and coarse (> 100 μm in some BMG composites).

1.6 Glass-Forming Ability

Bulk metallic glasses are created by successfully cooling liquid metal from above the melting temperature (T_m) to below the glass transition temperature (T_g) while avoiding crystal nucleation and growth, which is thermodynamically favored below T_m. As we have seen in the previous section, crystal nucleation and growth both require a finite amount of time to proceed. Obviously, if a liquid metal is cooled from T_m to below T_g at an infinitely high rate, the liquid will freeze as a glass because nucleation and growth will be completely suppressed. Of course, such a high cooling rate is impractical in the laboratory, and yet this does not prevent us from creating

bulk metallic glasses. As we will see in the next section, many factors, such as atomic size mismatch, contribute to the frustration of crystallization, leading to potentially millions of alloy compositions that can be frozen as glasses under practical cooling rates. For each glass-forming alloy composition there is a scheme to impede the formation of crystals. The better the scheme, the slower the cooling rate necessary to freeze the liquid into a glass. For each liquid metal, there is a critical cooling rate, denoted R_c, to create a glass during undercooling. The first metallic glass, created in $Au_{75}Si_{25}$ [8], was produced in ribbons by splat quenching. Splat quenching involves sandwiching a molten drop of liquid between two pistons, generating a cooling rate of approximately 10^6 K/s. This is the largest cooling rate that can be practically generated in the laboratory and typical sample sizes created by the method are only several microns thick. Many metallic glasses have such high R_c that splat quenching is the only method by which they can be produced. For alloys that have a low R_c, much thicker samples can be produced without resulting in crystallization. The center of a rapidly cooled ingot clearly has the slowest cooling rate and as long as it can be cooled to below T_g faster than R_c, the entire sample will be amorphous. The maximum thickness that a metallic glass sample can be cooled without crystallizing is referred to as the glass-forming ability (GFA). In weak glass formers it can be determined by splat quenching, in bulk glass formers it can be determined through copper-mold casting, and in highly processable glass formers it can be estimated through ingots cooled on one side in the arc melter. The best known glass former, $Pd_{40}Cu_{30}Ni_{10}P_{20}$ [9], has $R_c < 1$ K/s and has GFA of 7.2 cm. The best glass former made of practical

elements (those that are relatively low cost and easy to use), $Zr_{41.2}Ti_{13.8}Cu_{12.5}Ni_{10}Be_{22.5}$ (Vitreloy 1) [10–11], has a cooling rate of 1.4 K/s and has GFA of 2.5 cm.

The time it takes the center of a sample to cool to below T_g (which is inversely proportional to R_c) can be estimated experimentally by solving the one-dimensional Fourier heat flow equation (see, Haberman [12])

$$\frac{\partial T}{\partial t} = k\frac{\partial^2 T}{\partial x^2} \tag{1.8}$$

where T is the temperature, t is the time, k is the thermal diffusivity, and x is the spatial coordinate. The initial condition is that the alloy is at the liquidus temperature and the boundary conditions require room temperature at the edges (assuming a heat reservoir). The general solution can be written as

$$T(x,t) = \sum_{n=1}^{\infty} B_n \sin\frac{n\pi x}{L}\exp\left(-k\left(\frac{n\pi}{L}\right)^2 t\right). \tag{1.9}$$

Applying the boundary conditions, $T(x,0) = T_l$ (the liquidus temperature), and $T(0,t) = T(L,t) = T_r$ (room temperature), we obtain an equation for temperature as a function of time and of position

$$T(x,t) = T_r + \frac{4(T_l - T_r)}{\pi}\sum_{n=1}^{\infty}\frac{1}{2n-1}\sin\left[(2n-1)\frac{\pi}{L}x\right]\exp\left[-(2n-1)^2\pi^2\frac{kt}{L^2}\right]. \tag{1.10}$$

The centerline, $x = L/2$, has the slowest cooling rate so we can solve for temperature at the centerline as a function of time only

$$T\left(\frac{L}{2},t\right) = T_r + \frac{4(T_l - T_r)}{\pi}\sum_{n=1}^{\infty}\frac{-\cos(n\pi)}{2n-1}\exp\left[-(2n-1)^2\pi^2\frac{kt}{L^2}\right]. \tag{1.11}$$

We can use a first-order approximation to obtain the critical time it takes for the centerline to reach T_g. If this critical time is faster than the time it takes for crystal nucleation and growth to proceed above a critical size, then nucleation is suppressed. The critical time is defined as

$$t_c = \frac{L^2}{\pi^2 k} \ln\left(\frac{4}{\pi}\frac{T_l - T_r}{T_g - T_r}\right). \tag{1.12}$$

Therefore, the critical cooling rate, R_c, can be found by evaluating $R_c = \left(T_l - T_g\right)/t_c$. The critical cooling rate to create a bulk glass is

$$R_c = \frac{\frac{\pi^2 k}{L^2}\left(T_l - T_g\right)}{\ln\left(\frac{4}{\pi}\frac{T_l - T_r}{T_g - T_r}\right)}. \tag{1.13}$$

This equation tells us that the critical cooling rate to form a glass is a function of only the liquidus temperature, the glass transition temperature, the thermal diffusivity, and the length. GFA can be further defined as *critical casting thickness*, the critical length, L_c, where the centerline can be cooled to below T_g at the critical cooling rate. The critical casting thickness of a metallic glass is therefore

$$L_c = \sqrt{\frac{\pi^2 k\left(T_l - T_g\right)}{R_c \ln\left(\frac{4}{\pi}\frac{T_l - T_r}{T_g - T_r}\right)}}. \tag{1.14}$$

In Chapter 2, we focus on the weak glass forming binary alloy $Cu_{46}Zr_{54}$, which has L_c = 2 mm. In Chapter 3, we mainly focus on the ternary alloy $Cu_{47.5}Zr_{47.5}Al_5$,

which has L_c = 3 mm. In the later chapters, we focus only on highly processable BMGs based in the Zr-Ti-Be system with L_c > 1.5 cm.

1.7 Criteria Used to Develop Bulk Metallic Glasses

The majority of work in the metallic glass field has always centered on alloy development. In the scope of this thesis, the criteria used to create new glasses are useful in understanding the limitations observed while trying to create new composites. Many schemes are used to evaluate which systems will form bulk glasses. These include (but are not limited to) atomic size mismatch, confusion principle, deep eutectics, reduced glass transition temperature, and chemical interactions. We note that two of the strategies are useful for designing BMG composites: deep eutectics and atomic size mismatch.

First, we will briefly discuss the strategies that are not as useful for designing composite glasses. A large value of reduced glass transition temperature, defined as $T_{rg} = T_g/T_m$, is generally observed to lead to larger GFA [13]. A large T_{rg} leads to a lower nucleation rate and a smaller time window for crystallization. For BMG composites, the interaction between the inclusions and the glass matrix is the major design problem and the reduced glass transition temperature is not a practical strategy.

In another strategy it is observed that constituents that have a negative heat of mixing can lower the system's energy [14]. If the mixing effect is more prominent in the liquid than the crystal, the driving force for crystallization can be reduced and GFA can be enhanced. However, this empirical rule has been shown to have many exceptions and is not a practical strategy for designing composites.

The confusion principle, which states that the more elements in a liquid the more difficult it is to select a viable crystal structure [15], is an empirical rule with many exceptions. Clearly, most good glass formers are comprised of 4–5 elements and yet addition of further elements does not necessarily improve GFA. For example, Vitreloy 1, comprised of Zr-Ti-Cu-Ni-Be is an optimal composition, based on other criteria for GFA. Further additions of elements actually reduce GFA, which contradicts the confusion principle. In fact, the discoveries of binary bulk glasses in the Cu-Zr system prove that good glass forming can be achieved without numerous elements. In the Pd-Si binary system, 6 mm glasses can be obtained, representing larger GFA than many systems with five or more elements.

We have observed that the two most important criteria for bulk glass formation are deep eutectics and atomic size mismatch. Good glass-forming systems can be found by first looking at binary phase diagrams for deep eutectics. The deeper the eutectic, the easier it is to cool a liquid below T_g without allowing enough time for crystal nucleation and growth. Figure 1.1 is a binary phase diagram of Cu-Zr, which exhibits several deep eutectics. These eutectics are so prominent that three compositions, $Zr_{65}Cu_{35}$, $Cu_{46}Zr_{54}$, and $Cu_{50}Zr_{50}$, lead to the formation of bulk glasses. All bulk metallic glasses are based in systems that have deep binary eutectics between two constituents. Examples of deep eutectics are Pd-P, Pt-P, Au-Si, Pd-As, Pt-As, Zr-Be, Ti-Be, Cu-Ti, Cu-Zr, Ni-Ti, Ni-Zr, Pd-Si, Cu-P, and Fe-P. Figure 1.2 and Figure 1.3 show binary phase diagrams from Zr-Be and Ti-Be, which are the basis for the glass forming systems used in this work. In many cases, by combining several alloys that all exhibit binary eutectics, even lower melting temperatures can be achieved. For

instance, despite deep eutectics in Zr-Be and Ti-Be, bulk glasses cannot be created in those systems. However, by combining the three elements, Ti-Zr-Be glassy alloys can be created up to 6 mm thick [17]. With additions of Cu and Ni, glass forming increases to 2.5 cm and melting temperatures can dip as low as ~ 900 K. Practical metallic glasses (those that don't use precious or expensive metals) are typically comprised of elements such as Zr, Ti, Cu and Ni. To design highly processable BMG composites, this work deals solely with the Ti-Zr-Cu-Be system as its base.

Atomic size mismatch is the last constraint used to determine GFA. Elements that exhibit large differences in atomic size produce lattice stresses that increase the energy of the crystalline phase. Like the other strategies, there are many exceptions to this rule. Boron, for instance, is a very small metalloid that appears to be an excellent addition to some Zr and Ti-based alloys and yet it never seems to improve GFA. The most important contribution of atomic size mismatch is that a highly processable BMG made from practical elements cannot be made without mismatch or deep eutectics. The optimal combination of both is $Zr_{41.2}Ti_{13.8}Cu_{12.5}Ni_{10}Be_{22.5}$ (Vitreloy 1) [10]. In this alloy, Cu, Ni, and Be all exhibit extremely deep eutectics with Zr and Ti. Additionally, Be is a small metalloid which allows for pronounced atomic size mismatch between the other elements. As a result, GFA is on the order of 2.5 cm. The only practically based highly processable glasses that do not contain Be are $Zr_{57}Nb_5Cu_{15.4}Ni_{12.6}Al_{10}$ and $Zr_{52.5}Ti_5Cu_{17.9}Ni_{14.6}Al_{10}$, Vitreloy 106 and 105, respectively (see X. Lin, Caltech thesis, 1997). In these non-beryllium alloys, the deep eutectic obtained from Zr-Be and Ti-Be is absent, raising the melting temperature by ~ 200 K over Vitreloy 1. However, these alloys contain the small metalloid Al, which

increases GFA substantially, even though it raises the melting point of Ti. Vitreloy 105 and 106 utilize the strategy of atomic size mismatch but don't utilize the deep eutectic found in Be-containing alloys. Thus, GFA is reduced to ~ 1.5 cm. Additionally, without the oxygen-gettering affects of Be, these alloys are extremely prone to crystallization [18]. GFA is severely reduced when the oxygen content exceeds ~ 500 parts per million. Vitreloy 1, 105, and 106 are all considered to be highly processable, since they can be produced in ingot form. As we discuss in Chapter 6, small additions of Al dramatically increase the shear modulus of BMG composites, which eliminates ductility. To create highly processable BMG composites we require bulk glasses that don't contain a substantial amount of Al. Thus, our current composites are limited to Be-containing alloys. No highly processable BMGs made from practical elements currently exist which do not contain Be or Al.

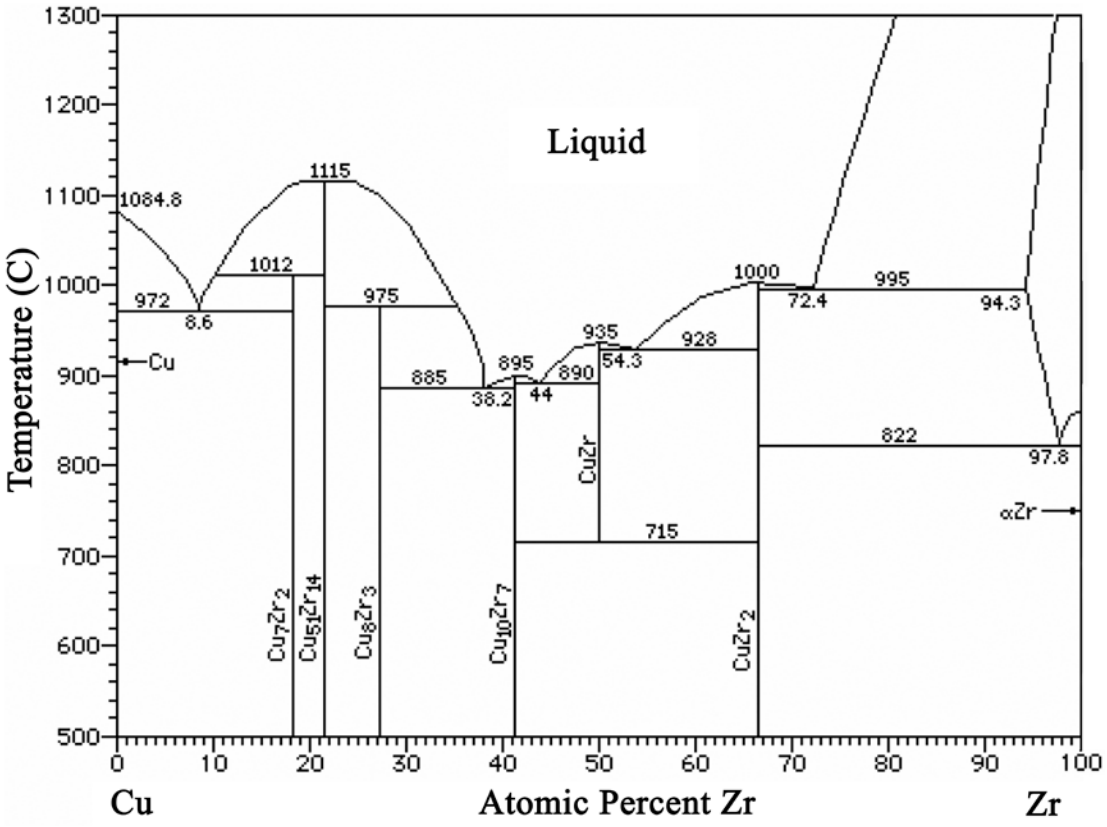

Figure 1.1 – Binary Cu-Zr phase diagram (adapted from [16]). The Cu-Zr eutectic temperatures are so deep that three binary bulk glasses form near 38.2%, 44%, and 54.3% zirconium. The best glass former, $Cu_{46}Zr_{54}$, can be cast up to 2 mm in diameter.

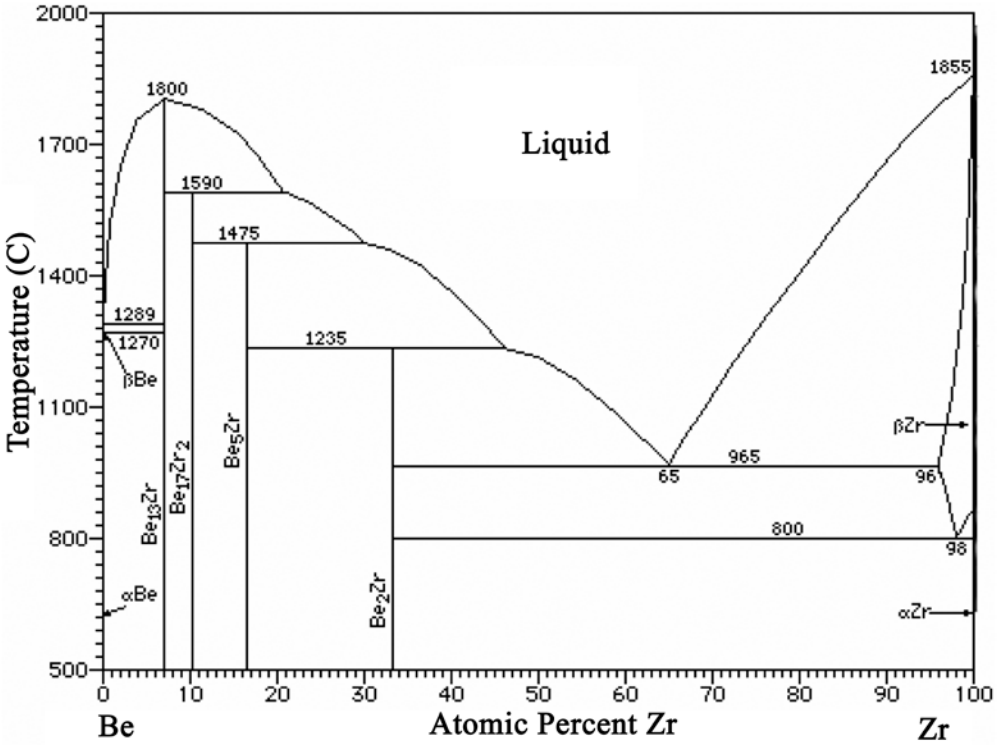

Figure 1.2 – Binary Zr-Be phase diagram (adapted from [16]).

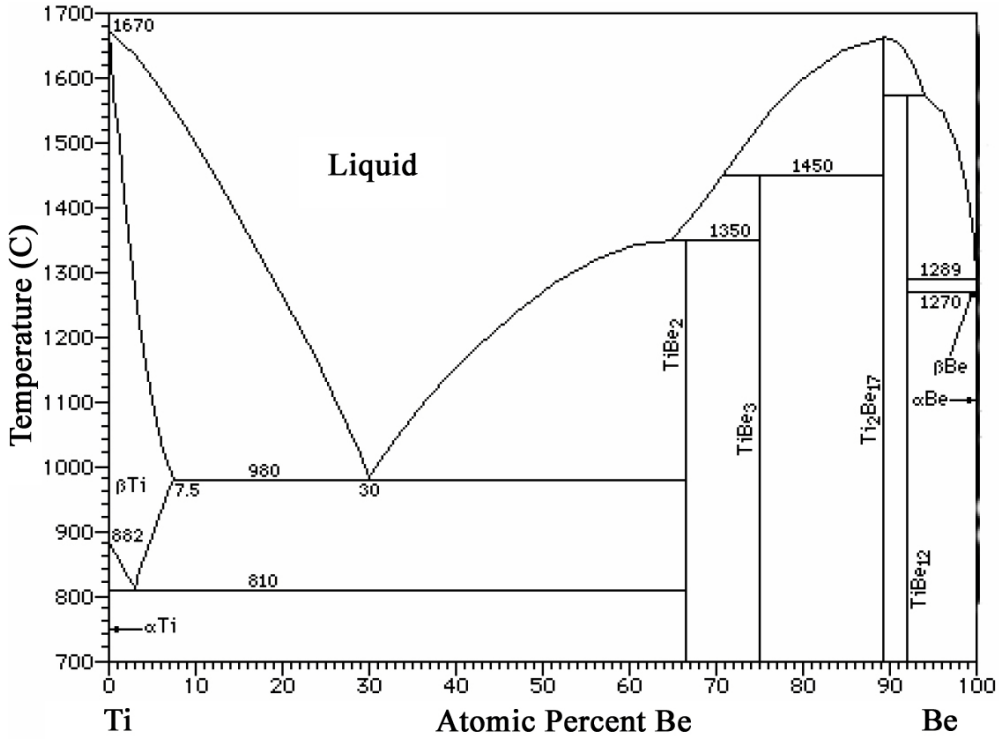

Figure 1.3 – Binary Ti-Be phase diagram (adapted from [16]).

1.8 Mechanical Testing of BMGs

Without question, mechanical testing, specifically the uniaxial compression test, is the single largest pitfall of BMG research. The problem with mechanical testing arises from the inherent nature of BMGs. Despite thousands of reported compositions that form bulk glasses, almost all of them possess mechanical properties that fall within a narrow window. Nearly all BMGs exhibit high strength, large elastic limit, high hardness, and zero tensile ductility in bulk dimensions. Many BMG publications rely on uniaxial compression tests because all monolithic BMGs look similar under tensile loading. This section demonstrates some of the problems associated with compression tests and motivates the tension tests used in Chapters 4–6.

BMGs have been created in many different alloys systems including Zr, Ti, Fe, Au, Pt, Pd, Cu, Ni, La, and Cs. Although some of these systems show unique mechanical properties (such as low strength in La-based glasses and high strength in Fe-based glasses), the mechanical properties of the majority are similar. Despite any observed differences in the mechanical properties of BMGs, they all have one feature in common: they lack any global tensile ductility. No monolithic BMG has ever demonstrated more than a 0.5% global ductility in uniaxial tension tests (at ambient temperature with standard strain rates). This implies that monolithic BMGs are brittle in tension (despite the fact that BMGs will exhibit tensile ductility at high strain rates [19], elevated temperatures [20], and on the nano scale [21]). This is a direct result of the fact that BMGs do not possess a crystal structure, and thus cannot deform by dislocation-based plasticity. This feature simultaneously leads to unprecedented strength and catastrophic failure when overloaded. BMGs exhibit a highly localized

strain-softening phenomenon manifested through shear bands. At the yield strength, a significant amount of deformation in a BMG is localized in narrow bands that nucleate and grow from the shear transformation zones (STZs). Shear bands exhibit large increases in temperature, which some researchers suggest is far above the melting temperature of the material [22]. Deformation in a shear band can be quite large but is limited to perhaps tens of nanometers in width, leading to very limited global ductility. Plasticity in BMGs results from arresting the persistent slip of one shear band and nucleating another. Since monolithic BMGs do not possess a microstructure or other stabilizing features, a slipping shear band under uniaxial tension is difficult to arrest. A shear band that forms under tensile stresses can simply extend without limit until it reaches a critical dimension (determined by the fracture toughness of the glass) before nucleating a cavity and opening failure occurs [23]. Failure in tension typically occurs at 45° to the loading axis, in the direction of the maximum resolved shear stress. Therefore, plasticity, in the sense of forming multiple shear bands, does not occur in tension tests of BMGs. As we explore in Chapter 4, without microstructural stabilization obtained through composites, BMGs should theoretically never display a significant amount of tensile ductility. During different scientific studies of BMGs, tensile ductility has been obtained in modified experiments. High strain rate tension tests (above the 0.1 mm/s standard) were used on Vitreloy 1 to obtain tensile ductility (see, for instance, [19]), elevated temperatures (above T_g) were used to achieve superplasticity in monolithic BMGs [20], and ambient temperature tensile ductility was obtained during in-situ TEM studies of BMG beams that were nanometers in width [21]. In structural applications, where samples larger than 1 mm are used at

ambient temperatures under normal loading configurations, BMGs are brittle materials that fail with no visual precursors. This makes them unacceptable for structural engineering applications. Thus, until now, BMGs have largely been relegated to niche applications that exploit their other unique features, not their strength.

As we discuss in Chapter 3, three-point-bending tests are an excellent way to compare the toughness of BMG materials. Unlike uniaxial tension tests, which all look similar, BMGs can behave very differently in bending. In Chapter 3 we note that bending tests possess a tensile and compressive surface, which in some thicknesses allows a BMG material to arrest slip on a single shear band and generate multiple shear bands. This work has lead to some of the best studies of how plasticity occurs at the bulk scale in BMGs. In literature, bending tests are rarely done because of a dramatic size effect that occurs. Bending is directly related to fracture toughness, and in the case of monolithic BMG materials, fracture toughness is typically so low that beams cannot be bent significantly at thicknesses greater than 1 mm. As a result, researchers commonly resort to the uniaxial compression test alone for all of the mechanical characterization of newly created BMGs. However, that test also has a size effect whereby smaller samples exhibit larger plasticity.

Arguably the most important application of materials science is “material selection for mechanical design” [24]. To properly select the best possible material for a specific application, many design criteria must be taken into account. For example, in structural applications materials must fit the requirements for strength, stiffness, corrosion, fatigue, fracture toughness, density, ductility, and cost, among many others [24]. For a specific application, some materials exhibit “enhanced mechanical

properties" over other suitable materials and this contributes to their selection. In metallurgy research, the mechanical properties of a new material must be evaluated and compared with known materials to observe if any improvements in properties come with the deterioration of other properties. Pros and cons are weighed and the material with the best balance of peformance and cost is selected. As an example of how mechanical properties could be misreported, it would be incorrect to claim that ceramics have enhanced mechanical properties over titanium alloys simply because they have higher strengths. Titanium alloys have higher ductility, fracture toughness and they exhibit graceful failure, unlike the catastrophic failure observed in ceramics. For a high strength structural application, like in an airplane, titanium alloys are much better suited than ceramics. Unfortunately, in the field of BMGs, similar claims about "enhanced mechanical properties" appear in many papers where compression tests are the only mechanical characterization techniques used.

The mechanical properties of many BMG materials have been misrepresented in literature owing to the uniaxial compression test, where small cylinders are compressed between two parallel plates. The difficulties associated with compression tests are numerous, yet these tests are useful for determining the compressive yield strength of a material, among several other properties. First, special consideration must be taken during compression testing to assure that high strength materials do not indent or plastically deform the machine platens. Very hard WC platens are often used to counter this effect [1]. Lubrication between the specimen and the platens is also very useful to decrease nonuniform deformation, called barreling in compression [1]. This happens when friction causes the sample's surface to "stick" to the platens,

forcing the sample to bulge out in the middle. The most important consideration for ceramics and BMGs is homogenous loading, since they fail predominantly in the elastic range. A desirable compression sample has no height difference but in practice this is not possible to achieve. If a cylindrical specimen has a height difference of $\Delta h = h_2 - h_1$, then the higher side will have stress $\sigma = E(\Delta h/h_2)$ before loading even begins on the lower side. Meyers and Chawla [1] give an example of this problem in Alumina, for which E = 400 GPa, h = 10 mm, and σ_f = 4 GPa. The strain at failure is $\varepsilon_f = \sigma_f / E = 10^{-2}$, which corresponds with a displacement of $\Delta h = \varepsilon_f h = 0.1\,\text{mm}$. Therefore, in a 10 mm long cylindrical sample of alumina, the change in height must not be greater than 0.1 mm or the higher side will fail before the lower side is loaded. If the surfaces of the compression sample are not flat, stress inhomogeneities will arise which can drastically alter the stress-strain curves, leading to apparent plasticity. In BMG research, sample dimensions for compression are often very small, usually limited by critical casting thickness. Typical compression test dimensions are 2 mm in diameter by 4 mm long, but many papers report tests done at 1 mm diameter by 2 mm long. In Vitreloy 1, for example, E = 95 GPa, h = 2 mm, and σ_f = 1.9 GPa. This leads to $\varepsilon_f = \sigma_f / E = 0.02$ and $\Delta h = \varepsilon_f h = 0.04\,\text{mm}$. This means a 1 mm diameter compression test must have a variation in height less than 40 μm to assure homogeneous loading. For the more common 2-mm-diameter compression test, the variation in height must be less than 80 μm. For samples being polished by hand on sandpaper, as is the common practice, such precision is extremely difficult to acheive. In practice, height differences of less than 0.1 mm are impractical to obtain and are

usually overlooked. For Vitreloy 1, compression tests should be larger than 3 mm in diameter to assure that tolerable differences in sample height can be obtained by mechanical polishing.

The most common problem associated with compression testing of BMG materials is the sample dimensions, usually a result of poor glass-forming-ability. Commonly, compression tests are performed on alloys with identical compositions but in different dimensions. For example, the binary BMG $Cu_{50}Zr_{50}$ was demonstrated to have 52% strain to failure in a 1-mm-diameter compression test [25], 11.5% in a 1.5 mm test [26], and 3.7% in a 2 mm test [27]. Clearly, vastly different values of compressive plasticity were obtained for the same alloy. This makes it challenging to compare BMGs compressed at different dimensions. How does one decide which alloy is better, a BMG that exhibits 10% plasticity in a 3 mm diameter or a BMG that exhibits 20% at 1 mm? Currently, several papers are being published discussing the shortfalls of compression tests to avoid misunderstanding the mechanical properties of BMGs. One such paper was recently published by Xie and George [28], where the effect of sample size in compression was investigated. The Vitreloy 105 BMG, developed at Caltech in the 1990s by X. Lin, was demonstrated to have extensive plastic strain in 1.35 mm diameter compression tests. However, at 6.5 mm in diameter, plastic strain is totally absent [28]. In addition to problems with obtaining plane parallelism in small samples, mechanical tests are usually performed on large testing machines capable of doing high-strength tensile tests. The BMG compression tests are so small relative to the testing equipment that the results can be overwhelmed by machine compliance issues, among others. In general, it seems unwarranted to claim a

material is suitable for structural applications when the only supporting test is a 1-2 mm diameter compression sample.

Recent results from compression tests were used in a high-profile BMG publication in *Science* [29]. The work reported room-temperature superplasticity in a Zr-Cu-Ni-Al alloy. Superplasticity occurs when a material exhibits positive strain-rate sensitivity (that is, the increased strain rate causes increased flow stress in the neck region during tension testing). When this occurs, necking is inhibited and plastic strain dramatically increases, sometimes into the thousands of percent. In this paper, 2 mm compression tests were used to claim room temperature superplasticity of up to 160%. There are several problems with such a claim, most of which are common in BMG literature. The undeformed compression specimen is not plane parallel (the top of the sample appears flat but the entire cylinder is leaning to the left, indicating major height change in the bottom surface). Therefore, the sample was loaded in an inhomogeneous state of stress. Above the flow stress, shear bands form under the compressive stress. Slip is hindered by friction and multiple shear bands nucleate and grow until they span the sample, usually occurring at ~ 25% strain. After 25% strain the sample shows clear signs of barreling, indicating that nonuniform plastic deformation has occurred from friction between the sample and the testing platen. In the stress-strain curve for the compression test, the curve changes from concave down to concave up at ~ 25% strain, corresponding exactly with the sample barreling. Since shear bands had previously spanned the sample, the sample has already failed. A continuous flaw through the sample implies the sample has failed, even though friction from the platens holds the sample together. The test should have been terminated at this point.

With the sample completely confined, friction prevented the sample from fracturing and it was flattened to 160% strain. Similar compression tests, with nearly identical stress-strain curves, are shown in many prominent BMG papers [29–35]. Although extensive amounts of plasticity are observed in compression, the monolithic BMGs fail catastrophically in tension.

In the uniaxial tension test, frictional forces are absent and BMG samples do not possess a stabilization mechanism to prevent the lengthening of a shear band. This problem is not without a solution, however. Results dating back to C. Paul Kim's work at Caltech in 2001 have demonstrated that ductile-phase in-situ metallic glass composites (with crystalline inclusions embedded in a glass matrix) can result in tensile ductility [36–37]. The current work demonstrates that with fundamental understanding of how BMGs fail in tension, composites can be designed with all the beneficial features of the monolithic metallic glass (high yield strength, elastic limit, low processing temperatures, etc.), but with significant tensile ductility.

1.9 Theoretical Yield Strength

The most common motivation for scientific studies involving BMGs is that they possess "nearly theoretical yield strengths." Since this is the most important feature of a glassy metal, we discuss in this section the Orowan model for theoretical tensile strength (described in [1]).

When a material is pulled in tension and fails perpendicular to the applied stress, cleavage has occurred. Orowan's model, published in 1949, does not take into account the effects of material imperfections or instabilities (such as necking) but

rather calculates the stress at which a perfect lattice will cleave. Therefore, the theoretical yield strength, by Orowan's description, is the theoretical cleavage stress of a material. We know now that stress concentrations at the tip of a crack control fracture, but in the model, all atoms are assumed to separate simultaneously. Once a critical value of separation is reached (called d) the atomic bonds are broken, two new surfaces are created, and cleavage occurs. Figure 1.4 shows that a plot of stress versus increasing atomic separation is roughly a negative parabola. It requires an increasing amount of stress to separate the atoms until a maximum is reached, after which stress falls to zero as the bonds are broken. In Orowan's model, the curve is assumed to be a simple sine wave and the area under the curve is the work necessary to cleave the crystal. Stress as a function of atomic separation can be written as

$$\sigma = K \sin \frac{2\pi}{2d}\left(a - a_0\right) \tag{1.15}$$

where K is a parameter related to Young's modulus, d is the critical separation, a_0 is the original separation, and a is the final separation. K can be determined by differentiating the stress equation with respect to a and then relating that to Young's modulus. It can be easily shown that $K = \frac{E}{\pi}\frac{d}{a_0}$. The unknown critical separation, d, can be determined by equating the area under the stress-separation curve with the surface energy of the two new surfaces created. In this manner, d can be related to surface energy, γ, through $d = \frac{\pi\gamma}{K}$. The maximum value of stress is when

$a = a_0 + d/2$. Plugging in these values we obtain the theoretical yield strength of a material

$$\sigma_{theoritical} = \sqrt{\frac{E\gamma}{a_0}}. \tag{1.16}$$

The surface energy can be rewritten in terms of the other parameters such that $\gamma = \frac{E}{a_0}\left(\frac{d}{\pi}\right)^2$. It can be shown experimentally that d is approximately equal to a_0 so a simplified equation for theoretical yield strength is

$$\sigma_{theoretical} \cong \frac{E}{\pi}. \tag{1.17}$$

This equation tells us that crystals should exhibit yield strengths that are approximately one third of their Young's modulus. Most common engineering metals have $E \sim$ 100–200 GPa, so this implies that they should have theoretical strength on the order of tens of gigapascals. In reality, most crystalline metals have yield strengths between 100–1000 MPa (or 0.1–1.0 GPa), far below the theoretical value. The discrepancy occurs because crystals contain imperfections and atomic cleavage (where every bond is broken simultaneously) does not occur. Real crystalline metals fail through motion of dislocations, which become mobile at stresses far below the theoretical yield strength. Additionally, the entropy of mixing tells us that even in thermodynamic equilibrium, a crystal will contain a finite number of point defects. Using statistical mechanics, the equilibrium number of vacancies of a material is

$$\frac{n}{N} = \exp\left(\frac{-G_f}{kT}\right) \tag{1.18}$$

where n is the number of vacancies, N is the number of vacancy sites, G_f is the free energy associated with the formation of a vacancy, k is Boltzmann's constant, and T is the temperature.

In metallic glasses, crystal structures are absent and common imperfections such as point, line, and surface defects are not responsible for plasticity. Deformation occurs through a strain softening phenomenon at stresses typically much higher than the yield strength of crystalline metals. BMGs typically exhibit low Young's modulus (< 100 GPa) and thus have very low theoretical yield strengths in comparison to many crystalline materials. Since they have high experimental yield strengths, the difference between the actual yield strength and the theoretical yield strength is often quite small. For example, Vitreloy 1 exhibits about 1/15 or ~ 7% of its theoretical yield strength.

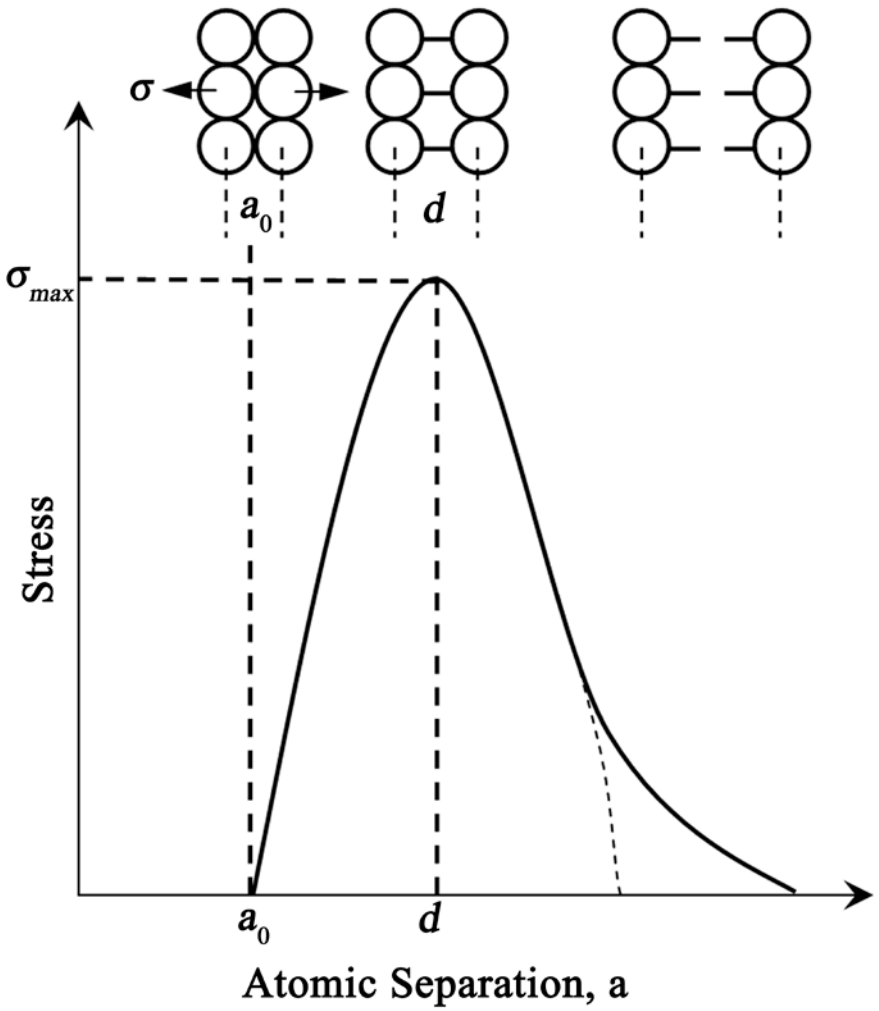

Figure 1.4 – Plot of stress versus atomic separation of atoms for cleavage in Orowan's model of theoretical cleavage strength. In the model, all of the atomic bonds are broken simultaneously, leading to a high value for yield strength. Experimentally, dislocations cause yielding at stresses far below the theoretical cleavage stress.

1.10 Metallic Glass Composites

The concept that metallic glasses are inherently brittle materials was first recognized shortly after their invention. Many researchers quickly recognized the need for BMG composites to decrease brittleness and catastrophic failure in unconfined loading. Among the first BMG composite papers was “A metallic glass-metal matrix composite,” published in 1982 [38], which surprisingly, was published over a decade before the invention of Vitreloy 1 in 1993 [10]. By the early 1990s, several research groups were exploring BMG-metal matrix composites, in which metallic glasses and crystalline metals were combined into a composite structure. Since then, hundreds of papers have been published exploring the mechanical properties of BMG composites.

A thorough investigation of literature indicates that almost all BMG composite materials fall into two categories: ex situ and in situ. The ex-situ composites, which account for a vast majority of published papers, involve mechanically combining a glass forming alloy with another material such that the glass matrix structure is interrupted by the inclusions. These composites are typically manufactured by casting a glass-forming liquid over crystalline wires or particles such that a continuous matrix of metallic glass remains. Among the most common wire reinforcements are W, Ta and Nb, while the most common particle reinforcements are hard carbides such as WC or ZrC. The number of ex-situ composites found in literature is extensive and yet the mechanical properties of the vast majority of them are typically not better than the monolithic glasses. Ductility is sometimes achieved but usually at the cost of strength. The problem with ex-situ BMG composites is very simple, yet often overlooked. The

interface between the BMG matrix and the inclusion determines how the composite will fail during unconfined loading. In the case of particulate reinforced BMGs, brittle materials such as carbides are often used to arrest shear band growth. Since compression tests are typically used to evaluate the mechanical properties of the composites, apparent toughening seems to occur. However, as we have seen, frictional forces combined with closing stresses on shear bands lead to plasticity in compression that is not present in unconfined loading geometries. As we know now, ex situ particle-reinforced BMGs are far more brittle that monolithic BMGs in bending or tension tests because of the interface between the glass and the particles. During unconfined loading, the particles simply separate from the matrix and shear bands grow uninterrupted. Additionally, the particles often act as stress nucleation sites for shear bands to form, which lowers the overall strength of the material. Recent work in our own group has shown that in the case where soft particles are used instead of carbides, oxide layers on the particles cause brittle interfaces between the particles and the glass matrix, and similar catastrophic failure is observed.

Our group's recent work has also demonstrated that wire-reinforced BMGs have improved bending and tension tests over particle-reinforced BMGs given that the wires are continuous through the matrix. If tensile loading occurs in the direction of the wires, shear bands must sever the wires for failure to occur. Unfortunately, since the wires are continuous, these alloys often have low strength, and interfacial effects usually cause the wires to "pull out" during tension tests. In addition, it is challenging to produce a fully dense composite using wires, and the final composite is highly anisotropic.

The largest success in the toughening of BMGs came in 2001 with the introduction of a ductile-phase in-situ metallic glass matrix composite [36]. These alloys, developed by Caltech graduate student C. Paul Kim, are comprised of a two-phase microstructure of glass and soft b.c.c. dendrites that nucleate and grow during the rapid cooling. The composite structure was originally obtained by simply increasing the amount of Zr in Vitreloy 1 (which has composition $Zr_{41.2}Ti_{13.8}Cu_{12.5}Ni_{10}Be_{22.5}$) at the expense of Cu, Ni, and Be (holding Ti constant). In Vitreloy 1, the sum of the atomic percentages of Zr-Ti is 55% and when this sum reaches ~ 70% a two-phase composite structure forms, with dendrites growing from the liquid. This in-situ composite is unique because it represents an equilibrium system. That is, the same volume fraction of crystalline phase (determined by the Lever Rule) is obtained in the final alloy regardless of cooling rate. The two-phases form due to the extremely low solubility of Be, Ni, and Cu in b.c.c. Ti and Zr, and if the alloys are designed correctly, the eutectic phase vitrifies upon rapid cooling. Owing to the low solubility of several elements with the crystalline dendritic phase, the volume fraction of the b.c.c. phase can be increased by simply increasing the ratio of Zr and Ti. Figure 1.5 is a pseudo-phase diagram reproduced from S-Y Lee's Caltech 2005 thesis, showing the formation of an in-situ Zr-Ti-Nb-Cu-Ni-Be BMG composite. The diagram has the monolithic glass Vitreloy 1 on the left axis, the monolithic b.c.c. alloy on the right axis, and the matrix composite at a composition between the two.

Both the in-situ composites and some particulate reinforced ex-situ BMG composites exhibit compressive plasticity but zero global tensile ductility. The

advancement that allowed in-situ alloys to exhibit tensile ductility while ex-situ alloys do not is the understanding that the inclusions need to be softer than the glass matrix [23]. This fundamental concept was experimentally demonstrated in 2001, with the alloy $Zr_{56.2}Ti_{13.8}Nb_5Cu_{6.9}Ni_{5.6}Be_{12.5}$ (LM2), but the concept was largely overlooked. Since the focus of most BMG papers has always been on the compression test, the effect of a soft, ductile inclusion was hardly exploited. The success of LM2 stems from the use of the β-stabilizer Nb to reduce the shear modulus of the b.c.c. phase. To illustrate this concept, C.P. Kim demonstrated two in-situ composites in his Caltech thesis. In one alloy, he melted Vitreloy 1 with an ingot of Ta in the plasma arc melter to create a two-phase composite of Vitreloy 1 and Ta dendrites. In the other alloy, he created LM2 by adding 5 atomic % Nb to a composite with a Zr+Ti ratio of 70%. In the Ta composite, no toughening or tensile ductility was observed, owing to the high shear modulus (G) of Ta relative to the glass matrix ($G \sim 60$ versus 30 GPa). In LM2, an electronic softening phenomenon was observed in Zr-Nb which lowered G to ~22 GPa. As we discuss in further detail in Chapter 4, shear band growth can be arrested by deformation in the softer phase. Two tension tests of LM2 made from different processing methods are shown in Figure 1.6, along with the tension test from Vitreloy 1. Note that the tensile behavior of the composites is different even though the alloys are the same. This indicates that processing plays a major role in the mechanical properties of in-situ composites, a concept that is exploited heavily later in this thesis.

Many attempts in literature have been made to create in-situ composites that match the mechanical properties of LM2. Although two papers were originally published on LM2 [36–37], the concept that a soft inclusion is needed was not well

understood. Ductility in tension was achieved by Yi Li's group in 2005 when pure La was precipitated as a dendrite in a LaAlCuNi alloy [39]. As we show in Appendix A, pure La has a shear modulus slightly lower than the La-based metallic glass. Another in-situ composite created by Todd Hufnagel's group demonstrated slight tensile ductility in a Ta-reinforced alloy owing to crack bridging.

Other attempts have been made to create in situ BMG matrix composites. In one attempt, an in-situ glass/b.c.c. composite was generated without lowering the shear modulus of the dendritic phase, leading to a brittle alloy. This alloy was developed to try to create an in-situ composite out of the non-Be alloy Vitreloy 106, much in the same way LM2 was created from the BMG Vitreloy 1. Two papers were published on this alloy, $Zr_{66.4}Nb_{6.4}Cu_{10.5}Ni_{8.7}Al_8$, one in 2002 [40] and one in 2004 [41]. In both cases, the papers refer to the alloy as having a "ductile b.c.c. phase," which is technically true since the monolithic dendritic phase was exhibited to have tensile ductility. Unfortunately, owing to the presence of 10 atom% Al in the original alloy, the dendritic phase has composition $Zr_{74.5}Nb_{7.7}Cu_{7.3}Ni_{1.1}Al_{9.3}$, which we now know has $G > 40$ GPa, while the glass matrix has been measured to have $G = 30.8$ GPa. As expected, no tensile ductility is reported in either paper, and only moderate amounts of plastic strain in compression is observed [40,41]. Additionally, this alloy has a dendritic phase on an extremely small scale which also contributes to the poor properties.

In another attempt at an in situ composite, the dendrite was designed to be soft by adding b.c.c. stabilizers and removing aluminum, but the glass matrix crystallized. These "nanoeuctectic" alloys are actually not as tough as monolithic BMGs (because a

crystallized BMG is *always* more brittle than a monolithic one) and yet compression tests indicate that enhanced plasticity occurs. This work has spawned a new field of research on nanocrystalline in situ composites. However, these alloys are very brittle and exhibit no tensile ductility, something that is noticeably absent from numerous publications. A further discussion of these alloys appears in Chapter 6.

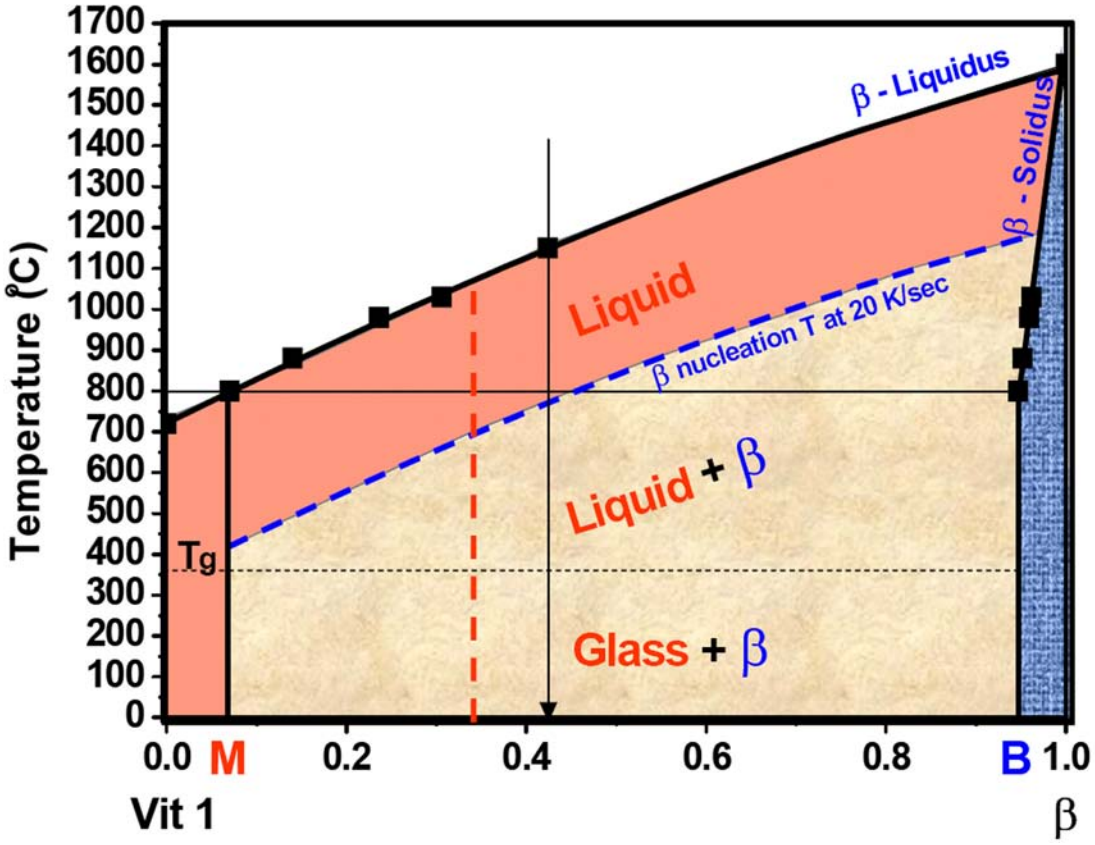

Figure 1.5 – Pseudo phase diagram of a metallic glass composite (courtesy of S.-Y. Lee, Caltech thesis, 2003). The value *M* represents the limit of solubility of the β phase crystalline alloy within the glass forming compositions. The blue line represents the nucleation of the dendritic phase. At compositions below the blue line and between *M* and *B*, an alloy will decompose into a composite with dendrite *B* and glass matrix *M*. In this system, *M* is $(Zr_{75}Ti_{25})_{55}(Be_{50}(Cu_{55}Ni_{45})_{50})_{45}$, while *B* is $Zr_{75}(TiNb)_{25}$. $(Zr_{75}(TiNb)_{25})_{75}$ $(Be_{50}(Cu_{55}Ni_{45})_{50})_{25}$.

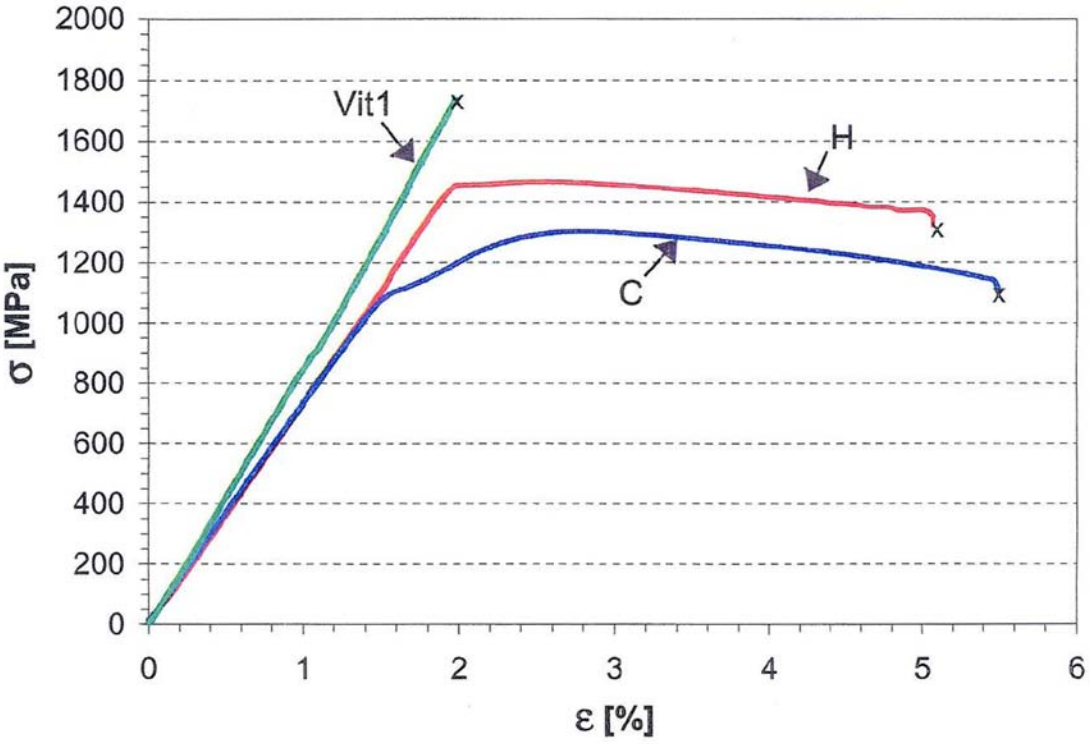

Figure 1.6 – Tension tests of the in-situ composite LM2 produced at Caltech (*C*) and Howmet (*H*) along with the monolithic BMG Vitreloy 1 (courtesy of C. P. Kim, Caltech thesis, 2001). The in-situ composites have nearly the same tensile strength as the monolithic glass, because of their glassy matrix, but have ~ 3% tensile ductility, because of their soft microstructure. However, the difference between the curves *H* and *C* indicates that processing plays a role. As we know now, the alloy at lower strength with higher ductility has larger, more coarsened dendrites. The higher-strength alloy has smaller dendrites.

References

1. Meyers, M. A., and Chawla, K. K., *Mechanical Behavior of Materials.* (Prentice Hall, Upper Saddle River, NJ, 1999).
2. Cohen, M. H., and Turnbull, D., *Nature* **203**, 964 (1964).
3. Kauzmann, W., *Chem. Rev.* **43**, 219 (1948).
4. Angell, C. A., *Science* **267**, 1924 (1995).
5. Herlach, D. M., *Mater. Sci. Eng. R* **12**, 177 (1994).
6. Uhlmann, D. R., *J. Non-Cryst. Solids* **7**, 337 (1972).
7. Reed-Hill, R. E., and Abbaschian, R., *Physical Metallurgy Principles, 3rd Edition.* (PWS Publishing Co., Boston, MA, 1994).
8. Klement, W., Willens, R. H., and Duwez, P., *Nature* **187**, 869 (1960).
9. Nishiyama, N., and Inoue, A., *Mater. Trans. JIM* **38**, 464 (1997).
10. Peker, A., and Johnson, W. L., *Appl. Phys. Lett.* **63**, 2342 (1993).
11. Waniuk, T. A., Schroers, J., and Johnson, W. L., *Appl. Phys. Lett.* **78**, 1213 (2001).
12. Haberman, R., *Elementary Applied Partial Differential Equations, 3rd Edition.* (Prentice Hall, Upper Saddle River, NJ, 1998).
13. Turnbull, D., *Contemp. Phys.* **10**, 473 (1969).
14. Inoue, A., and Takeuchi, A., *Mater. Trans.* **43**, 1892 (2002).
15. Greer, A. L., *Nature* **366**, 303 (1993).
16. Massalski, T. B., ed., *Binary Alloy Phase Diagrams, 2nd Edition.* (ASM International, Metals Park, OH, 1990).

17. Duan, G., Wiest, A., Lind, M.-L., et al. *Scripta Mater.* **58**, 465 (2008).

18. Lin, X. H., Johnson, W. L., and Rhim, W. K., *Mater. Sci. Trans.* **38**, 473 (1997).

19. Telford, M., *Materials Today* **7**, 36, (2004).

20. Wang, G., et al. *Non-Cryst. Solids* **351**, 209 (2005).

21. Guo, H., et al. *Nature Mater.* **6**, 735 (2007).

22. Lewandowski, J. J., Greer, A. L., *Nature Mater.* **5**, 15 (2006).

23. Hofmann, D. C., et al. *Nature* **451**, 1085 (2008).

24. Ashby, M. F., *Materials Selection in Mechanical Design.* (Pergamon, Oxford, 1992).

25. Inoue, A., Zhang, W., Tsurui, T., et al. *Phil. Mag. Lett.* **85**, 221 (2005).

26. Zhu, Z. W., et al. *Scripta Mater.* **54**, 1145 (2006).

27. Eckert, J., Das, J., Kim, K. B., et al. *Intermetallics* **14**, 8 (2006).

28. Xie, S., George, E. P., *Intermetallics* **16**, 485 (2008).

29. Lui, Y. H., et al. *Science* **315**, 1385 (2007).

30. Yao, K. F., et al. *Appl. Phy. Lett.* **88**, 122106 (2006).

31. Hajilaoui, K., et al. *Mater. Sci. & Eng. A* **449**, 105 (2007).

32. Chen, L. Y., et al. *Phys. Rev. Letts.* **100**, 075501 (2008).

33. Bae, D. H., et al. *Mater. Sci. & Eng. A* **449**, 111 (2007).

34. Schroers, J., Johnson, W. L., *Phys. Rev. Lett.* **93**, 255506 (2004).

35. Qiang, J. B., et al. *App. Phys. Lett.* **90**, 231907 (2007).

36. Hays, C. C., Kim, C. P., Johnson, W. L., *Phys. Rev. Lett.* **84**, 2901 (2000).

37. Szuecs, F., Kim, C. P., Johnson, W. L., *Acta Mater.* **49**, 1507 (2001).

38. Cytron, S. J., *J. Mat. Sci. Lett.* **1**, 211 (1982).

39. Lee, M. L., et al. *Acta Mater.* **52**, 4121 (2004).

40. Kühn, U., Eckert, J., Mattern, N., Schultz, L., *Appl. Phys. Lett.* **80**, 2478 (2002).

41. Kühn, U., Eckert, J., Mattern, N., Schultz, L., *Mater. Sci. & Eng. A* **375**, 322 (2004).

Chapter 2

TEM Study of Structural Evolution in a Copper-Mold-Cast $Cu_{46}Zr_{54}$ Bulk Metallic Glass*

2.1 Commentary

The Cu-Zr binary glass-forming system is an excellent model for understanding BMGs. This chapter exploits two very similar BMGs ($Cu_{46}Zr_{54}$ and $Cu_{50}Zr_{50}$) with quite different properties in bending and in compression tests. Although the compositions are similar, one alloy seems to have higher toughness than the other, based on three-point-bending tests. Work in literature on Cu-Zr and Cu-Zr-Al BMGs attributed the difference in compressive plasticity between these series of alloys to partial crystallization of the glass matrix, which somehow restricted shear band propagation. During my TEM work, I noticed that these alloys were all fully amorphous, as long as the samples were prepared "artifact free."

The results of many BMG papers have been thrown into question recently, as new evidence has been presented that compression tests are an undesirable method for comparing the mechanical properties of BMGs. As we discuss in Chapter 4, compressive plasticity is a result of friction and closing stresses on shear bands and many alloys that exhibit plastic strain in compression are very brittle went bent. However, it is true that BMGs have widely varying mechanical properties, even

* The contents of this chapter are published: Douglas C. Hofmann, Gang Duan, and William L. Johnson, *Scripta Materialia*, 54, 1117–1122 (2006).

though they are all fully amorphous. Many explanations have been offered to explain this (such as high Poisson's ratio and strain-induced crystallization) but in every glass-forming system that we have seen, partial crystallization *always* results in embrittlement.

In the Cu-Zr binary system, as with many other systems containing Cu and Zr, the first phases to crystallize are the brittle intermetallics Zr_2Cu and $Cu_{10}Zr_7$, as verified through X-ray diffraction. Unfortunately, due to the geometric stability of compression tests, partially crystalline BMGs that contain these phases often yield plastically. The particles can arrest shear band propagation and generate multiple shear bands, leading to the incorrect assumption that the partial crystallization actually toughens the BMG. This has lead to a great deal of seemingly misguided research in which brittle phases (such as carbides) are incorporated into metallic glasses to improve toughness. Almost all of this research relies solely on compression tests so apparent progress has continued to drive the work. (As we will show in Chapter 4, a ductile phase inclusion is absolutely necessary to obtain significant toughening and tensile ductility because the brittle phases simply separate from the glass matrix during unconfined loading, such as bending or tension tests.)

In this chapter we will discover that on occasion one of the phases that crystallizes is b.c.c. Other researchers have observed this and have created alloys that partially crystallize into a two-phase alloy of glass and b.c.c. dendrites. Unfortunately, many of these b.c.c. phases that form are stiff ordered phases, not the soft phases necessary for ductility.

2.2 Background on Cu-Zr Binary Bulk Metallic Glasses

Recent progress in both binary bulk metallic glasses (BMGs) and ductile metal reinforced BMG matrix composites has triggered interest in trying to combine beneficial mechanical properties with simple glass-forming systems [1–16]. Such work is vital to future applications of BMGs because it is widely known that while these amorphous metals show unique mechanical properties, they lack the tensile ductility needed for structural engineering applications. For instance, most metallic glasses loaded in uniaxial tension or plane stress fail catastrophically on one shear band with negligible plasticity [3].

To combat this problem, many researchers have been investigating glassy alloys that inherently show some level of plastic strain prior to failure in uniaxial compression tests [1, 12, 13]. Although special considerations must be taken during compression tests to assure that the samples are plane parallel and have the correct aspect ratio, some monolithic BMGs exhibit significant compressive plasticity while most exhibit none. Many of these alloys are based on the simple Cu-Zr binary BMG, an alloy which seems to have an inherently high level of toughness in its amorphous state. This BMG is also fundamentally important to understanding the structure of BMGs because its binary composition lends itself well to molecular dynamics studies.

2.3 Designing the TEM Study

The aim of this chapter is to use transmission electron microscopy to address issues of partial crystallization that arise in literature regarding the Cu-Zr binary. This is done by studying micrographs from a 1-mm-thick, 4-mm-wide, and 40-mm-long

cast $Cu_{46}Zr_{54}$ binary BMG based on the Cu-Zr phase diagram, where the current alloy is a eutectic composition [17–19]. Much work has been done on both this alloy and the very similar $Cu_{50}Zr_{50}$ alloy, but there has never been any indication that the mechanical behavior or the microstructures of these alloys are different. Since a molecular dynamics study has already been completed on the eutectic composition, it was selected for this TEM study [5].

The locations of the TEM samples vary from the mold tip, where the sample is totally amorphous, to 20 mm away from the tip, where the sample is partially crystalline, to 40 mm from the tip, where the sample is totally crystalline. Throughout the strip, there is a gradient of crystallization due to the uneven cooling rate in the casting process. This is important in the Cu-Zr system because its low critical casting thickness (~ 2 mm) and tendency to crystallize has caused many researchers to claim that nanometer scale crystallites or second phase particles are what cause the observed toughness in the alloy.

The intent of this TEM work is to demonstrate that the $Cu_{46}Zr_{54}$ BMG has no nanometer scale crystallites if it is successfully vitrified and is capable of having complex microstructures when it is partially crystalline. Later, comparisons are given between the mechanical properties of $Cu_{46}Zr_{54}$ and data from literature for $Cu_{50}Zr_{50}$. The ultimate goal is to show that the Cu-Zr binary system has an inherent toughness in the amorphous state resulting in the observed plastic strain and that partial crystallization only leads to a much more brittle alloy.

2.4 Experimental Method

The Cu-Zr alloy used in this work was prepared first as an ingot by arc melting together ultrasonically cleansed 99.999 at. % Cu and 99.9 at. % Zr pieces on a water-cooled copper plate in a high-purity argon atmosphere. The ingot was melted at least three times to promote homogeneity. The ingot was then remelted under high vacuum in a quartz tube through the use of an induction heating coil and injected with argon pressure into a copper mold. The mold has a cavity with thickness 1 mm, width 4 mm, and length approximately 40 mm. To study the glass transition and crystallization behavior of the alloy, a Bruker AXS X-ray diffractometer was used with Cu-Kα source and a Perkin-Elmer DSC7 (differential scanning calorimeter) was used with constant heating rate (dT/dt = 0.33 K/s). Transmission electron microscope work was done using a Philips EM430 electron microscope at 300 keV.

It was discovered that creating very large electron-transparent areas is possible in $Cu_{46}Zr_{54}$ by using chemical thinning. The etching conditions were optimized on multiple samples until a large electron-transparent region was obtained with 1:2 HNO_3:CH_3OH 5V and -25°C.

The TEM samples were prepared by first taking the 1-mm-thick strip of $Cu_{46}Zr_{54}$ and mechanically grinding it down to 250 μm. Starting at the amorphous tip, a punch was used to cut 3-mm-diameter disks from the thinned strip. In total, eight TEM-sized foils were punched from the strip and then electropolished using the conditions given above. The locations of the TEM foils taken from the BMG strip are diagramed in Figure 2.1.

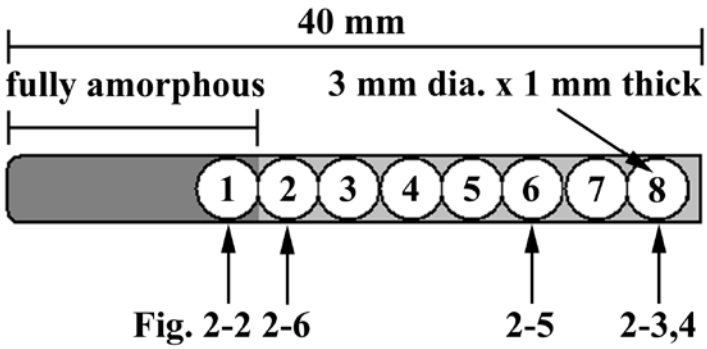

Figure 2.1 – Diagram of BMG strip showing location of eight samples used in TEM study and the figure numbers for the TEM micrographs relating to each sample.

2.5 High-Resolution TEM

Figure 2.2(a) shows a nominal HRTEM micrograph from a part of the strip nearest the tip, sample 1. Despite intensive study of this sample, no hint of crystallization or crystallites was observed in dark field imaging, selected area diffraction (inset in Figure 2.2(a)), or HRTEM imaging. As an example of what crystallization looks like in HRTEM, compare Figure 2.2(a) with Figure 2.2(b), a HRTEM image of Si oriented on the [110] pole. The diamond cubic structure of Si leads to an ordered contrast in TEM imaging. In the HRTEM micrograph of $Cu_{46}Zr_{54}$ no such ordering is observed for any sample tilt, indicating a totally amorphous matrix. Although not shown, XRD and DSC experiments on the tip of the sample also indicate that $Cu_{46}Zr_{54}$ can be fully amorphous with no hint of crystallization. The X-ray diffraction pattern exhibits a pair of broad diffraction maxima, with no evidence of crystalline Bragg peaks. The DSC scan clearly shows an endothermic heat event (associated with glass transition) and further heat releases due to crystallization.

Although nanocrystalline particles can evade detection through DSC and XRD, the TEM confirms that the samples are indeed amorphous.

Figure 2.3 shows three bright field micrographs, with the objective aperture centered over the transmitted spot, and one diffraction pattern with a large selected area—all taken from sample 8, nearest the top of the mold. Many microstructural features are evident in the micrographs that are not usually seen in BMG samples. Clearly, there are grain boundaries, where bands of contrast at different angles meet, and dendrites, which appear in Figure 2.3(c). The diffraction pattern in Figure 2.3(a) shows a weak amorphous halo with bright spots from crystalline diffraction.

Figure 2.4 shows bright field/dark field pairs from the dendrites within the bulk microstructure. Figure 2.4(a–b) show multiple dendrites with the dark field conditions being set up on the amorphous halo in the diffraction pattern (inset in Figure 2.4(a)). Figure 2.4(c–d) are high-resolution TEM micrographs of the interface between the dendrite and the matrix. Comparing Figure 2.4(c–d) with Figure 2.2 leads to the conclusion that the matrix is at least partially amorphous, while the dendrites are crystalline. From the selected area diffraction pattern inset in Figure 2.4(d), the dendrites are a b.c.c. phase of Cu-Zr and are similar in size and microstructure to the β-phase (b.c.c.) in metallic-glass-based composites. In this work, they are found within a mostly crystalline matrix, unlike the fully amorphous matrix in the composite [3]. The dendrites in ductile-phase reinforced composites have been shown to create organized shear band patterns under mechanical loading, which greatly increases the toughness of the alloy [2, 9]. However, although the dendrites observed in the TEM images have a b.c.c. microstructure, without β-stabilizing elements such as Nb, V, Ta,

and Mo, the dendrites are likely stiff phases relative to the amorphous matrix. As we discuss in Chapter 4, the dendritic phase must exhibit a lower shear modulus than the glass matrix for significant toughening to occur.

Figure 2.5 shows a bright field/dark field pair using high-resolution TEM on a typical section of the bulk matrix, from sample 6. The diffraction pattern, which is inset in Figure 2.5(a), shows many bright spots from diffracting crystallites. The dark field micrograph shows a structured particle, as well as many nano-scale diffracting crystallites, which appear as bright spots. Unlike Figure 2.3, where a large grain structure is clearly present, this sample, which is closer to the amorphous tip, has no clearly visible grain structure and yet has a large volume fraction of crystallites within a bulk glassy matrix.

While Figure 2.4 shows the b.c.c. dendrites which are usually associated with a bulk metallic glass based composite, Figure 2.6 shows a heterogeneous microstructure with a combination of a glassy matrix with crystalline second-phase particles. The micrographs were taken from sample 2, just above the sample that was shown to be totally amorphous. Figure 2.6(b) shows an inset selected area diffraction pattern containing a few small spots from diffracting crystallites, but mostly shows an amorphous halo, typical of a bulk metallic glass. The dark field micrograph, also shown in Figure 2.6(b), has a band of very small diffracting crystallites, less than 10 nm in size. Figure 2.6(a) shows a bright field image with the objective aperture centered over the transmitted spot to gain contrast. This demonstrates that the first phases to crystallize in the Cu-Zr binary BMG are tiny crystalline particles, which are likely brittle intermetallics (such as Zr_2Cu and $Cu_{10}Zr_7$).

Following the TEM analysis, mechanical testing was performed on the $Cu_{46}Zr_{54}$ BMG to investigate the effect crystallization has on plastic strain. It is noteworthy to mention the difficulty in preparing reproducible samples of the binary alloy. In the current work, the samples were very near the critical casting thickness of the alloy and slight variations in the copper-mold casting process caused varying degrees of crystallization in the strips and rods. Figure 2.7 shows a compression test on a 2 mm rod of $Cu_{46}Zr_{54}$ that was checked on top and bottom through XRD for any sign of crystallization. In a 2 mm rod, the length of amorphous $Cu_{46}Zr_{54}$ seems to vary between approximately 3 mm and 6 mm, depending on the cooling rate, before the onset of crystallization. The compression test sample in Figure 2.7 was from the tip of the 2 mm rod and was shown to be fully amorphous. From Figure 2.7, the amorphous $Cu_{46}Zr_{54}$ showed only ~ 1% of plastic strain before failure.

Figure 2.8 shows the results of a three-point-bending test comparing $Cu_{46}Zr_{54}$ and $Cu_{50}Zr_{50}$. In addition to having a steeper slope in the load versus bend displacement plot, $Cu_{50}Zr_{50}$ is able to plastically deform slightly before failure. The bend test of $Cu_{46}Zr_{54}$ showed no plastic strain prior to failure.

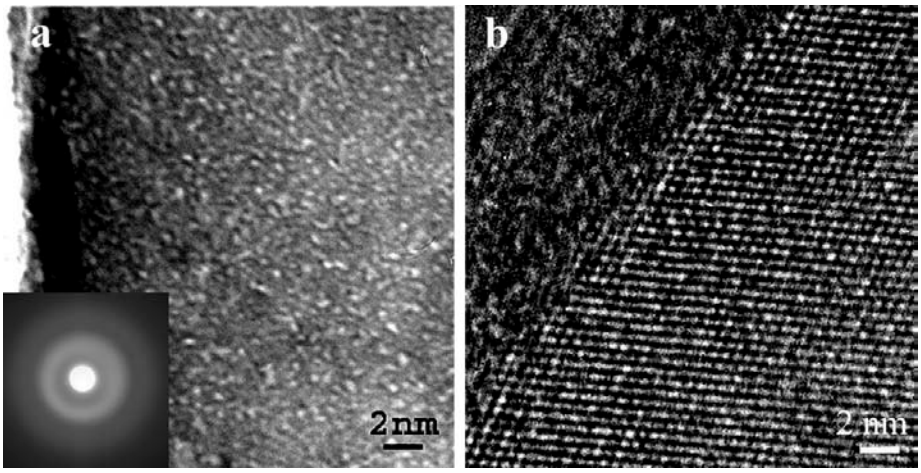

Figure 2.2 – (a) HRTEM micrograph of $Cu_{46}Zr_{54}$ near the sample tip showing totally amorphous microstructure and inset diffraction pattern. (b) HRTEM of Si oriented on the [110] to demonstrate the contrast seen in crystalline samples through TEM.

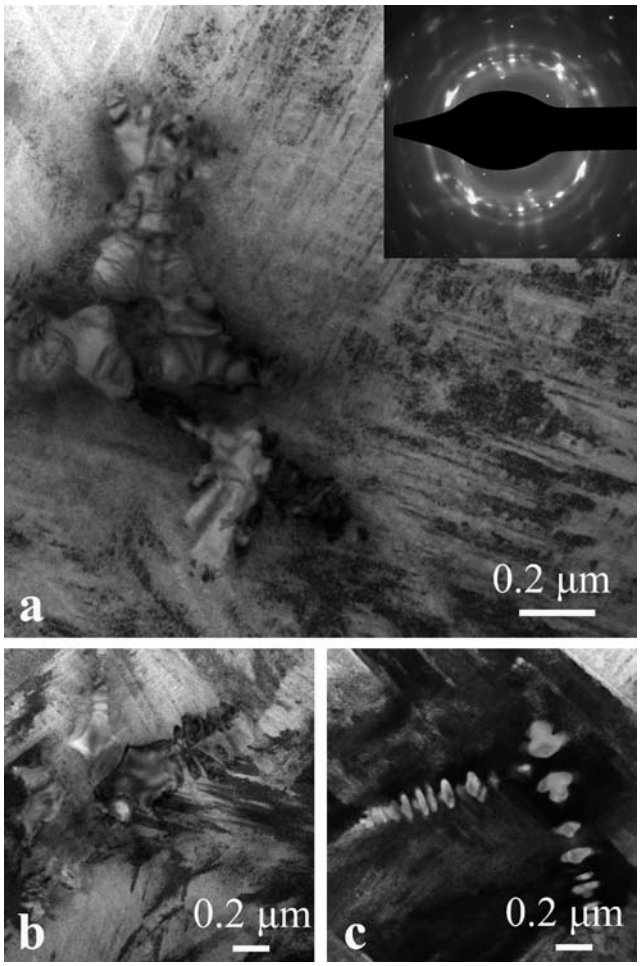

Figure 2.3 – (a), (b), (c) TEM bright field images from $Cu_{46}Zr_{54}$ far away from the amorphous tip. Inset DP in (a) shows largely crystalline diffraction.

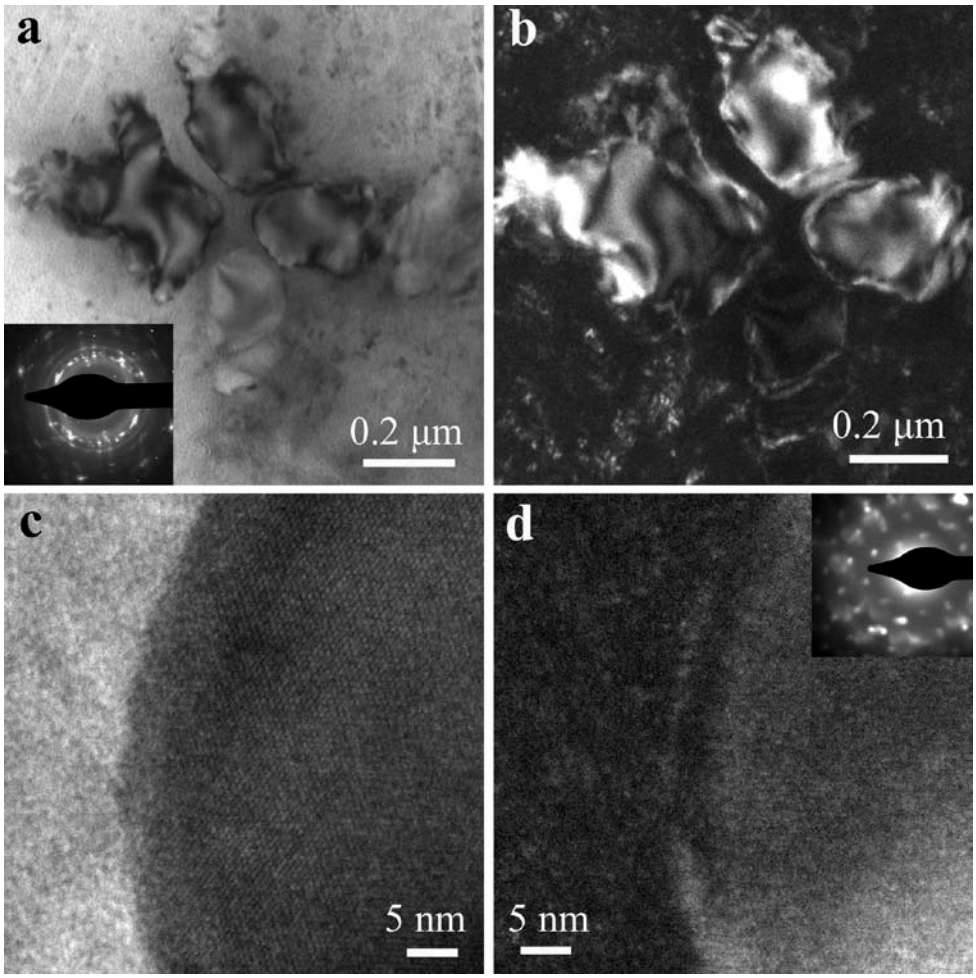

Figure 2.4 – (a), (b) BF/DF pairs of sheared dendrites with DF set up on the amorphous halo in the inset DP. (c), (d) HRTEM micrographs at interface of dendrite and BMG matrix with inset DP showing bcc diffraction.

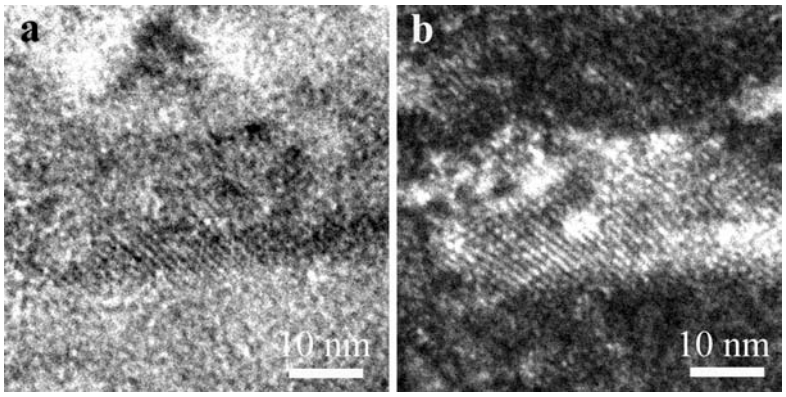

Figure 2.5 – HRTEM BF/DF pairs on $Cu_{46}Zr_{54}$ matrix with (a) inset DP and (b) DF set up on amorphous halo.

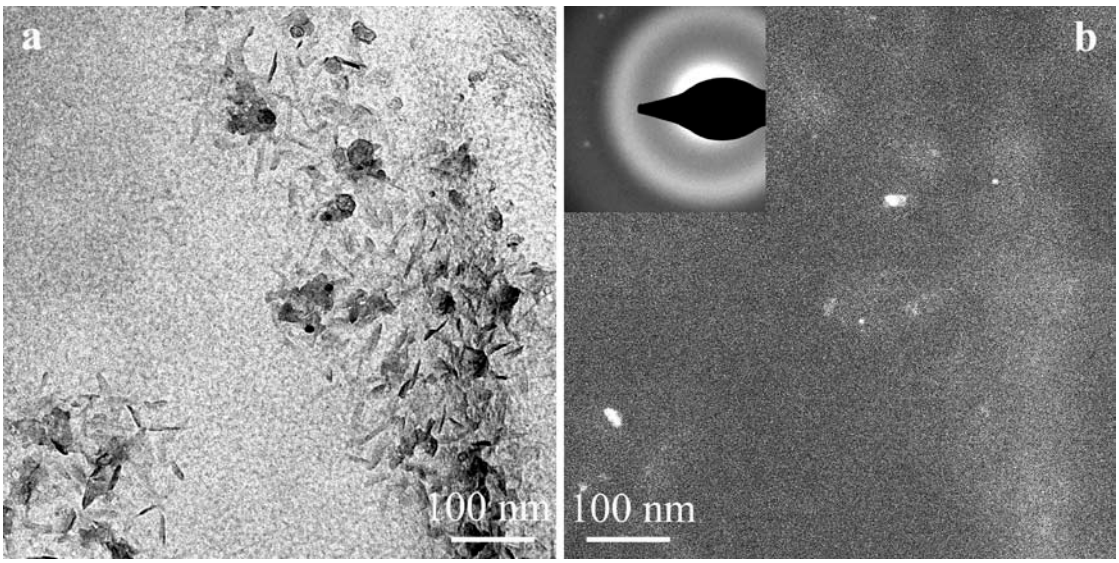

Figure 2.6 – (a) BF micrograph and (b) DF micrograph with inset DP showing heterogeneous microstructure of both glassy matrix and second phase particles.

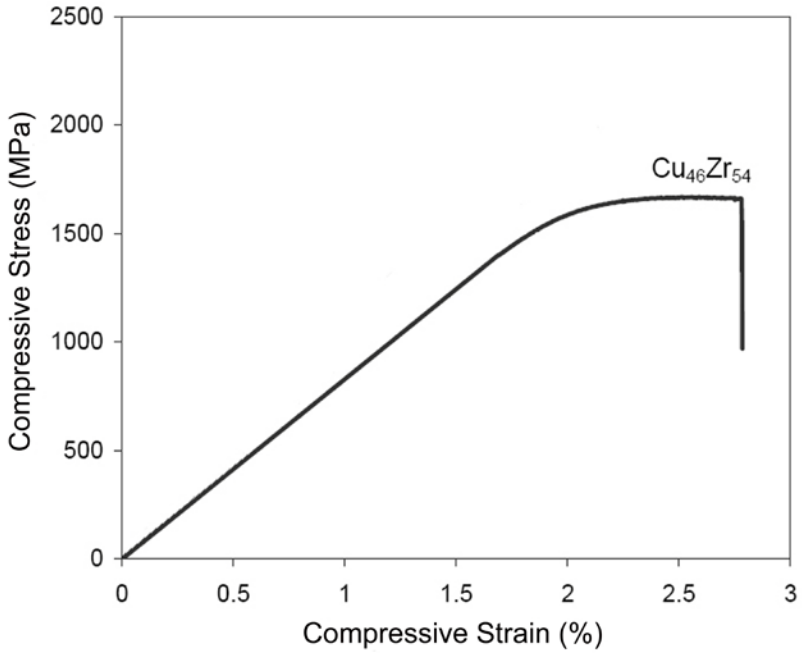

Figure 2.7 – Stress-strain curve of fully amorphous $Cu_{46}Zr_{54}$ under compression at a strain rate of 4E-4 s^{-1} showing 1% plastic strain.

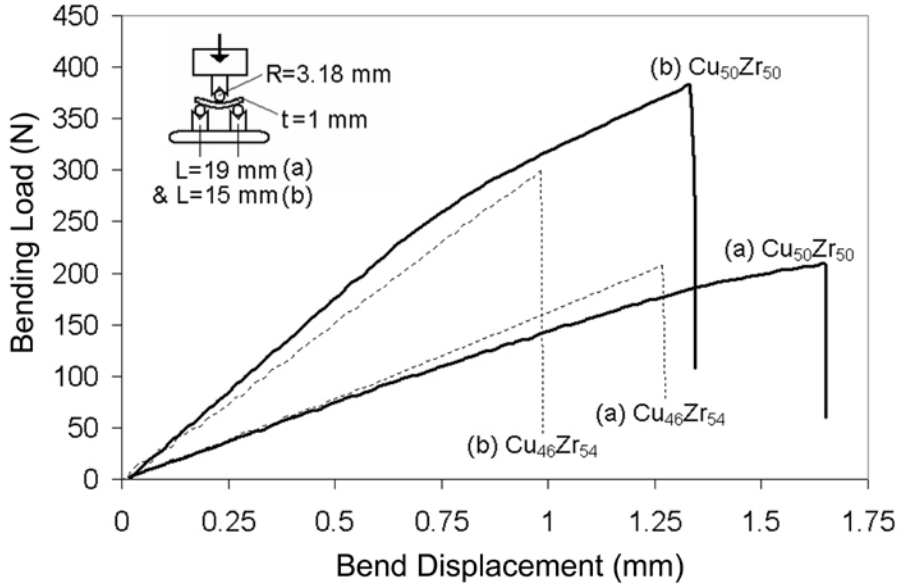

Figure 2.8 – Three-point-bend test of $Cu_{46}Zr_{54}$ and $Cu_{50}Zr_{50}$ showing the differences in mechanical properties despite their similar compositions and fully amorphous structures. The bending configurations for the two tests are shown in the inset.

2.6 Discussion

The first of many issues that arise from the TEM micrographs is that in the first 10–15 mm of the alloy (the tip), the sample shows a totally amorphous structure with no diffracting crystallites. Although there is a slight variation in composition between $Cu_{46}Zr_{54}$ and $Cu_{50}Zr_{50}$, the micrographs contradict the findings of both Das et al. [1] and Inoue et al. [12], where it was claimed that nanometer-sized crystallites were found in the later alloy. The micrographs are supported, however, by the work of Sun, et al. [13], where it was rigorously demonstrated that TEM sample preparation can produce artifacts that make the sample appear to be partially crystalline. In that work, $Cu_{64.5}Zr_{35.5}$ was shown to be both amorphous and apparently partially crystalline depending on the thinning technique used. Additionally, Wang et al. [14] did a study on the glass-forming ability of $Cu_{50}Zr_{50}$ and showed through HRTEM that rods cast less than 2 mm in diameter were fully amorphous.

This contradiction in the observed microstructures is important in terms of explaining the observed mechanical properties of both $Cu_{46}Zr_{54}$ and $Cu_{50}Zr_{50}$. The compression test shown in Figure 2.7 demonstrates that in a 2 mm rod of fully amorphous $Cu_{46}Zr_{54}$, there is only 1% plastic strain before failure, unlike the 7.9% reported in $Cu_{50}Zr_{50}$ [1]. The difference in plastic strain may be caused by slight anti-parallelism or by a short aspect ratio. If the tests are indeed valid, and the rod of $Cu_{50}Zr_{50}$ used in the compression test was totally amorphous, as would be suggested by the work of Wang et al. [14], then there is clearly some internal feature present in these bulk metallic glasses that causes a significant increase in plastic strain with a small shift in composition. Typically, Poisson's ratio is used to explain why some

BMGs are tougher than others within a specific system. It is theorized that a higher Poisson's ratio makes it more difficult for cavitation to occur within a slipping shear band. Indeed, as we demonstrate in the next chapter, the addition of 5 atomic% of aluminum to the Cu-Zr binary alloy both increases the Poisson's ratio and the plastic bending strain. However, no appreciable difference in Poisson's ratio was measured for $Cu_{50}Zr_{50}$ and $Cu_{46}Zr_{54}$, despite their obvious difference in toughness. Clearly, there is more involved than simply Poisson's ratio.

As a direct comparison of the two alloys, two three-point-bending tests were performed on 1-mm-thick strips with sample lengths 15 mm and 19 mm. In both tests shown in Figure 2.8, $Cu_{50}Zr_{50}$ demonstrates plastic strain prior to failure (indicated by the non-linear portion of the bend versus displacement curve). On the other hand, $Cu_{46}Zr_{54}$ showed no plastic strain prior to failure in either test. The slopes of the curves in the elastic bending region of Figure 2.8 can be used to calculate Young's modulus using beam bending analysis, as was done in [8] and in Chapter 3. For the four tests shown, Young's modulus ranges from 82–93 GPa, similar to the acoustically measured value of 84 GPa for both alloys. The difference in slopes is attributed to slight differences in the loading configuration. Since both samples were fully amorphous in the bending region, the tests seem to indicate that the small change in composition has affected the internal property that toughens BMGs.

Additional bending and compression tests were attempted on the partially crystalline and fully crystalline regions demonstrated to be present in long strips of Cu-Zr alloys, and yet no increase in the plastic strain was discovered by these "composite" structures. In fact, the alloys became very brittle at the onset of

crystallization, and in most cases could be broken by hand. The presence of the brittle intermetallic phases dramatically reduces the toughness of the alloy.

2.7 Afterward

Our understanding of deformation in metallic glasses has evolved since this work was completed in 2006. Thus, this chapter has been modified from the published version (D.C. Hofmann, G. Duan, & W.L. Johnson, *Scr. Mater.* 54, 1117–1122 (2006)) to reflect our current understanding of BMGs.

References

1. Das, J., Tang, M.B., Kim, K.B., Theissmann, R., Baier, F., Wang, W.H., and Eckert, J., *Phys. Rev. Lett.* **94**, 205501 (2005).
2. Hays, C.C., Kim, C.P., and Johnson, W.L., *Phys. Rev. Lett.* **84**, 13 (2000).
3. Park, J.S., Lim, H.K., Kim, J.-H., and Park, J.M., *J. Mater. Sci.* **40**, (2005).
4. Pekarskaya, E., Kim, C.P., and Johnson, W.L., *J. Mater. Res.* **16**, 9 (2001).
5. Duan, G., Xu, D., Zhang, Q., Cagin, T., Johnson, W.L., and Goddard III, W.A., *Phy. Rev. B.* **71**, 224208 (2005).
6. Xu, D., Duan, G., and Johnson, W.L., *Phys. Rev. Lett.* **92**, 245504 (2004).
7. Wang, D., Li, Y., Sun, B.B., Sui, M.L., Lu, K., and Ma, E., *Appl. Phys. Lett.* **84**, 4029 (2004).
8. Xu, D.H., Lohwongwatana, B., Duan, G., Johnson, W.L., and Garland, C., *Acta Mater.* **52**, 2621 (2004).
9. Tang, M.B., Zhao, D.Q., Pan, M.X., and Wang, W.H., *Chin. Phys, Lett.* **21**, 901 (2004).
10. Duan, G., Xu, D.H., and Johnson, W.L., *Metall. Mater. Trans. A* **36A**, 455 (2005).
11. Inoue, A., Zhang, W., and Saida, J., *Mater. Trans., JIM* **45**, 1153 (2004).
12. Inoue, A., Zhang, W., Tsurui, T., Yavari, A., and Greer, A., *Phil. Mag Lett.* **85**, 2 (2005).
13. Sun, B., Wang, Y., Wen, J., Yang, H., Sui, M., Wang, J., and Ma, E., *Scripta Mater.* **53**, 805 (2005).

14. Wang, W., Lewandowski, J., and Greer, A., *J. Mater. Res.* **20**, 9 (2005).

15. Leonhard, A., Xing, L., Heilmaier, M., Gebert, A., Eckert, J., and Schultz, L., *Nano. Struc. Mater.* **10**, 5 (1998).

16. Fan, C., Ott, R., and Hufnagel, T., *Appl. Phys. Lett.* **81,** 6 (2002).

17. Massalski, T.B., *Binary Alloy Phase Diagrams,* 2nd ed. (Metals Park, OH, Int. 1990).

18. Wang, D., Li, Y., Sun, B.B., Sui, M.L., Lu, K., and Ma, E., *Appl. Phys. Lett.* **84**, 4029 (2004).

19. Hofmann, D.C., Duan, G., and Johnson, W.L.. *Unpublished* (2005).

Chapter 3

Shear Band Formation in Cu-Zr-Based Bulk Metallic Glasses through Three-Point-Bending

3.1 Overview

Herein we investigate bending tests on 1 mm strips of monolithic metallic glasses. The results are very interesting because we discover that BMGs vary in their resistance to fracture, determined by their amount of plastic bending strain in three-point-bending tests. Some glasses exhibit brittle failure while others exhibit dense patterns of closely spaced shear bands. In this chapter, we focus mainly on the ternary Cu-Zr-Al BMG, which displays the largest amount of bending plasticity. We use bending equations to estimate the yield strain and Young's modulus, and then we use shear band analysis (derived elsewhere) to estimate the total strain. In Section 3.7, we discuss fracture toughness and plastic zone size, which in BMGs is related to how long a shear band can develop before it nucleates a crack. We use the bending tests to determine the critical length of a shear band before it becomes unstable and we relate that length scale to fracture toughness in metallic glass matrix composites. This chapter leads into Chapter 4, where we develop "designed composites" by matching of key fundamental length scales.

3.2 Background on Bending Tests

Unlike crystalline metals, which can accommodate plastic strain through slip, twinning, etc., bulk metallic glasses undergo permanent deformation through formation of shear bands. In most BMGs, plastic deformation is a function of sample geometry and experimental testing conditions [1]. For instance, Inoue et al. [2] and Katsuya et al. [3] found that as sample size increases, bending ductility decreases. Conner et al. [1, 4] showed that as sample thicknesses approach the "bulk" level (~ 1 mm), there is a significant reduction in the number of shear bands generated, and thus, less plastic strain prior to failure.

To avoid catastrophic failure in unconstrained loading (as might be experienced in engineering applications) future BMGs or their composites must be able to exhibit plastic strain in tension and bending. Thus far, the only method for creating an alloy that is ductile in tension testing is through the use of a composite structure, where a softer dendritic phase inhibits shear band movement [5, 6] (see Chapter 4). However, recently a new class of alloys has been developed, based on the simple Cu-Zr binary system, that shows high levels of plastic strain in uniaxial compression tests [7–13].

Three-point-bending tests are rarely used in literature involving BMGs and yet they are quite useful for predicting the mechanical behavior of glasses in semi-unconstrained loading. Since tension tests always result in catastrophic failure in BMGs, and compression tests only give plastic strain (not ductility), bending tests provide a unique compromise between the two.

3.3 Experimental Method

The alloys used in this work were first prepared as an ingot by arc melting ultrasonically cleansed 99.999 at.% Cu, 99.9 at.% Zr, and 99.9 at.% Al on a water cooled copper plate in a high-purity argon environment. Each ingot was melted three times to promote homogeneity. The ingots were then melted in a quartz tube through an induction coil and injected with pressurized argon (0.2–0.4 MPa) into a copper mold. The cavity has thickness 1 mm, width 3 mm, and length 40 mm. Bending specimens were cut from the strip to a length of 25 mm and then polished with 3 micron diamond suspension. Three-point bending was completed on an Instron 5500R load cell with the sample resting on two 6.35 mm diameter pins separated by 18.89 mm and bent by a third pin of the same diameter. TEM work was done on a Phillips EM420 at 120 keV using samples that were prepared electrochemically with 25% nitric acid in methanol.

3.4 Results of Bending Tests

Figure 3.1 shows bending load versus bend displacement curves for five 1-mm-thick Cu-Zr based alloys bent in the three-point-bend configuration, shown in the inset. Each alloy shows a non-linear effect at small displacements that is caused by machine compliance. Only two alloys, $Cu_{47.5}Zr_{47.5}Al_5$ and $Cu_{16.4}Zr_{57.4}Ni_{8.2}Ta_8Al_{10}$, show a significant amount of plastic strain prior to failure at this thickness, indicating that they have enhanced fracture resistance.

Optical micrographs of shear bands on the tensile side of four bending specimens are shown in Figure 3.2. Each micrograph shows the shear band formation

near the point of fracture. Horizontal lines in the micrographs are damage from polishing and not from deformation.

Figure 3.3 is an example of the evolution of mixed mode cracks across the tensile side of the bending surface in $Cu_{47.5}Zr_{47.5}Al_5$, and is used to estimate the bending displacement at the onset of plastic strain. The sample was polished and then loaded in steps to increasing displacements. Following each step, the sample was removed from the testing equipment and viewed via optical microscopy for the presence of visible deformation. Figures 3.3(a–b) are micrographs of the sample bent to 1.25 mm and 1.50 mm, respectively. Just prior to 1.50 mm of displacement, mixed mode cracks begin to form and propagate from the edge of the sample across the width, indicating the onset of plastic strain. This coincides with the onset of the non-linear curvature in Figure 3.1 for $Cu_{47.5}Zr_{47.5}Al_5$.

Figure 3.3(c) is a higher magnification image of the arrow in Figure 3.3(b). The micrograph shows a mixed-mode crack at the surface being blunted by several small shear bands at its tip. From Figure 3.3(b) this plastic region in front of the mixed-mode crack extends approximately 450–600 μm into the sample. This plastic zone size can be used to approximate the fracture toughness of the glass (see Section 3.7). Figure 3.4 is an optical micrograph of the side view of a 1 mm $Cu_{47.5}Zr_{47.5}Al_5$ bending sample. The shear band spacing and offsets are estimated to be approximately 180 μm and 15.4 μm, respectively.

Prior to bending, the microstructure of $Cu_{47.5}Zr_{47.5}Al_5$ was evaluated through transmission electron microscopy (TEM). TEM foils were prepared from a 1-mm-thick bending specimen and then viewed less than five minutes after being chemically

thinned. The SAED pattern (Figure 3.5(c)) from a nominal part of the sample demonstrates that $Cu_{47.5}Zr_{47.5}Al_5$ has a fully amorphous structure. Two broad diffuse rings, characteristic of an amorphous material, are apparent in the diffraction pattern and no crystallization is observed in bright field or dark field imaging. To determine the effect of oxidation on the TEM images, the foils were stored in air for three days and viewed again for comparison. Figures 3.5(a–b) demonstrate that the oxidation of the sample now causes it to appear crystalline. The bright field image displays surface discoloration, the dark field image has small diffracting crystallites, and the SAED pattern has a thin, crystalline halo.

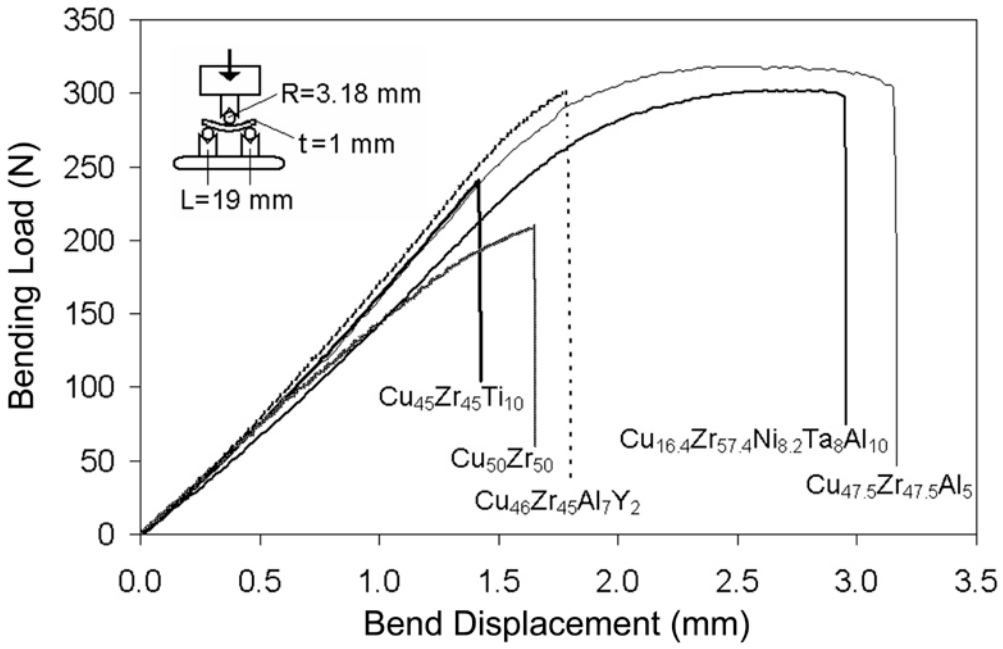

Figure 3.1 – Bending load versus bend displacement plot for five alloys bent in three-point-bending configuration shown in the inset. Despite all having an amorphous microstructure, some BMGs exhibit higher resistance to fracture in bending tests, as evidenced by their bending plasticity.

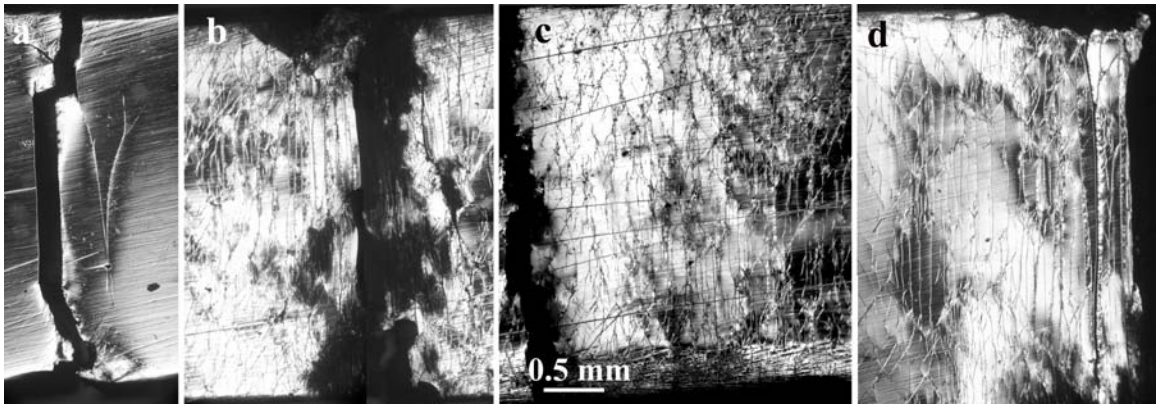

Figure 3.2 – Tensile surfaces of bending samples in (a) $Cu_{45}Zr_{45}Ti_{10}$, (b) $Cu_{16.4}Zr_{57.4}Ni_{8.2}Ta_8Al_{10}$, (c) $Cu_{46}Zr_{45}Al_7Y_2$, (d) $Cu_{47.5}Zr_{47.5}Al_5$.

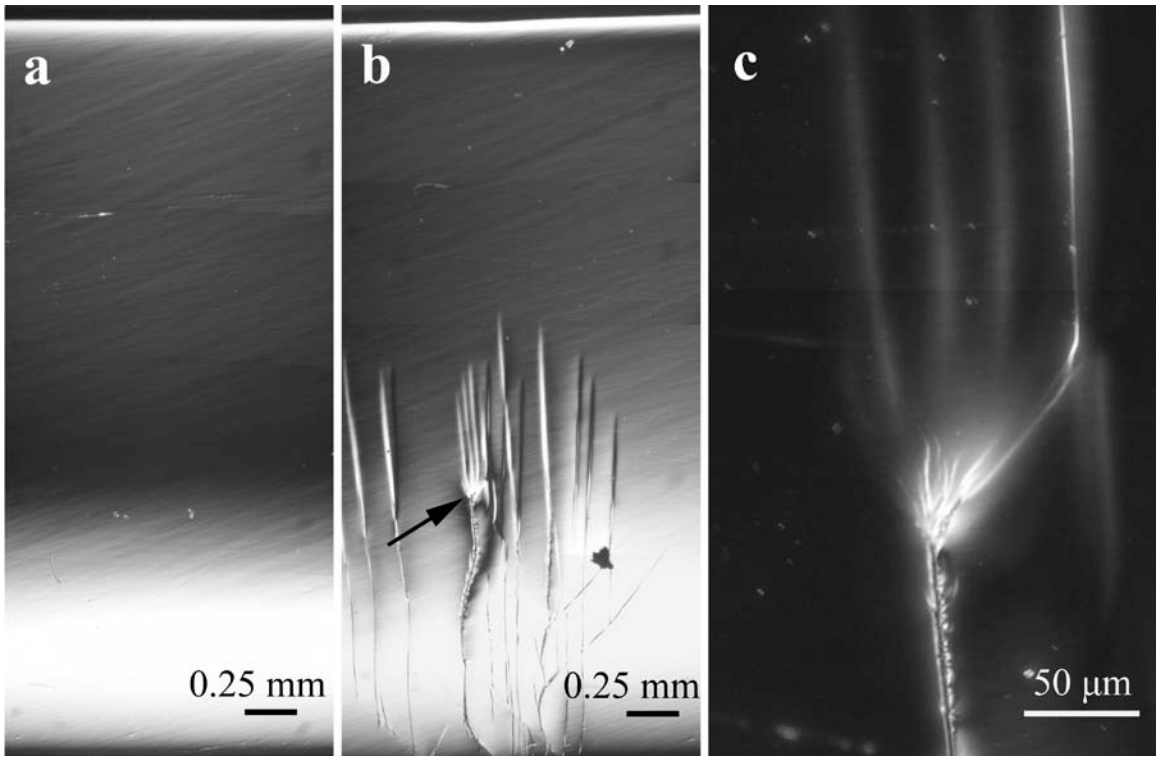

Figure 3.3 – (a) $Cu_{47.5}Zr_{47.5}Al_5$ loaded to 1.25 mm of bend displacement and then unloaded; (b) loaded to 1.50 mm showing onset of plastic strain. (c) enlargement of arrow showing that the plastic region in front of a crack is comprised of many small shear bands. The size of the plastic zone can be estimated from (b) to be several hundred microns.

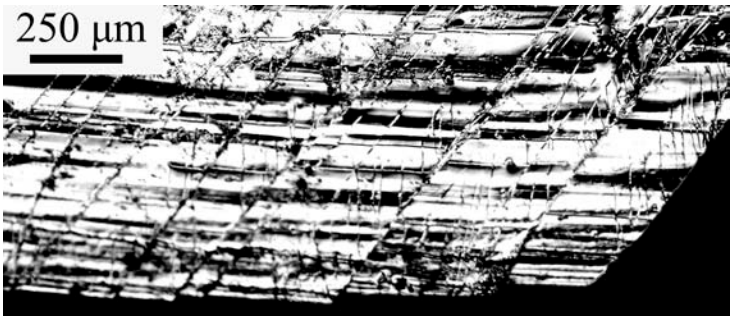

Figure 3.4 – Side view of a bending sample of $Cu_{47.5}Zr_{47.5}Al_5$ showing shear band offsets and shear band spacing. The sample was unpolished on the sides so horizontal lines are flow lines from casting, not from deformation. When the shear band offset become too large (at some specific shear band length) cracks nucleate and the beam fractures.

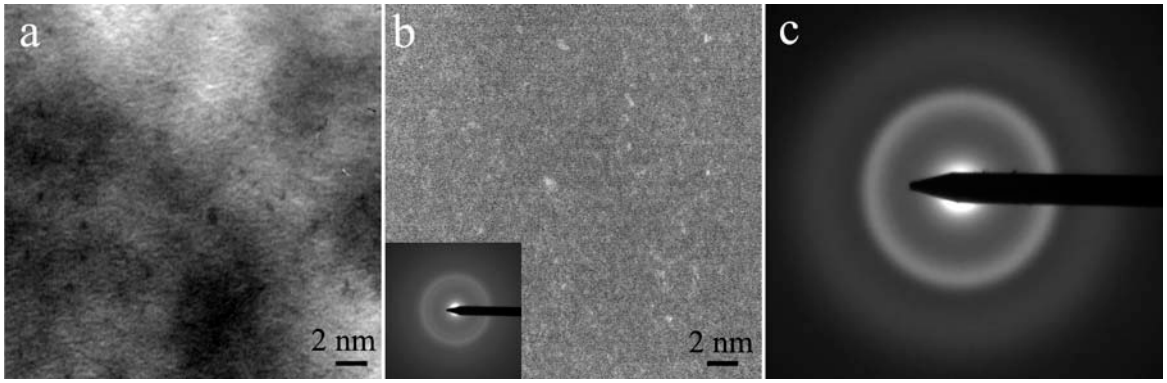

Figure 3.5 – (a) BF of $Cu_{47.5}Zr_{47.5}Al_5$ after three days exposed to air, showing discoloration and apparent crystallization. (b) DF showing small crystallites and a crystalline halo in the inset SAED pattern. (c) SAED pattern for $Cu_{47.5}Zr_{47.5}Al_5$ showing fully amorphous structure (taken less than five minutes after mechanically thinning).

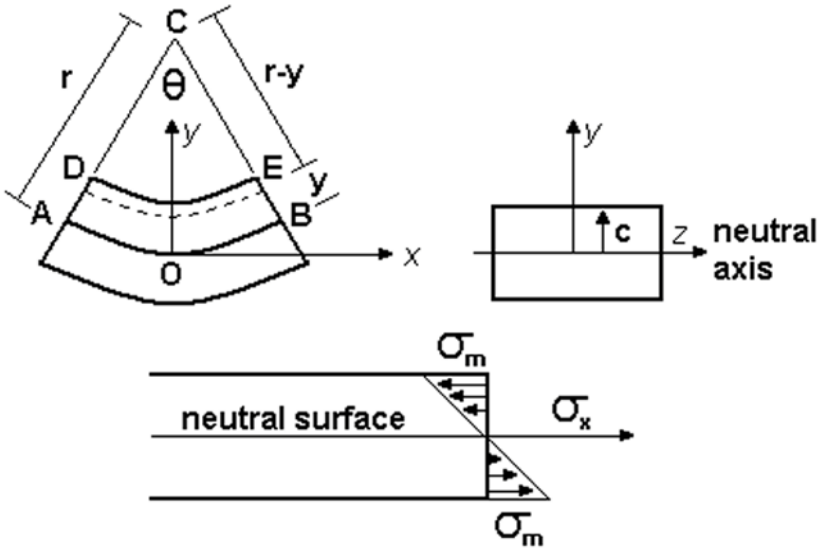

Figure 3.6 – Geometry of a sample in pure bending.

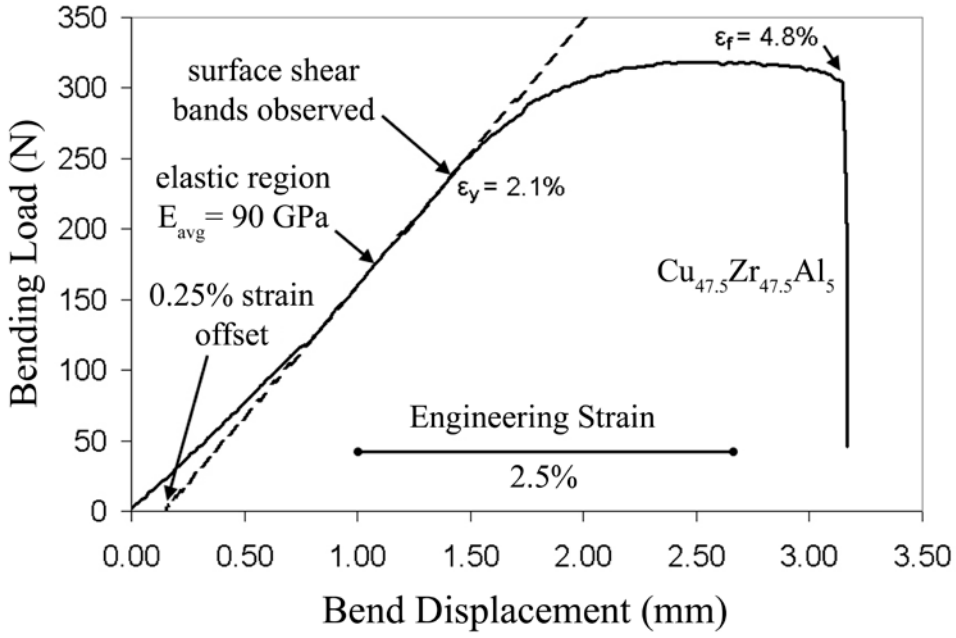

Figure 3.7 – Bending load versus bending displacement curve for $Cu_{47.5}Zr_{47.5}Al_{5,}$ showing estimations for Young's modulus, yield strain, and total strain.

3.5 Bending Equations

Figure 3.1 demonstrates that among several Cu-Zr based bulk metallic glasses, the amount of plastic strain observed in bending is dramatically different. TEM work, XRD, and DSC on these alloys suggests that all of the samples are fully amorphous. This confirms what we discovered in Chapter 2—that deformation in BMGs is maximized when the samples are amorphous, and partial crystallization only results in brittleness.

In the three-point bending tests, the number of shear bands that form is not the same for all metallic glasses even though they all have the same thickness. $Cu_{45}Zr_{45}Ti_{10}$, shown in Figure 3.2(a), is a very brittle alloy and failure occurs sharply without any visible plastic deformation near the fracture. In contrast, $Cu_{16.4}Zr_{57.4}Ni_{8.2}Ta_8Al_{10}$, shown in Figure 3.2(b), exhibits a large amount of plastic strain and has a very jagged fracture surface. $Cu_{46}Zr_{45}Al_7Y_2$, shown in Figure 3.2(c), has a shear band pattern unique from any other alloy. From Figure 3.1, this alloy does not demonstrate a large amount of plastic strain before failure but does have an extensive shear band pattern comprised of branch-like bands moving longitudinally on the sample. Additionally, the edge of the fracture surface has jagged diagonal steps. $Cu_{47.5}Zr_{47.5}Al_5$, shown in Figure 3.2(d), shows the most uniform shear band pattern along with the largest amount of plastic strain.

We can estimate the yield strain in bending for $Cu_{47.5}Zr_{47.5}Al_5$ (which we suspect will be ~ 2%) by employing stress and strain relationships for pure bending. To make these estimations more accurate, the experiments need to be repeated with a Linear Variable Displacement Transducer (LVDT) attached to the sample fixture to

offset the effects of machine compliance. However, since the loads are small in bending, we can approximate the yield strain.

Figure 3.6 shows the geometry of a sample in pure bending where the length AB (at the neutral axis) is *L*, the original length of the sample. Additionally, $L = r\theta$, where θ is the angle of curvature and r is the distance from the neutral axis to the center of bending. Near the compressive side of the beam, arc DE has length equal to $L' = (r-y)\theta$, where y is the distance from the arc DE to the arc AB. Since DE had an original length *L*, the deformation in DE is given by [14]:

$$\delta = L' - L \tag{3.1}$$

$$\delta = (r - y)\theta - r\theta \tag{3.2}$$

$$\delta = -y\theta\,. \tag{3.3}$$

The longitudinal strain ε_x is then found by dividing the deformation by the original length of DE

$$\varepsilon_x = \frac{\delta}{L} = -\frac{y}{r}\,. \tag{3.4}$$

The longitudinal strain can be rewritten in terms of the maximum absolute value of strain, ε_m, by noting that $\varepsilon_m = c/r$, where c is the distance from the neutral axis to the edge of the sample

$$\varepsilon_x = -\frac{y}{c}\varepsilon_m\,. \tag{3.5}$$

We now use Hooke's Law for elastic deformation to determine the stress associated with a strain, ε_x, and Young's modulus *E*. By multiplying Equation 3.5 by

E, we can determine the longitudinal stress in terms of the maximum absolute value of the stress, σ_m

$$\sigma_x = E\varepsilon_x \tag{3.6}$$

$$\sigma_x = -\frac{y}{c}\sigma_m . \tag{3.7}$$

The maximum stress occurs on both the tensile and compressive surfaces of the beam and their values are equal and opposite, as shown in Figure 3.6. By taking the sum of the moments around the z-axis, the elastic flexure formula can be obtained:

$$\int\left(-y\sigma_x dA\right) = M \tag{3.8}$$

$$\int\left(-y\right)\left(-\frac{y}{c}\sigma_m\right)dA = M \tag{3.9}$$

$$\frac{\sigma_m}{c}\int y^2 dA = M\ . \tag{3.10}$$

By noting that this last integral is the moment of inertia, *I*, of the beam, an equation for the maximum absolute value of the stress can be obtained from

$$\sigma_m = \frac{Mc}{I}. \tag{3.11}$$

The value I/c is known as the elastic section modulus, *S*, and is given by

$$S = \frac{I}{c} = \frac{1/12\left(bh^3\right)}{h/2} = \frac{1}{6}bh^2 . \tag{3.12}$$

The moment, *M*, is simply half of the bending load, *F/2*, times the half length of the distance between the simple supports, *L/2*. The stress in the elastic region of bending is calculated using the bending load:

$$\sigma_m = \frac{3}{2}\frac{FL}{bh^2}. \tag{3.13}$$

Displacement analysis is used to estimate Young's modulus, *E,* in the elastic region. The deflection, *u,* of point *c* downwards for a simply supported beam with a centrally located point load is given by

$$u = \frac{FL^3}{48EI}. \tag{3.14}$$

Solving for *E* gives an equation for Young's modulus as a function of bending load, *F,* and bending displacement, *u.* For each point in the elastic region, the value of *E* is calculated and then used in Hooke's law to obtain elastic strain. The average value of *E* obtained in this manner for $Cu_{47.5}Zr_{47.5}Al_5$ is 90 GPa, quite close to the value of 87 GPa, obtained through acoustical measurements (see Figure 3.7).

The onset of plastic strain, where shear bands are observed to form on the tensile surface of the specimen, coincides closely with the non-linear curvature in Figure 3.1 at 1.40 mm of bend. Knowing the location of the onset of plastic strain allows a linear fit to be made to the elastic region of Figure 3.1. A strain offset of 0.25% is estimated for the non-linear compliance of the samples and the engineering elastic strain is calculated for $Cu_{47.5}Zr_{47.5}Al_5$ in a three-point-bend test with 1 mm thickness. Converting from engineering strain, the true elastic strain of the sample is approximately $\varepsilon_y = 2.1\%$, similar to the 2% obtained from uniaxial compression tests (see Figure 3.7).

The total bending strain for $Cu_{47.5}Zr_{47.5}Al_5$ can be estimated using the shear band analysis given by Conner et al. [1, 4]. For a metallic glass plate, $2D$ in thickness, the total strain in the x-direction measured at the tensile surface is obtained from

$$\varepsilon_{xx}(y = D) = \frac{\Delta u_{\max}}{\sqrt{2}\lambda}, \tag{3.15}$$

where λ is the shear band spacing, and $\Delta u_{\max}$ is the shear band offset. For the 1-mm-thick sample of $Cu_{47.5}Zr_{47.5}Al_5$, the shear band spacing is approximately 180 μm, the shear band offset is 15.4 μm, and the half beam height is 0.5 mm. The total strain is thus estimated to be $\varepsilon_t = 6.1\%$. Subtracting the elastic strain, the plastic strain in the three-point-bending sample is estimated to be $\varepsilon_p = 4.0\%$.

The bending tests and the shear band analysis both confirm that $Cu_{47.5}Zr_{47.5}Al_5$ is a simple metallic glass with high bending plasticity and resistance to fracture, as was first suggested through uniaxial compression tests [7]. The alloy exhibits plastic strain prior to failure in bending and has significant shear band development on the tensile surface.

In both uniaxial compression tests and three-point-bending tests, $Cu_{47.5}Zr_{47.5}Al_5$ demonstrates more total strain than most other metallic glasses. Das et al. [7] explained this by claiming that nanometer scale particles were present in the microstructure. These crystallites are thought to enhance the plastic strain by interfering with shear band mobility. However, the TEM analysis of $Cu_{47.5}Zr_{47.5}Al_5$ shows that it is fully amorphous in 1-mm-thick plates and the partial crystallization may be caused by oxidation, as supported by [15, 16].

3.6 Commentary

Very few studies had been completed prior to this work to evaluate the mechanical properties of BMGs in bending. Instead, only compression tests were used, which raises questions about comparisons between alloys. How does one differentiate the compression test between a tough BMG and a brittle composite where friction in compression has resulted in a large amount of plasticity? The semi-unconstrained loading of a bending test (combining both a compressive and tensile surface) screens out alloys that are brittle and makes direct comparisons possible. In this chapter we have shown that several BMGs display different amounts of plastic bending strain, indicating their varying degrees of fracture resistance or toughness. Why BMGs exhibit different toughness despite having the same amorphous structure is still an interesting question. We have noticed that as Poisson's ratio increases, bending strain increases. As we discuss in Section 4.3, a Pt-Ni-Cu-P alloy was developed with very high Poisson's ratio and exhibited the highest bending strain of any BMG. However, this alloy also exhibits negligible ductility in uniaxial tension tests, as with all BMGs. Designing BMGs to simply have a high Poisson's ratio is impractical, and thus designing monolithic BMGs with ductility is currently not possible. As we discuss in the next section, what we can learn from bending tests is that plasticity is greatly enhanced when the plastic zone radius in front of a crack tip (determined from fracture toughness) is larger than a certain length scale related to the beam thickness in bending.

3.7 Bending Tests, Plastic Zone Size, and Fracture Toughness

Three very detailed studies have been performed on the physics governing bending in metallic glass plates and beams [1, 4, 19]. In these studies, bending equations are derived to explain the growth and spacing of shear bands in relationship to beam thickness. These papers do not attempt to identify why BMGs exhibit very different plastic bending strains but they do clearly explain a size effect that occurs while increasing the beam height. Going from thin ribbons to bulk glasses (> 1 mm thick) BMGs undergo a transformation whereby the alloy is stable in bending until it reaches a critical thickness, at which point it fails in a brittle manner. In fact, [4] indicates that the fracture strain in bending varies inversely with the square of the sample thickness. In [19], this claim was contested and fracture strain was shown to vary inversely with beam thickness, not the square of beam thickness. Shear band spacing has also been shown to vary linearly with sample thickness, displaying an approximate 1:10 relationship between the spacing of the shear bands and the sample thickness [4]. For a brittle BMG in bending, failure occurs with a single shear band. As plastic bending strain increases, the number of shear bands increases and their relative spacing decreases.

To understand how a metallic glass can become stable against fracture in bending, we need to first investigate the plastic zone in front of a crack tip. The stress components at the tip of a crack for mode I, II, and III are given by [20]. Although not presented here, in each case stress is related to geometry by a factor of $K/\sqrt{2\pi r}$, where K is the stress intensity and r is the radius from the tip of the crack. The stress intensity factor, K, describes external conditions and contains contributions from the applied

stress and the crack dimensions. The critical value of stress intensity, denoted K_C, depends on the sample dimensions. In thin samples, where thickness effects play a role in fracture, K_C is said to be in plane-stress conditions. When the thickness is sufficiently large that no thickness effects are observed, K_C is denoted K_{IC} and is said to be in plane-strain conditions. It is important for discussions in the next chapter to note that K_{IC} is independent of sample thickness, K_C depends on sample thickness, and K varies from one system to another.

It is also important to note that the equations for stress at a crack tip contain a $\sqrt{r}$ singularity. This implies that the stress becomes infinite at the tip of a crack. For most materials, yielding near the crack tip is observed, which relaxes the singularity in stress. During yielding, the crack tip becomes blunted, creating two new crack surfaces without advancing the crack, see Figure 3.8 (adapted from [20]). The volume of material at the tip of the crack that participates in yielding is generally given a radius, r_p (sometimes denoted r_y or R_p), which is called the crack tip "plastic zone radius." Material far away from the crack tip can "feel" or "see" the crack as a result of the stress field generated by the plastic zone. In metallic glasses, cracks are blunted by shear bands that form at the crack tip (see Figure 3.3 and Figure 4.3(c)), and the length of these shear bands can be denoted as $2r_p$. In the simplest case, the plastic zone can be approximated by a cylinder with radius r_p. Stress intensity can be defined generally using the stress, σ, and crack length, a as

$$K = \sigma\sqrt{\pi a} \ . \tag{3.16}$$

For a cylindrical plastic zone size we can relate stress intensity to the yield strength, σ_y, and the plastic zone radius, r_p (which is one half of the crack length) as

$$\sigma_y = \frac{K}{\sqrt{2\pi r_p}}. \tag{3.17}$$

Therefore we can approximate the plastic zone radius by solving for r_p

$$r_p = \frac{1}{2\pi}\left(\frac{K}{\sigma_y}\right)^2. \tag{3.18}$$

This equation works well for the case of plane stress but in the case of plane strain, a factor of $1/(6\pi)$ is used instead of $1/(2\pi)$ [20]. However, typical observations regarding plastic zone size are done on the sample's surface, where plane stress conditions are in effect. Thus, we will use the form of Equation 3-18 for our geometric arguments. In the case of a mode I crack, stress intensity, K, is written as K_{IC}, and is called plane strain fracture toughness.

To ultimately design composites in bulk dimensions (for example, 3 mm tension specimens) that exhibit high resistance to fracture and ductility, it is important to understand how long a shear band can become before it nucleates a catastrophic crack. This allows microstructural stabilization mechanisms to be applied to prevent shear bands from reaching this length. Therefore, it is important to know the fracture toughness and the plastic zone size of each metallic glass, which is defined by the length of shear bands that form at the crack tip during mode I failure. For every metallic glass tested in mode I, there will be a shear band length that defines the plastic zone size and this length will increase with increasing fracture toughness. Each shear band is accompanied by a shear offset at its base and this offset grows with applied stress. At a critical shear band length, the shear offset reaches a critical value and the crack grows.

Figure 3.3 can be used to estimate the fracture toughness for the $Cu_{47.5}Zr_{47.5}Al_5$ ternary glass. The plastic zone can be physically observed on the sample's surface for a mixed-mode crack, and the plastic zone radius is simply one half of this value. When measuring fracture toughness, there are multiple geometries that can be used. Toughness can be measured in modes I–III or in mixed modes, and the samples can be in plane-stress, plane-strain, or a combination. In all geometries, the lowest value for fracture toughness is when mode I is measured in plane-strain, so-called K_{1C}. Typically, all other geometries will overestimate K_{1C}. Thus, the mixed-mode crack in Figure 3.3 can be used as an overestimate for K_{1C}. From the figure, $Cu_{47.5}Zr_{47.5}Al_5$ exhibits r_p ~ 225–300 μm. Using a yield stress of σ_y = 1547 MPa [7], this corresponds to a partial plane-stress fracture toughness of K_C ~ 58–67 MPa $m^{1/2}$, a very respectable overestimate compared to other BMGs. Typically Fe-based BMGs exhibit K_{1C} < 10 MPa $m^{1/2}$, Vitreloy 1 exhibits K_{1C} = 20–50 MPa $m^{1/2}$ (depending on the reference), and the Zr-Ti-Cu-Be that we use later in Chapter 4 as the matrix for our composites exhibits K_{1C} ~ 80 MPa $m^{1/2}$ (although this value may be inflated due to plane-stress effects). Thus, using the plastic zone in front of a mixed-mode crack, we obtain a value for fracture toughness that matches our observations from bending tests quite well.

To determine the maximum spatial length of shear bands originating at a crack tip before fracture ensues, which can be thought of as $2r_p$, two simple methods can be used. Beams can be cast, polished, notched, cyclically loaded, precracked and then the shear bands can be observed at the tip of the pre-crack. This is the general procedure used in Chapter 4 to measure K_{1C}. We can also use bending tests to determine the maximum beam thickness where plastic strain is observed.

According to the derivations found in [1, 4, 19], plastic bending strain decreases as beams become thicker. At some critical beam height, which we denote as D_C (also called h^* [19]), a metallic glass beam will exhibit zero plasticity and will fail on one shear band. Below D_C, multiple shear bands will form and bending plasticity will be observed. In the case of a beam at D_C, the first shear band that forms will propagate from the tensile surface towards the neutral stress axis, creating a shear offset that is at a critical value, denoted Δu^* in [4] and $\Delta u_{\max}$ in Section 3.5. The shear offsets can be seen in Figure 3.4 for the $Cu_{47.5}Zr_{47.5}Al_5$ ternary glass. When the shear offset reaches this critical value, the shear band is transformed into a mixed-mode crack, which results in failure of the beam. In other words, when a metallic glass beam is bent past the point of yielding (typically > 2% strain) shear bands will form that grow to a certain depth, s, that is smaller than the neutral axis of stress [4]. If a shear band can grow to this length before the stress intensity at the surface reaches the fracture toughness of the glass, then bending is considered stable. If we assume that s is at the neutral stress axis (which is half the beam height for symmetric bending), the length of a shear band is approximately $D/\sqrt{2}$, since shear bands are assumed to grow at a 45° angle. If we are at the critical beam thickness D_C, then the edge of sample is at the fracture toughness of the glass and a mixed-mode crack develops with length $a = 2r_p \sim D_C/\sqrt{2}$. Therefore, fracture will occur in a bent BMG plate of thickness D when

$$r_p < \frac{D}{2\sqrt{2}} = 0.35D. \tag{3.19}$$

Experimentally, s is typically less than half of the beam height. If we look at Figure 3.9, showing shear bands in a bent metallic glass plate, we can see that

deformation is close to symmetric and shear bands grow from both the tensile and compressive surfaces, stopping before they reach the neutral axis of stress. Recently, experiments have been performed on the composite alloys from Chapter 6, along with several others, to determine the relationship between r_p and the critical beam thickness where bending is stable. Fracture toughness values were obtained and then beams of increasing thickness were bent to estimate the critical beam size. These experiments, which will be the subject of future work, indicate that at the critical beam thickness where bending is stable, $r_p \sim 0.15–0.2\ D$—about half the value we derive in Equation 3.19. From a scaling argument, however, we can say that in the case where $r_p > D/2$, stability against crack opening is geometrically assured.

We can now estimate the strain at failure of a bent BMG plate from [19]:

$$\varepsilon_f \approx \frac{\Delta u_{\max}}{2\gamma D}, \tag{3.20}$$

where γ is a material constant that relates the shear band spacing, λ, with the depth that shear bands grow, s, through the relationship $\lambda = 2s\gamma$. It can be said that a wire or thin beam of metallic glass is ductile if the strain to failure is equal to or greater than 0.1 or 10% [19]. Therefore, Equation 3.20 can be rewritten to express the transition for which a beam experiences ductile to brittle failure as

$$D_C = 5\left(\frac{\Delta u_{\max}}{\gamma}\right), \tag{3.21}$$

which relates the critical beam thickness with the maximum shear band offset before cracking occurs. As we can see, the fracture toughness of a metallic glass and the length scale r_p are related to the thickness of a bent beam and the maximum shear band offset.

Of course, the geometric arguments described above have more rigorous definitions. We can say that unstable crack growth and fracture occur when the stress intensity K_I for a mode I crack perpendicular to the surface of a bent BMG plate exceeds the fracture toughness of the BMG, K_{IC}. The equation for K_I can be obtained from fracture mechanics and takes the form of

$$K_1 = \left[\left(\frac{2G}{(1-\nu)}\varepsilon_y\left(\frac{3}{2}-\frac{1}{2}\left(\frac{\varepsilon_y}{\varepsilon}\right)^2\right)\right)\sqrt{a\pi}\left(1.12-\frac{1.39}{2}\left(\frac{a}{D}\right)+\frac{7.3}{4}\left(\frac{a}{D}\right)^2-\frac{13}{8}\left(\frac{a}{D}\right)^3+\frac{14}{16}\left(\frac{a}{D}\right)^4\right)\right]$$

where G is the shear modulus, ν is Poisson's ratio, a is the crack length, ε_y is the yield strain, and D is the beam thickness [4]. Fracture occurs when $K_1 > K_{1C}$. We can plug in the equation $K_{1C} = \sigma_y\sqrt{2\pi r_p}$ and then solve for r_p such that we get an equation of the form

$$r_p < \frac{1}{2\pi}\left(\frac{K_1(D)}{\sigma_y}\right)^2, \tag{3.22}$$

where $K_1(D)$ represents the stress intensity as a function of the beam height. The strain needed to initiate cracking at the surface of the beam can be defined from [4] as

$$\varepsilon_i = \varepsilon_y + \frac{\alpha D}{2}\left(1+\sqrt{1+\frac{4\varepsilon_y}{\alpha D}}\right), \tag{3.23}$$

where the material parameter α is defined as

$$\alpha = \frac{(1-\nu)}{(1-2\nu)}\frac{\Delta u_{\max}}{\sqrt{2}D^2}. \tag{3.24}$$

For a 1 mm beam of the ternary alloy $Cu_{47.5}Zr_{47.5}Al_5$, we can calculate the strain needed to initiate cracking in the plate. For ν = 0.365, $\Delta u_{\max}$ = 15.4 μm, and ε_y = 0.02, we calculate the strain needed to initiate cracking is ε_i = 0.059 or 5.9%. This value

closely matches the total strain to failure of 6.1% that we calculated in Section 3.5 using the shear band spacing. Using Equation 3.20, we can estimate the material parameter γ using the value for ε_i such that γ = 0.13. We can plug this value into Equation 3.21 to estimate the critical beam thickness where the transition occurs between ductile and brittle bending. Using this method, we estimate the critical beam thickness is D_C = 0.6 mm or 600 μm. Below this thickness, we expect that a beam of the BMG $Cu_{47.5}Zr_{47.5}Al_5$ will be completely stable in bending (in other words, it will have a strain to failure of > 0.1 or 10% before fracture). Earlier, we estimated the plastic zone radius, r_p, to be approximately equal to 225–300 μm for $Cu_{47.5}Zr_{47.5}Al_5$ using a micrograph of a crack tip. We note that a beam of $Cu_{47.5}Zr_{47.5}Al_5$ will be stable in bending when

$$r_p > D_C / 2 , \tag{3.25}$$

which is the same scaling argument that we predicted from geometry. Although this analysis is only approximate, the scaling argument presented here relates the plastic zone size at a crack tip with plasticity in monolithic BMGs.

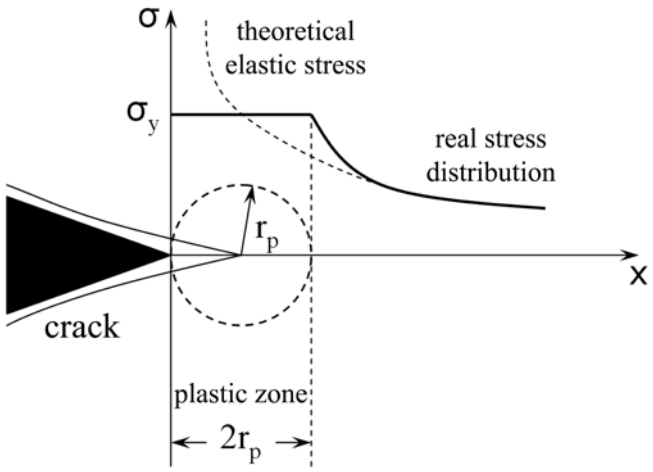

Figure 3.8 – Diagram of the plastic-zone correction at the tip of a crack (adapted from [20]).

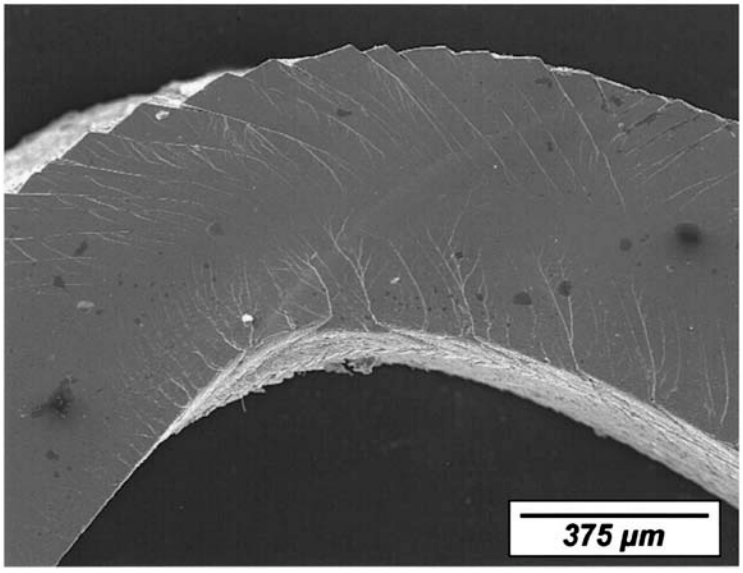

Figure 3.9 – Stable bending in a thin beam of metallic glass showing shear band growth from both the tensile and compressive surfaces (image courtesy of R.D. Conner).

3.8 Conclusion

Every metallic glass exhibits brittle failure at some critical beam thickness. However, when we design BMG composites, we would like bending and tension tests to exhibit ductile failure in dimensions larger than the critical beam thickness of the metallic glass matrix. Therefore, to design composites we need a metallic glass matrix with the highest fracture toughness available, and we need to add ductile inclusions spaced at a distance less than the maximum length of a shear band before it nucleates a crack. In unconstrained loading (like tension tests) we want shear bands to form and propagate and yet become arrested by the microstructure prior to the nucleation of cracks. If it requires more energy to drive the shear band than it takes to form a new one, then multiple shear bands will form and the alloy will exhibit global ductility. This is the strategy we use in the next chapter to create high-toughness BMG composites.

References

1. Conner, R. D., Li, Y., Nix, W. D., Johnson, W. L., *Acta Mater.* **52**, 2429 (2004).
2. Inoue, A., Katsuya, A., Amiya, K., Masumoto, T., *Mater. Trans. JIM* **36**, 802 (1995).
3. Katsuya, A., Inoue, A., Amiya, K., *Int. J. Rapid Solidif.* **9**, 137 (1996).
4. Conner, R. D., Paton, N. E., Nix, W. D., *J. Appl. Phys.* **94**, 2 (2003).
5. Hays, C. C., Kim, C. P., Johnson, W. L., *Phy. Rev. Lett.* **84**, 2901 (2000).
6. Pekarskaya, E., Kim, C. P., Johnson, W. L., *J. Mater. Res.* **16**, 9 (2001).
7. Das, J., Tang, M. B., Kim, K. B., Theissmann, R., Baier, F., Wang, W. H., Eckert J., *Phy. Rev. Lett.* **94**, 205501 (2005).
8. Fan, C., Ott, R. T., Hufnagel, T. C., *Appl. Phys. Lett.* **81**, 6 (2002).
9. Zhang, Z. F., Eckert, J., Schultz, *Acta Mater.* **51**, 1167 (2003).
10. Wang, W. H., Lewandowski, J. J., Greer, A. L., *J. Mater. Res.* **20**, 9 (2005).
11. Xu, D., Duan, G., Johnson, W. L., *Phy. Rev. Lett.* **92**, 24 (2004).
12. Inoue, A., Zhang, W., Tsurui, T., Yavari, A. R., Greer, A. L., *Phil. Mag. & Phil. Mag. Lett.* **88**, 5 (2005).
13. Sun, Y. F., Wei, B. C., Wang, Y. R., Li, W. H., Cheung, T. L., Shek, C. H., *Appl. Phys. Lett.* **87**, 051905 (2005).
14. Beer, F. P., Russell Johnston Jr., E., DeWolf, J. T., *Mechanics of Materials*. (McGraw-Hill, New York, 2001)
15. Sun, B., Wang, Y., Wen, J., Yang, H., Sui, M., Wang, J., Ma, E., *Scripta Mater.* **53**, 805 (2005).

16. Chang, H. J., Park, E. S., Kim, Y. C., Kim, D. H., *Mat. Sci. Eng. A* **406**, 119 (2005).

17. Johnson, W. L., Samwer, K., *Phy. Rev. Lett.* **95**, 195501 (2005).

18. Schroers, J., Johnson, W. L., *Appl. Phys. Lett.* **93**, 25506 (2004).

19. Ravichandran, G., Molinari, A., *Acta. Mater.* **53**, 4087 (2005).

20. Meyers, M. A., Chawla, K. K., *Mechanical Behavior of Materials*. (Prentice Hall, New Jersey, 1999).

Chapter 4

Designing Metallic Glass Matrix Composites with High Toughness and Tensile Ductility*

4.1 Commentary

This chapter represents the major discovery of this thesis. In Appendix A at the end of this thesis, we present the supplementary material necessary to support the technical claims and some important questions raised by the reviewers in *Nature*.

In this chapter, we extend our discussion on length scales from Chapter 3 to design metallic glass matrix composites with high toughness and tensile ductility. What is not obvious from this chapter or from our publication is the BMG matrix material that we used. Our group developed a new Zr-Ti-Cu-Be alloy (GHDT) exhibiting the most impressive properties of any metallic glass. As we discuss in Chapter 5, this new alloy has low density, the largest supercooled liquid region of any metallic glass, eutectic melting and crystallization, large critical casting thickness, low shear modulus, and the highest fracture toughness of any Zr-Ti-based metallic glass.

This chapter also adds far more to the field of metallic glasses than simply new alloy compositions. We present a scientific understanding about how to toughen metallic glasses that is not found in literature. Our discussion is therefore a guide for

* The contents of this chapter are published: Douglas C. Hofmann, Jin-Yoo Suh, Aaron Wiest, Gang Duan, Mary-Laura Lind, Marios D. Demetriou, and William L. Johnson, *Nature*, 451, 1085–1089 (2008).

others to follow to develop ductile BMG composites. Further, our understanding about the formation of composites has allowed us to alter the volume fraction of the soft inclusions from 0–100%, which changes the mechanical and thermal properties. We now understand how to tailor these alloys for specific applications without resorting to trial and error. In conclusion, the alloys presented in this chapter are so far removed from ordinary metallic glasses (especially in terms of fracture toughness) that they open the door for years worth of future research.

4.2 Motivation

The selection and design of modern high-performance structural engineering materials for demanding applications is driven by optimizing combinations of mechanical properties including strength, ductility, toughness, elasticity, and requirements for predictable and graceful failure in service [1]. Highly processable bulk metallic glasses are a new class of engineering materials and have attracted significant technological interest [2–6]. While many BMGs exhibit high strength and show substantial fracture toughness, they lack ductility and fail in an apparently brittle manner in unconstrained loading geometries [7]. For instance, while some BMGs exhibit significant plastic deformation in compression or bending tests, all exhibit negligible plasticity (< 0.5% strain) in uniaxial tension. To overcome brittle failure in tension, BMG-matrix composites were previously introduced [8–9]. The inhomogeneous microstructure, with isolated dendrites in a BMG matrix, stabilizes the glass against the catastrophic failure associated with unlimited extension of a shear band and results in enhanced global plasticity and more graceful failure. Tensile strengths of ~ 1 GPa, tensile ductility of ~ 2–3% [9], and enhanced fracture toughness

K_{1C} ~ 40 MPa-$m^{1/2}$ were reported [8–9]. Building on this approach, we have developed "designed composites" by *matching of key fundamental mechanical and microstructural length scales*. In this chapter, we report new exemplary BMG composites with benchmark engineering properties. Room-temperature tensile ductility exceeding 10%, yield strengths of 1.2–1.5 GPa, mode I fracture toughness up to K_{1C} ~ 170 MPa-$m^{1/2}$, and fracture energies for crack propagation, G_{1C}, as high as ~ 340 kJ/m^2 are reported for the new Ti-Zr-based BMG composites. The K_{1C}, and more particularly the G_{1C}, values equal or surpass those achievable in the toughest titanium or steel alloys placing BMG composites among the toughest known materials of any kind.

4.3 Discussion of Fracture Toughness

Researchers frequently use uniaxial compression tests to assess ductility of BMG materials because it differentiates glassy alloys that all lack tensile ductility [10–21]. Under compression, an operating shear band is subject to a normal stress that closes the band. Variations in local material properties caused, for example, by nanoscale inhomogeneities [20] and frictional forces (due to closing stresses) combine to arrest persistent slip on individual shear bands. Multiple shear bands are sequentially activated giving rise to global plasticity (~ 1–10% strain). A geometry that better differentiates the ductility is bending. Here, the sample is subject to both compressive and tensile stresses. Shear bands initiate on the tensile surface but are arrested as they propagate toward the neutral stress axis [22, 24]. Deformation is stable unless the shear band at the tensile surface evolves to an opening crack [23, 24]. In bending, plasticity is dramatically enhanced when the characteristic dimension, R_P, of a crack tip "plastic zone" exceeds ~ $D/2$, where D is sample thickness [22, 23] and R_P is a material length

scale related to fracture toughness. For a mode I opening crack, it can be expressed as [25]

$$R_P \approx (1/2\pi)(K_{1C}/\sigma_Y)^2.$$

R_P varies from ~ 1 μm up to ~ 1 mm on going from relatively brittle to tough BMGs [26]. R_P is associated with the maximum spatial extension (band length) of shear bands originating at an opening crack tip. For a specific geometry (e.g., a mode I opening crack in tension tests), R_P is related to a maximum allowable shear offset along the band [23, 24]. In bending, the most ductile BMG reported is $Pt_{57.5}Cu_{14.7}Ni_{5.3}P_{22.5}$, with R_P ~ 0.5 mm (K_{1C} = 83 MPa-$m^{1/2}$). A 4-mm-thick square beam showed 3% plastic bending strain without cracking [27]. Despite large bending and compressive ductility, the $Pt_{57.5}Cu_{14.7}Ni_{5.3}P_{22.5}$ glass has negligible (< 0.5%) ductility in uniaxial tensile tests. In tension, the opening stress on the shear bands enhances strain softening and instability, frictional forces are absent, and a propagating shear band lengthens and slips without limit. Cavitation ultimately ensues within the slipping band and an opening failure follows.

Suppression of tensile instability requires a mechanism to limit shear band extension. Bending produces an inherently inhomogeous stress state where a shear band is arrested by the gradient in applied stress, $\nabla\sigma = 2\sigma_Y/D$. Stability against crack opening is geometrically ensured when $D/2 < R_P$ [23, 24]. Under uniaxial tension, applied stress is uniform. By introducing inhomogeneity in elastic or plastic material properties at a microstructural length scale L, "microstructural" stabilization mechanisms become possible. Shear bands initiated in plastically soft regions (e.g., lower σ_Y or lower shear modulus, G) can be arrested in surrounding regions of higher

yield stress or stiffness. Stabilization requires that $L \sim R_P$. This fundamental concept underlies enhancement of ductility and toughening and is similar to that employed in toughening of plastic by inclusion of rubber particles [28].

4.4 Designing the New Composites

Compared to previous in-situ composites, the new BMG composites have increased Ti content to reduce density and contain no Ni. Removal of Ni enhances fracture toughness of the glass and suppresses nucleation of brittle intermetallics during processing. Three alloys, $Zr_{36.6}Ti_{31.4}Nb_7Cu_{5.9}Be_{19.1}$, $Zr_{38.3}Ti_{32.9}Nb_{7.3}Cu_{6.2}Be_{15.3}$ and $Zr_{39.6}Ti_{33.9}Nb_{7.6}Cu_{6.4}Be_{12.5}$, (DH1–3, respectively) are discussed. The Be content, x = 12.5–19.1, is varied while fixing the mutual ratios of Zr, Ti, Nb, and Cu. As x decreases, one obtains an increasing volume (or molar) fraction of dendritic phase in a glass matrix. SEM, EDS, and XRD analysis show that the composition of the dendrites and glass matrix remain approximately constant with varying x. The dendritic phase is a b.c.c. solid solution containing primarily Zr, Ti, and Nb, as verified by X-ray and EDS analysis. DH1–3 partition by volume fraction into 42%, 51%, and 67% dendritic phase in a glass matrix, respectively. These percentages were obtained by analyzing the contrast from SEM images using computer software. They were independently verified by analyzing the heat of crystallization from DH1–3 in DSC scans relative to the heat of crystallization from a fully glassy matrix alloy (see Appendix A). Dendrite compositions measured using EDS range over $Zr_{40–44}Ti_{42–45}Nb_{11–14}Cu_{1–3}$, while glass matrix compositions range over $Zr_{31–34}Ti_{17–22}Nb_{1–2}Cu_{9–13}Be_{31–38}$. These are reported with an estimated error of 1 at.%. The volume fraction of dendritic phase can be controlled by varying x (though not presented here) from 0 to 100%. Ultrasonic

measurements for the composites give average elastic constants following a “volume rule of mixtures” with varying x. In DH1, for example, a shear modulus G = 33.2 GPa (28.7 GPa), and Young’s modulus E = 89.7 GPa (78.3 GPa) are obtained for glass matrix phase and dendritic phases, respectively. The two-phase composite has a volume weighted average value of the two, G = 30.7 GPa and E = 84.3 GPa. The dendrites are elastically soft inclusions relative to the matrix (see Appendix A). Under loading, yielding and deformation are promoted in the dendrite vicinity and limited by the surrounding matrix.

Earlier reported “in-situ” composites [8, 9] were solidified from the melt in an arc melter. Due to cooling rate variations with the ingots, the overall dendrite length scale and interdendrite spacings showed large variation from ~ 1–100 μm [8, 21]. To produce a more uniform microstructure, the present alloys were heated into the semi-solid two-phase region (T = ~ 800–900 °C) between the alloy liquidus and solidus temperature [21] and held there isothermally for several minutes, remaining entirely below the molten state (T > 1100 °C). The semi-solid mixture was then quenched sufficiently rapidly to vitrify the remaining liquid phase. This process yields a more uniform “near equilibrium” two-phase microstructure throughout the ingot, which was characterized using TEM, as shown in Figure 4.1. A bright-field/dark-field pair showing the b.c.c. dendrite in the glass matrix is shown in Figure 4.1(a–b) for the alloy DH1. The interface between a dendrite and the glass matrix is shown in high resolution in Figure 4.1(b). The micrograph confirms that the interface between the two phases is atomically sharp. Diffraction patterns are shown in the insets of Figure 4.1(c) for both the dendrite and the matrix glass. The dendrite exhibits a b.c.c. diffraction pattern,

while the glass matrix exhibits two broad diffuse halos typical of an amorphous material. The dendrite/glass interfaces in DH2–3 are similar to those seen in Figure 4.1.

SEM analysis was used to characterize the bulk microstructure of the composites. Two selected areas are shown in Figure 4.2(a–b) for the alloys DH1 and DH3. After analyzing an array of micrographs, dendrite size was found to vary over L ~ 60–120 μm, while inter-dendrite spacings vary over S ~ 80–140 μm. (The interdendrite spacing is the distance from the center of a single dendrite tree to the center of an adjacent one, while the dendrite size is the total spanning length of a single dendrite tree.) Primary or secondary "trunk" diameters noticeably increase from DH1 to DH3 with DH1 (DH3) exhibiting a more (less) developed tree structure. The rationale for selecting these microstructures lies in uniformly matching the length scales L and S to be less than, but of order, R_P. The R_P for the glass matrix can be estimated from its K_{1C} ~ 70 MPa-$m^{1/2}$, to be R_P ~ 200 μm.

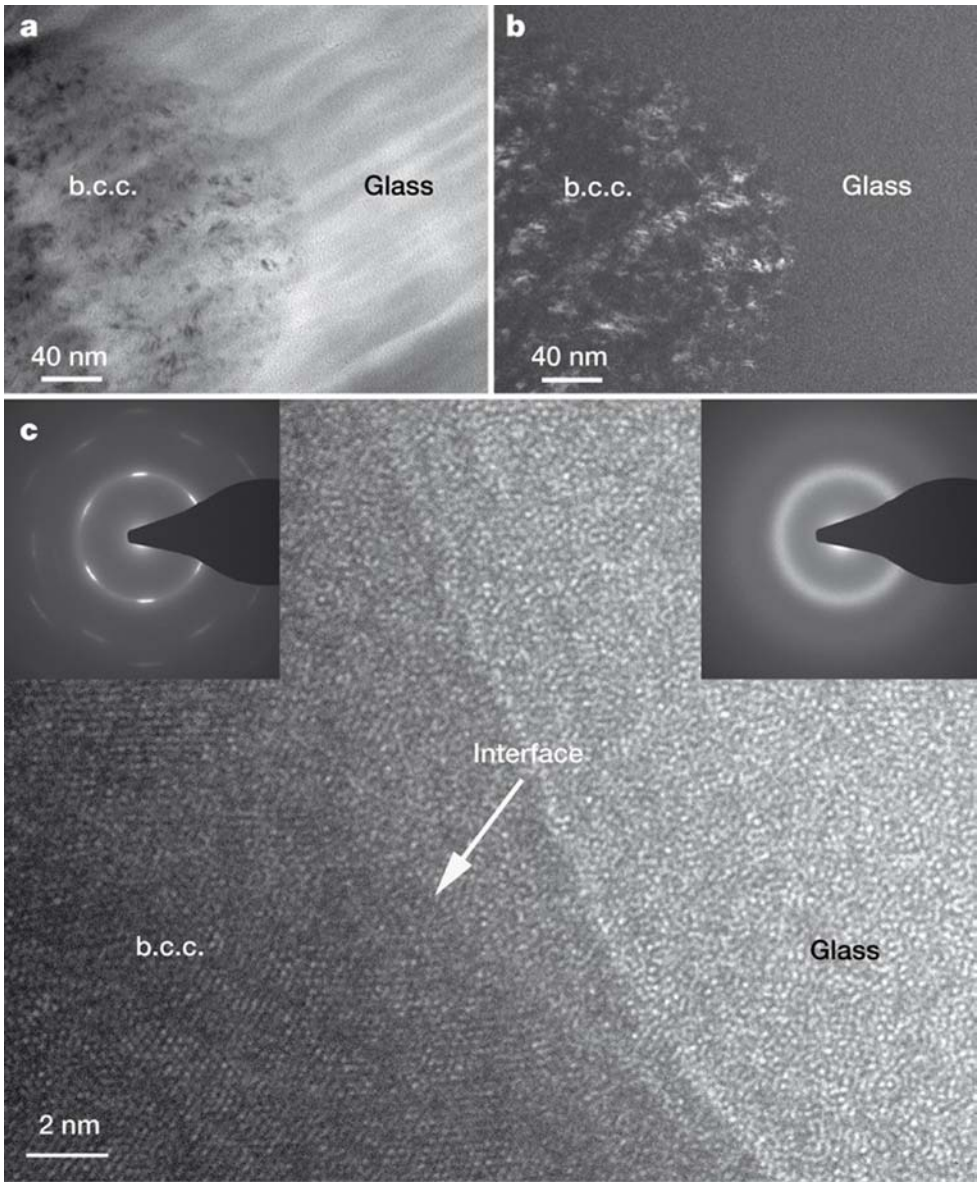

Figure 4.1 – (a) Bright-field TEM micrograph showing a b.c.c. dendrite in the glass matrix and (b) the corresponding dark-field micrograph of the same region. (c) A high-resolution micrograph showing the interface between the two phases with corresponding diffraction patterns shown in the inset.

4.5 Room-Temperature Tension Tests

The room temperature engineering stress-strain tensile curves for DH1–3 (Figure 4.2(c)) show total strain to failure ranging from 9.6–13.1% at ultimate tensile strengths of 1.2–1.5 GPa. Sample-to-sample variation in total strain was typically ± 1%, and variation in strength was typically ± 0.1 GPa. The stress decreases at large strains due to necking in the gauge section. The alloy DH2, demonstrates the most necking (50% reduction in area), and fails at a true stress of 2.15 GPa in the necked region. Optical images of tensile gauge sections in DH2–3 are shown in Figure 4.2(d–e). The in-situ composites exhibit plastic elongation of approximately 1.3 mm (8.6%) and 1.7 mm (11.3%) from their undeformed gauge lengths of ~ 15 mm. Figure 4.2(g–h) shows the necked regions from DH2–3 at higher magnification. In contrast, monolithic BMGs fail on a single shear band oriented at roughly 45^o (Figure 4.2(i)). The observed tensile ductility of DH1–3 is associated with patterns of locally parallel primary shear bands that form in domains defined by individual dendrites (Figure 4.2(f), taken near the necked region). The primary shear bands have a dominant spacing of $d_P \sim 15$ μm, or roughly $S/10 \approx L/10$. The plane of shear slip of the primary bands changes orientation (often by a 90^o rotation) on moving from one dendrite domain to a neighboring dendrite domain. The length of individual primary shear bands (~ 60–100 μm) is of order L (and S), and somewhat less than but of the order of R_P. The inset of Figure 4.2(f) shows a magnified image of secondary shear band patterns between two primary shear bands. Dense secondary shear bands with spacing d_S ~ 1–2 μm are uniformly distributed within primary bands. It is noteworthy that $d_P \sim L/10$ and $d_S \sim d_P/10$. Similar geometric

"scaling" of shear band spacings is also observed for primary/secondary patterns in bending experiments [23–24].

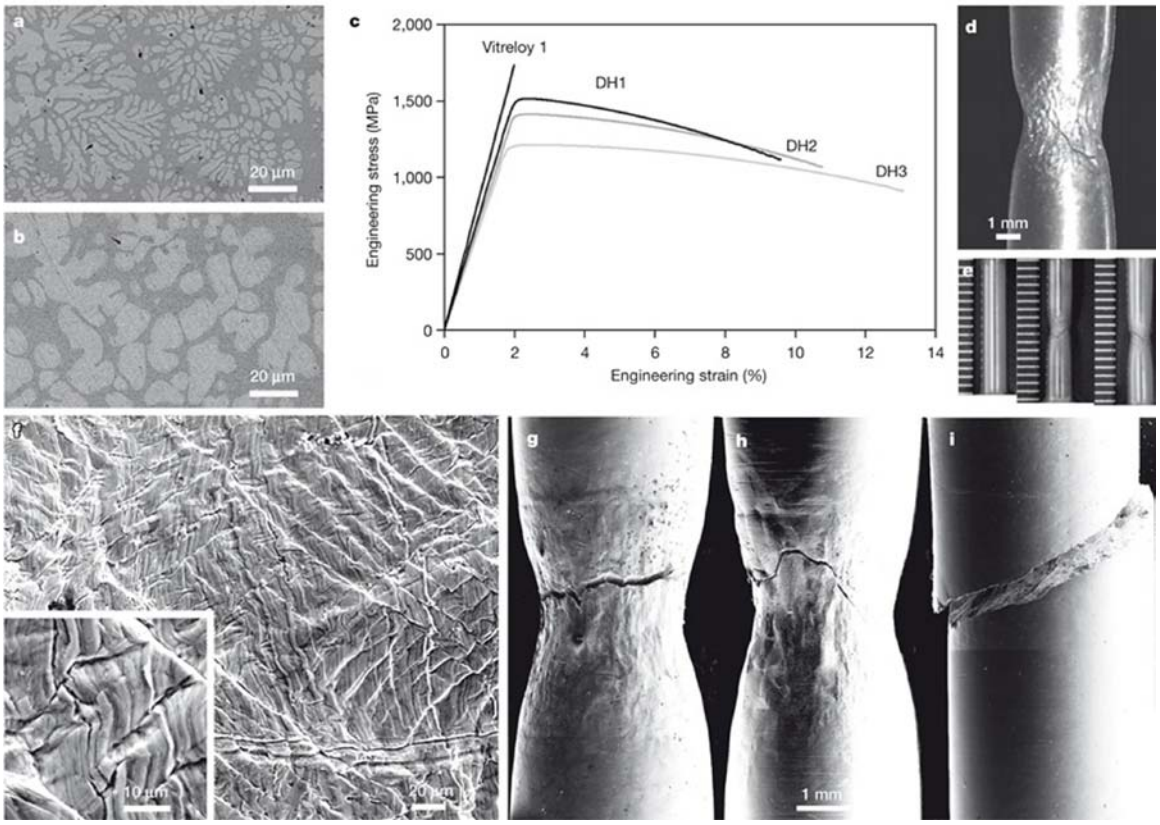

Figure 4.2 – Backscattered SEM micrographs showing the microstructure of (a) DH1, (b) DH3 where the dark contrast is from the glass matrix and light contrast is from the dendrites. (c) Engineering stress-strain curves for Vitreloy 1 and DH1–3 in room-temperature tension tests. (d) Optical micrograph of necking in DH3. (e) Optical micrographs showing an initially undeformed tensile specimen contrasted with DH2-3 specimens after tension testing. (f) SEM micrograph of the tensile surface in DH3 with higher magnification shown in the inset. SEM micrographs of necking in (g) DH2 and (h) DH3. (i) Brittle fracture representative of all monolithic BMGs.

4.6 Fracture Toughness Tests

Mode I fracture toughness tests in the three-point-bend geometry (K_{1C}) were used to assess resistance to crack propagation of DH1–3 (illustrated in Figure 4.3(a)). From an initial cut notch, a pre-crack was generated by fatigue cracking. On subsequent loading, extensive plasticity is observed prior to crack growth. While the load displacement curves start to turn over at a stress intensity of K = 55–75 MPa-$m^{1/2}$, unloading compliance shows that failure at the blunted pre-crack front initiates much later. Thus, the J-integral and J-R curves were used to assess K_{1C} according to method ASTM E399.A3 and formula ASTM E1820. In fact, the final propagating crack was arrested before sample failure occurred (Figure 4.3(b)). This contrasts sharply with the behavior of monolithic BMGs (Figure 4.3(c)) where crack arrest is never observed. Although an array of shear bands form at the pre-crack tip, the monolithic glass fails catastrophically along a single shear band when overloaded. Figures 4.3(d–e) are backscattered SEM micrographs of the arrested crack tip in DH1 and DH3 showing a complex plastic zone with primary and secondary shear band patterns. DH3, which has the highest fracture toughness, exhibits more extensive deformation at the crack tip than DH1 (Figure 4.3(d–e). High-resolution SEM was used to image the shear band formation in the interdendrite regions, shown in Figure 4.3(f). Primary and secondary shear band patterns are visible with spacing 5–10 μm and 0.3–0.9 μm, respectively. This matches closely with the secondary-to-primary shear band relation $d_S \sim d_P/10$. The fracture toughness (K_{1C}) of DH1–3 were estimated to be 87 MPa $m^{1/2}$, 128 MPa $m^{1/2}$, and 173 MPa $m^{1/2}$. DH1–3 have high K_{1C} in load-limited failure, but have extremely high values of G_{1C} ($\approx K_{1C}^2/E$) in energy-limited failure (due in part to their

relatively low Young's modulus). For example, the fracture toughness of DH3 is $K_{1C} \sim 173$ MPa $m^{1/2}$, while the fracture energy is $G_{1C} \sim 341$ kJ/m^2. This is comparable to G_{1C} in highly toughened steels which have nearly three times higher stiffness than DH3 ($E \sim 200$ GPa versus $E = 75$ GPa). It is noteworthy that the apparent plastic zone radius, R_P, of the composite is several mm's (Figure 4.3(a)), comparable to many structural crystalline metals.

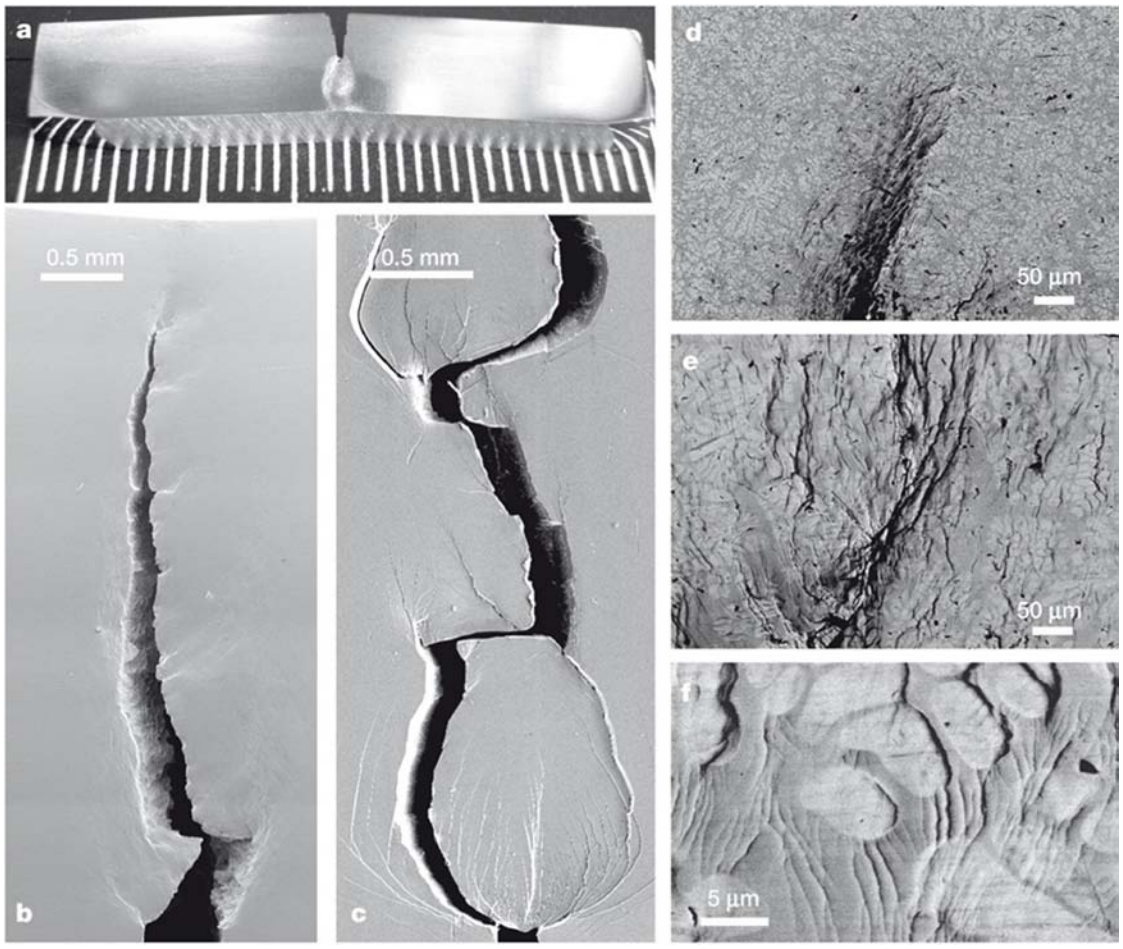

Figure 4.3 – (a) Optical image of an unbroken fracture toughness (K_{1C}) specimen in DH1 showing plasticity around the crack tip on the order of several mm. (b) SEM micrograph of an arrested crack in DH1 during a K_{1C} test. (c) SEM micrograph of K_{1C} test in Vitreloy 1. Backscattered SEM micrographs showing the plastic zone in front of the crack in (d) DH1 and (e) DH3. (f) Higher magnification SEM micrograph of DH3 showing shear bands on the order of 0.3–0.9 µm.

4.7 Ashby Map—Comparing Properties

To illustrate the unusual properties of the new composites, an "Ashby Map" used for selection of materials in load, deflection, and energy limited structural applications is shown in Figure 4.4. The two axes are Fracture Toughness (K_{1C}) and Young's Modulus (E), while the parallel dashed lines correspond to constant G_{1C} contours. Whereas the K_{1C} values of DH1–3 are comparable to those of the toughest steels and crystalline Ti alloys, the G_{1C} values appear to pierce the limiting envelope defined by all alloys. The new BMG composites have benchmark G_{1C} values.

Table 4.1 summarizes some of the properties observed for DH1–3. The properties are compared with those of monolithic BMGs and with earlier reported composites. Space precludes discussion of other data obtained. For example, Charpy impact energies were measured and found to be of order 40–50 J/cm^2, much higher than values for either monolithic glass or previous composites (Table 4.1). These results will be discussed in a later publication. Further details regarding the current alloys are shown in Appendix A. These include X-ray diffraction scans, DSC curves, optical images, and backscattered SEM micrographs.

We conclude by noting that the present materials were created using the strategy of *microstructural toughening and ductility enhancement* in metallic glasses, as described in the text. The basic principles are: (1) introduction of "soft" elastic/plastic inhomogeneities in a metallic glass matrix to initiate local shear banding around the inhomogeneity, (2) matching of microstructural length scales (e.g., L and S) to the characteristic length scale R_P (for plastic shielding of an opening crack tip) to limit shear band extension, suppress shear band opening, and avoid crack development.

These principles are applicable to other ductile-phase reinforced metallic glass systems in the event that several criteria are met. The new alloy system must be comprised of a highly processable metallic glass in which a shear-soft dendritic phase nucleates and grows while the remaining liquid is vitrified on subsequent cooling. At least one other alloy system has been reported that successfully uses this strategy [30]. A BMG matrix composite was discovered in $La_{74}Al_{14}(Cu,Ni)_{12}$ whereby 5% tensile ductility was achieved with 50% volume fraction of soft second phases. Although the La-based composite exhibited an ultimate tensile strength of only 435 MPa, the alloy demonstrated that the properties of the monolithic metallic glass ($La_{62}Al_{14}(Cu,Ni)_{24}$) could be greatly improved through the introduction of a soft second phase. Other desirable composite systems are those with lower density (as with Al-containing alloys) or with higher strength (as with Fe-based alloys).

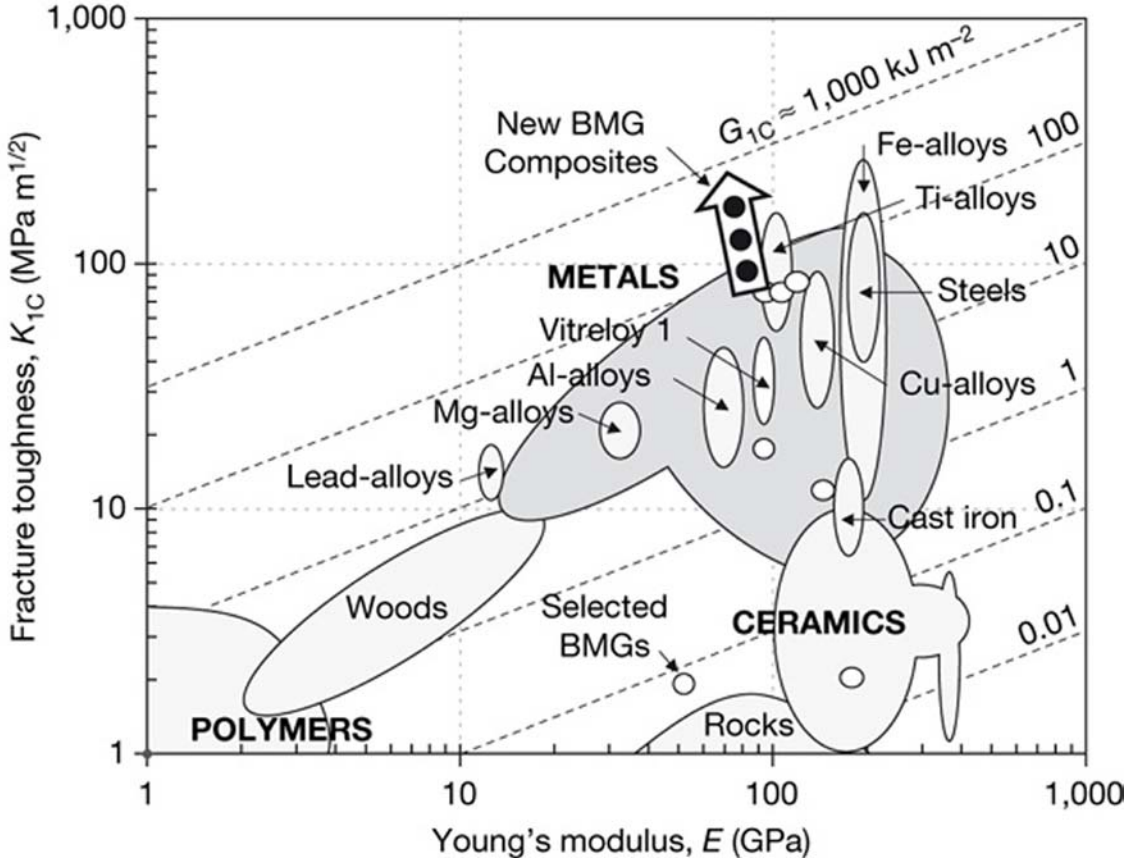

Figure 4.4 – An Ashby plot for materials selection showing fracture toughness (K_{1C}) versus Young's modulus (*E*). The dashed contour lines are fracture energies for crack propagation (G_{1C}) with each line being separated by an order of magnitude. The plot shows a large range of common engineering materials, along with selected metallic glass ribbons and BMGs. Due to their high K_{1C} with low stiffness, the semi-solidly processed composites DH1–3 (Zr-Ti-Nb-Cu-Be) have among the highest G_{1C} for all known engineering materials.

4.8 Experimental Method

Master ingots were prepared by arc melting ultrasonically cleansed pure elements under a Ti-gettered argon atmosphere. The master ingots were then placed in a water-cooled Cu boat and heated (again under a Ti-gettered argon atmosphere) via induction, with the temperature monitored by pyrometer. The final shape of the ingots ranged from 6–15 mm thick and 40–60 mm long with total ingot mass of 10–35 g. Mechanical test samples were machined from ingots.

ASTM standard tension tests were prepared in proportion with the ASTM E8M standard. The diameter of the gauge section was between 3.00–3.05 mm and the gauge length was between 15.15–15.25 mm. The tests were performed at room temperature on a calibrated Instron 5500R load frame. The tests were done with a constant crosshead displacement rate of 0.1 mm/min. The elastic strain was measured by extensometer and the total strain was measured both by a linear variable displacement transducer (LVDT) attached to the sample fixture and by machine crosshead. The decrease in area was measured by a Leo 1550 VP Field Emission SEM in conformance to ASTM standards.

Fracture toughness samples were prepared with dimensions 2.4–2.6 mm thick × 7.6–8.4 mm wide × 36 mm long and were polished for observation of surface shear bands after fracture. An initial notch was made in the middle of one side using a wire saw. From the notched end, a pre-crack was generated by fatigue cracking with 5 Hz of oscillating load (applied by MTS hydraulic machine equipped with 3-point-bending fixture having 31.75 mm span distance.) Load level was kept at approximately $\Delta K \cong 10$ MPa $m^{1/2}$, $K_{min}/K_{max} \cong 0.2$ and 2 mm of pre-crack was obtained after 40,000–100,000 cycles. With the initial crack length of 3.7–4.4 mm, the sum of the notch length and

pre-crack, a quasi-static compressive displacement of 0.3 mm/min (K ~ 40 MPa $m^{1/2}$/min) was applied and the load response of the pre-cracked sample was measured. Evaluation of J, a parameter of elastic-plastic fracture mechanics, and the J-R curve by measuring unloading compliance were also performed during the test, as the samples have extensive plasticity before the initial crack propagation. In the samples with high fracture toughness (e.g., DH3), the requirement of sample dimension given by ASTM E1820 is marginally satisfied for the J evaluation. Due to limitations in sample geometry, these J-values were used to estimate K_{1C}. Reduced-size Charpy impact tests were machined proportional to ASTM standard E23-82. The samples were made 5 mm x 5 mm x 55 mm in the U-notch configuration. Charpy tests were performed on a calibrated Riehle impact testing machine.

The pulse-echo overlap technique was used to measure the shear and longitudinal wave speeds at room temperature for each of the samples. The setup included a 3500PR pulser/receiver and 5 MHz piezoelectric transducers from Panametrics, a Tektronix 1500 oscilloscope, and a GPIB interface to a PC-controlled Labview program to capture the pulse and echo waveforms. Sound velocity samples were all greater than 3 mm in thickness and sample surfaces were polished flat and parallel to a surface finish of 9 μm. Sample density was measured by the Archimedean technique according to the American Society of Testing Materials standard C 693-93. The sound velocity, density, and thickness of each sample were measured multiple times and the error propagated. The errors in the calculated values of G, ν, E range from +/- 0.5–0.6% of the stated average value.

Compositions of the dendrites and glass were estimated through electron dispersive X-ray spectrometry (EDS), DSC, and computer software. TEM analysis was performed at the Kavli Nanoscience Institute at the California Institute of Technology using a FEI Tecnai F30UT high-resolution TEM operated at 300 kV. Samples were prepared for TEM observation by microtoming.

Table 4.1 – A comparison between the alloys DH1-3, Vitreloy 1, and the in-situ composite of [8–9] (LM2). The properties listed in the table are yield strength (σ_y), ultimate tensile strength (σ_{max}), yield strain (ε_y), total strain to failure (ε_{tot}), reduction in area (RoA), density (ρ), modulus of elasticity (E), shear modulus (G), Charpy impact toughness (CIT), and Poisson's ratio (ν).

Alloy	σ_{max} (MPa)	ε_{tot} (%)	σ_y (MPa)	ε_y (%)	E (GPa)	ρ (g/cm^3)	G (GPa)	CIT (J)	RoA (%)	ν
$Zr_{36.6}Ti_{31.4}Nb_7Cu_{5.9}Be_{19.1}$ (DH1)	1512	9.58	1474	1.98	84.3	5.6	30.7	26	44	0.371
$Zr_{38.3}Ti_{32.9}Nb_{7.3}Cu_{6.2}Be_{15.3}$ (DH2)	1411	10.76	1367	1.92	79.2	5.7	28.8	40	50	0.373
$Zr_{39.6}Ti_{33.9}Nb_{7.6}Cu_{6.4}Be_{12.5}$ (DH3)	1210	13.10	1096	1.62	75.3	5.8	27.3	45	46	0.376
$Zr_{41.2}Ti_{13.8}Cu_{12.5}Ni_{10}Be_{22.5}$ (Vitreloy 1)	1737	1.98	--	--	97.2	6.1	35.9	8	0	0.355
$Zr_{56.2}Ti_{13.8}Nb_{5.0}Cu_{6.9}Ni_{5.6}Be_{12.5}$ (LM 2)	1302	5.49	1046	1.48	78.8	6.2	28.6	24	22	0.375

References

1. Ashby, M. F., *Materials Selection in Mechanical Design*. (Pergamon Press, Oxford, 1992).
2. Peker, A. and Johnson, W. L., *Appl. Phys. Lett.* **63**, 2342 (1993).
3. Johnson, W. L., *MRS Bull.* **24**, 42 (1999).
4. Ashby, M. F. and Greer A. L., *Scripta Mater.* **54**, 321 (2006).
5. Salimon, A. I., et al., *Mater. Sci. and Eng. A* **375**, 385 (2004).
6. Greer, A. L., *Science* **267**, 1947 (1995).
7. Rao, X., et al., *Mater. Lett.* **50**, 279 (2001).
8. Hays, C. C., Kim, C. P., Johnson, W. L., *Phys. Rev. Lett.* **84**, 2901 (2000).
9. Szuecs, F., Kim, C. P., and Johnson, W. L., *Acta. Mater.* **49**, 1507 (2001).
10. Liu, Y. H., et al., *Science* **315**, 1385 (2007).
11. Hofmann, D. C., Duan, G., and Johnson, W. L., *Scripta Mater.* **54**, 1117 (2006).
12. Fan, C., Inoue, A., *Appl. Phys. Lett.* **77**, 46 (2000).
13. Eckert, J., et al., *Intermetallics* **10**, 1183 (2002).
14. He, G., Löser, W., and Eckert, J., *Scripta Mater.* **48**, 1531 (2003).
15. Lee, M. H., et al., *Mater. Lett.* **58**, 3312 (2004).
16. Lee, M. H., et al., *Intermetallics* **12**, 1133 (2004).
17. Das, J., et al., *Phys. Rev. Lett.* **94**, 205501 (2005).
18. Yao, K. F., et al., *Appl. Phys. Lett.* **88**, 122106 (2006).
19. Eckert, J., et al., *Intermetallics* **14**, 876 (2006).

20. Chen, M., et al., *Phys. Rev. Lett.* **96**, 245502 (2006).

21. Lee, S. Y., et al., *J. Mater. Res.* **22**, 538 (2007).

22. Conner, R. D., et al., *J. Appl. Phys.* **94**, 904 (2003).

23. Conner, R. D., et al., *Acta Mater.* **52,** 2429 (2004).

24. Ravichandran G. and Molinari, A., *Acta Mater.* **53**, 4087 (2005).

25. Meyers M. A., Chawla, K. K., *Mechanical Metallurgy: Principles and Applications.* (Prentice Hall, Englewood Cliffs, New Jersey, 1984).

26. Lewandowski, J. J., Wang, W. H., and Greer, A. L., *Phil. Mag. Lett.* **85**, 77 (2005).

27. Schroers, J. and Johnson, W. L. *Phys. Rev. Lett.* **93**, 255506 (2004).

28. See for example; Liang J. Z. and Li, R. K. Y., *J. of Appl. Polymer Sci.* **77**, 409 (2000).

29. Gu, X. J., Poon, S. J, and Shiftel, G. J., *J. Mater. Res.* **22**, 344 (2007).

30. Lee, M. L., et al., *Acta Mater.* **52**, 4121 (2004).

Chapter 5

New Processing Potential for Highly Toughened Metallic Glass Matrix Composites*

5.1 Commentary

The increased tensile ductility and fracture toughness of the BMG composites reported in Chapter 4 do not explain exactly how the new materials differ from previous metallic glasses in terms of processing. The goal of this chapter is to demonstrate that the new highly toughened composites can be processed in ways that many monolithic glasses cannot be processed. For example, monolithic BMGs exhibit low resistance to fracture and cannot be rolled significantly at ambient temperatures. In contrast, the new composites can be rolled extensively at high strain rates and still preserve their ductility. This chapter further separates the new composites from any reported monolithic BMG or BMG composite in terms of mechanical properties.

5.2 Introduction

Many advances in materials engineering result from combining advantageous properties of several materials into one. Toughened ceramics, for example, combine brittle high-melting temperature ceramics with inclusions that undergo stress-induced transformations, substantially increasing fracture toughness [1]. Similar

* The contents of this chapter are published: Douglas C. Hofmann, Jin-Yoo Suh, Aaron Wiest, and William L. Johnson, *Scripta Mater.* **58**, 684 (2008).

success was recently obtained in metallurgy by marrying relatively brittle but high-strength bulk metallic glasses (BMGs) with mechanically soft crystalline dendrites, creating a new class of crystalline/amorphous metal composites [2]. These alloys have been shown to have high strengths (as with monolithic BMGs), large ductility (as with soft crystalline metals), but fracture toughness substantially exceeding either phase individually [2]. While the strategy for designing these BMG composites is now developed [2–4], the processing potential of these alloys has not been explored. In this research, we demonstrate thermoplastic processing, cold rolling of plates, and work-hardening behavior in an optimized BMG matrix composite. We have found that the tensile necking instability seen in high-ductility BMG matrix composites can be mitigated by cold rolling the samples prior to tension testing. Necking during tensile elongation, which leads to a reduction in area > 40% in highly toughened BMG matrix composites, can be reduced to ~ 20% without substantial loss of overall ductility. Understanding the processing behavior of BMG composites will likely widen the applications for these promising new materials.

5.3 Experimental Method

Samples of the BMG matrix composites were prepared in ingot form by semi-solid processing (see [2]). All samples used for processing were machined directly from these ingots. Thermoplastic processing was completed on a heated hydraulic press with compressive capabilities of 1–20 tons. Processing was done just below the crystallization temperature of the composites, ~ 670 K. Cold rolling was performed on a Stanat rolling mill at ambient temperatures with no oil or lubricant in contact with the sample. Tension tests were performed at ambient temperature on a

calibrated Instron 5500R load frame. The tests were done with a constant crosshead displacement rate of 0.1 mm/min. A Netzsch 404C differential scanning calorimeter (DSC) (performed at a constant heating rate 20 K/min) was used to assess the crystallization behavior of the alloys.

5.4 Thermoplastic Processing

BMG alloys typically have low equilibrium melting temperatures (allowing for net-shape casting) and, in the glassy state, they exhibit a sharp drop in viscosity above their glass transition temperature (allowing for thermoplastic processing in some alloys). Both methods can reduce the cost of producing net-shape BMG parts by eliminating expensive machining. Using thermoplastic forming, a monolithic BMG can be formed or stamped into net-shaped components at temperatures well below the equilibrium alloy melting temperatures, much as polymers are thermoplastically processed [5–7]. Metallic glasses have a metastable liquid region above the glass transition temperature in which the viscosity decreases rapidly until the onset of crystallization. Thermoplastic forming is done in this metastable region under an applied load. The width of the region is defined as $T_x - T_g = \Delta T$, where T_x represents crystallization temperature (defined at a typical heating rate of 10–20 K/min) and T_g represents glass transition. With a large enough ΔT (typically > 100 K), BMGs can be processed well above T_g for several minutes and still be cooled sufficiently rapidly to avoid the onset of crystallization [5]. Previously, thermoplastic forming of BMGs has been carried out mainly with expensive Pt- or Pd-based alloys [9–11]. Recently, a new Zr-Ti BMG, $Zr_{35}Ti_{30}Cu_{8.25}Be_{26.75}$ (G1), was demonstrated to have ΔT = 159 K and superior thermoplastic processability (see [5]). To take

advantage of this, we designed our new BMG composites to yield a glass matrix of constitution similar to G1 (using the toughening strategy described in [2]). In this work, we used one of these alloys, DH1 ($Zr_{36.6}Ti_{31.4}Nb_7Cu_{5.9}Be_{19.1}$ in atomic %, $Zr_{55.3}Ti_{24.9}Nb_{10.8}Cu_{6.2}Be_{2.8}$ in weight %), which is comprised of 58% glass phase by volume and has been processed semi-solidly [2]. Figure 5.1(a) shows a differential scanning calorimetry (DSC) scan from DH1 and its glass matrix (similar to G1 with ~ 3% Nb). Both alloys exhibit a clear glass transition (enlarged in the inset), a single sharp eutectic crystallization event, and a melting event. While the composite DH1 has a smaller supercooled liquid region than its matrix alone (ΔT = 103 K versus ΔT = 123 K), it is nevertheless sufficient for thermoplastic processing (see Figure 5.1(a)). In contrast, previous in-situ composites exhibited ΔT = 45 K—too small to allow for thermoplastic processing before crystallization of the glass phase [3]. Thermoplastic processing was carried out on a heated hydraulic press at ~ 670 K, where the equilibrium viscosity of the glass matrix is on the order of 10^{6-7} Pa-s. Figure 5.1(b) shows an impression of the front of a United States dime on an initially 2-mm-thick wafer of DH1. Despite having 42% volume fraction of dendrites, near perfect replication is achieved if the glass phase reaches a suitably low viscosity. The glass/dendrite composite microstructure remains unaltered after thermoplastic processing and is shown in the inset of Figure 5.1(b). Despite the deformation, the dendrite phase appears unaltered from its nominal appearance. At high magnification, the micro-replication of scratches is observed. Minimal oxidation was observed on the surface and the glass matrix remained fully amorphous, as verified by X-ray diffraction.

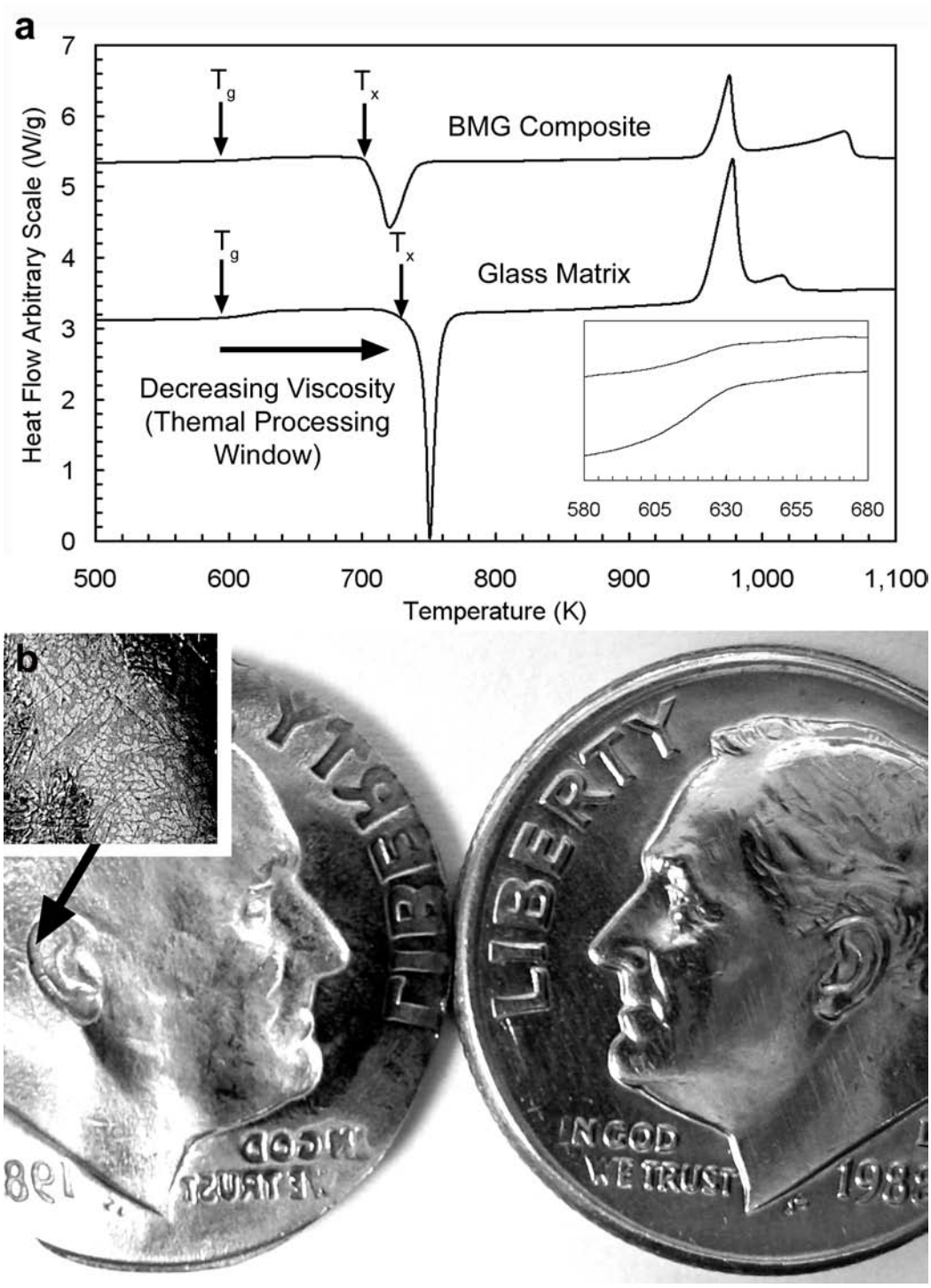

Figure 5.1 – (a) DSC curves of the BMG matrix composite DH1 and its glass matrix. ΔT for both alloys is indicated with arrows, and the glass transitions are shown in the inset. (b) Thermoplastic forming of DH1 into the shape of a U.S. dime. The inset shows the composite microstructure, which is unaltered during the process. Once suitable viscosity is reached in the glass matrix, near-perfect replication was achieved.

5.5 Cold Rolling

In many crystalline metals forming and strengthening is accomplished through cold working. BMGs in contrast, are normally difficult to cold work, owing to their high hardness, low resistance to fracture, and tendency to deform in a highly localized manner. Several attempts have been reported in literature to cold work BMGs to improve mechanical properties. Cold drawing of wire-shaped BMGs and cold rolling of BMG ribbons showed increases in yield strength, while cold rolling of 3-mm-thick BMG plates leads to increased compressive plasticity and Charpy impact toughness [12–16]. For BMG wires and plates with diameters and thicknesses < 1 mm, cold working can be accomplished easily, owing to geometric stability of shear bands in small samples (see, for example Conner, R. D., et al. *Acta Mater.* **52**, 2429 (2004)). In larger specimens (ex. 3 mm plates) thickness reduction can be obtained through cold rolling by covering the samples in MoS_2 grease to avoid cracking and by performing the deformation in small incremental steps of 0.1 to 0.5% per rolling pass. Extensive cold rolling of thin sheets produces many shear bands that are arrested under the geometric confinement, much in the same way apparent “super-plasticity” is achieved in compression tests of BMG rods [17–18]. Closing stresses generated by the compressive load prevent active shear bands from developing into catastrophic cracks and frictional forces arrest persistent slip when shear bands interact with the rolling wheel at the sample’s edge. Cold rolling BMGs was intended here to generate active slip bands, which would release the strain field in front of a crack tip and would ultimately lead to the formation of multiple shear bands during subsequent mechanical testing. Unlike dislocations in crystalline

materials however, shear bands do not have a repulsive core and do not appear to significantly tangle or lock. Without an arresting mechanism, active shear bands slip without limit and generally result in tensile instability. In some cases however, active shear bands oriented at different angles do interact, generating up to 0.25% tensile elongation [13]. Typically, rolled BMGs fail at a lower stress than unrolled samples in uniaxial tension with little or no plastic elongation due to active shear bands generated by cold rolling.

The problems associated with generating active shear bands in rolled BMGs can be circumvented in highly toughened BMG matrix composites. In contrast to the incremental deformation commonly applied to cold rolled monolithic BMGs, Figure 5.2 shows an initially 4-mm-square beam of DH1 that was deformed in steps of 5 to 14% (0.2 to 0.5 mm) per pass through progressively smaller square channels with no oil or lubricant at ambient temperature. In five passes, the initially 4-mm-square beam was reduced to 2.5 mm (square) and the beam length was increased from 51 mm to ~ 124 mm before cracking ensued. Monolithic BMGs rolled at this higher strain typically cracked during the first pass.

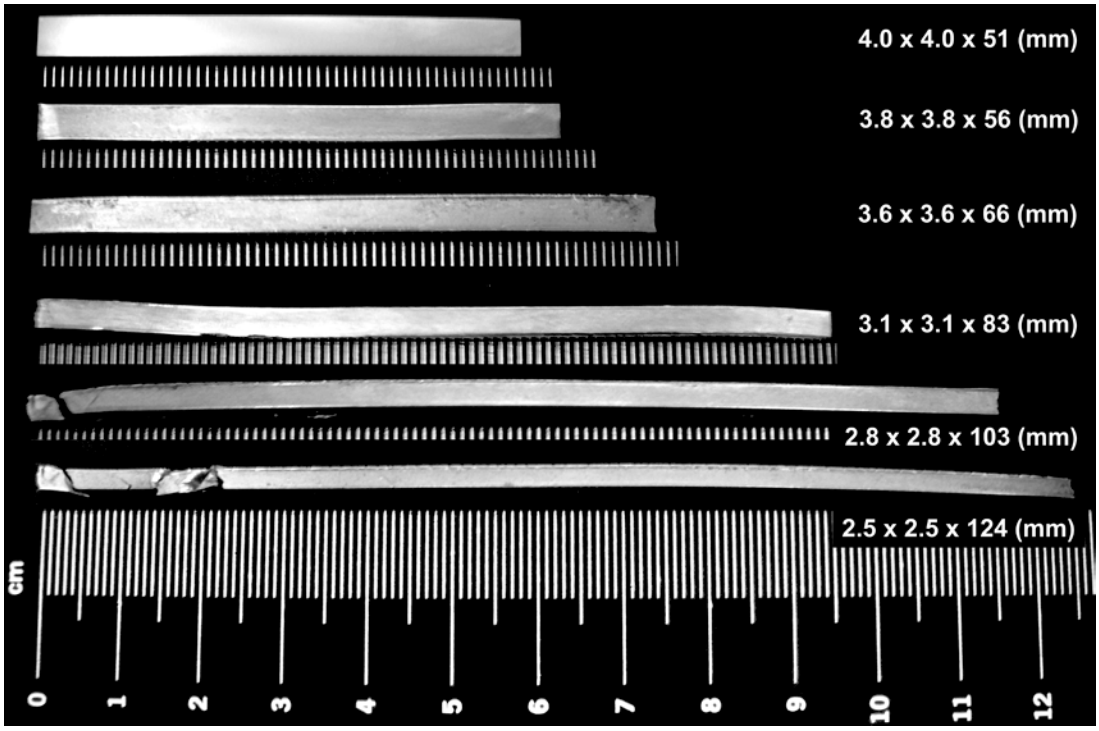

Figure 5.2 – An initially 4-mm-square beam of DH1 cold rolled through square channels five times until cracking ensued. The length of the beam was increased from 51 mm to ~ 124 mm using no lubrication or heating.

5.6 Work Hardening

To investigate the mechanical properties after cold rolling we took a beam of DH1 initially 5 mm square and 51 mm long and cold–rolled it to 4 mm square and 72 mm long (see Figure 5.3(b)). The rolled dendrites are shown in the inset of Figure 3(b). We then machined a cylindrical gauge section 3 mm in diameter and 15 mm long and pulled the sample in uniaxial tension. The tension test is shown in Figure 3(a) along with a nominal sample of DH1 and the BMG Vitreloy 1 for comparison. The unrolled sample of DH1 exhibits total strain to failure of 9.6% and ultimate tensile strength of 1,512 MPa, while the rolled sample exhibits 7.6% and 1,604 MPa, respectively. In addition we observed an increase in Young's modulus for the rolled sample, from 84.3 GPa to 94.5 GPa (measured acoustically). The inset of Figure 5.3(a) shows large shear banding events accompanied by sharp decrease in stress. These jagged drops are seen in tension tests of BMG matrix composites when normally catastrophic shear bands are arrested and stabilized by the microstructure. In the rolled sample, the total plastic strain decreases by ~ 2% from the nominal sample but the reduction in area is substantially less, from 44% in the unrolled sample to 20% in the rolled sample (see Figure 5.3(c-d)). This indicates that the necking instability often seen in high-ductility BMG composites is lessened and the plastic strain is spread more uniformly throughout the gauge section. Moreover, we observe a work-hardening phenomenon which increases the tensile yield strength by ~ 100 MPa. Although the rolled sample contains active shear bands, which have been shown to increase tensile instability, these shear bands are confined to interdendritic regions, effectively locking them and preventing further slip (see

Figure 5.3(f) of [2]). During subsequent tension testing, the stress required to drive these active shear bands through the soft crystalline dendrites is higher than the stress required nucleating new shear bands. A multiplicity of shear bands form and tensile ductility is preserved. The accompanying increase in yield strength is attributed to work-hardening in the dendritic phase through the introduction of dislocations. The arrested shear bands generated during rolling provide nucleation sites for the new shear bands generated during tension testing. In high-ductility BMG matrix composites shear bands normally nucleate and develop within a relatively small region of the gauge section, typically in ~ 2 mm in length out of total length of 15 mm. Necking is usually extensive but confined to this small region. The introduction of shear bands through rolling apparently increases the fraction of the tensile gauge section that participates in plastic deformation, to typically ~ 4 mm. Shear bands on the tensile surface of both the rolled and nominal samples are shown in Figure 5.3(e–f). In both cases there is substantial deformation, evidence of the tensile ductility.

To conclude we note that highly toughened BMG matrix composites are truly a new class of engineering materials. Owing mainly to their high toughness, they can be processed by cold working in a manner similar to crystalline metals without significant cracking or embrittlement. By “designing” the glass matrix phase to have a large ΔT (as in highly processable BMGs), thermoplastic processing (e.g., hot-forging, compression molding, etc.) are possible. Summarizing, the new BMG composites can (1) be processed in the semisolid region (two-phase liquid+dendrite mixtures) by traditional casting into net-shapes, (2) thermo-plastically processed by

reheating above the glass transition temperature of the amorphous matrix, and (3) extensively cold-worked in the solid (glass+dendrite) state. These process characteristics are expected to substantially increase the potential applications for these novel materials.

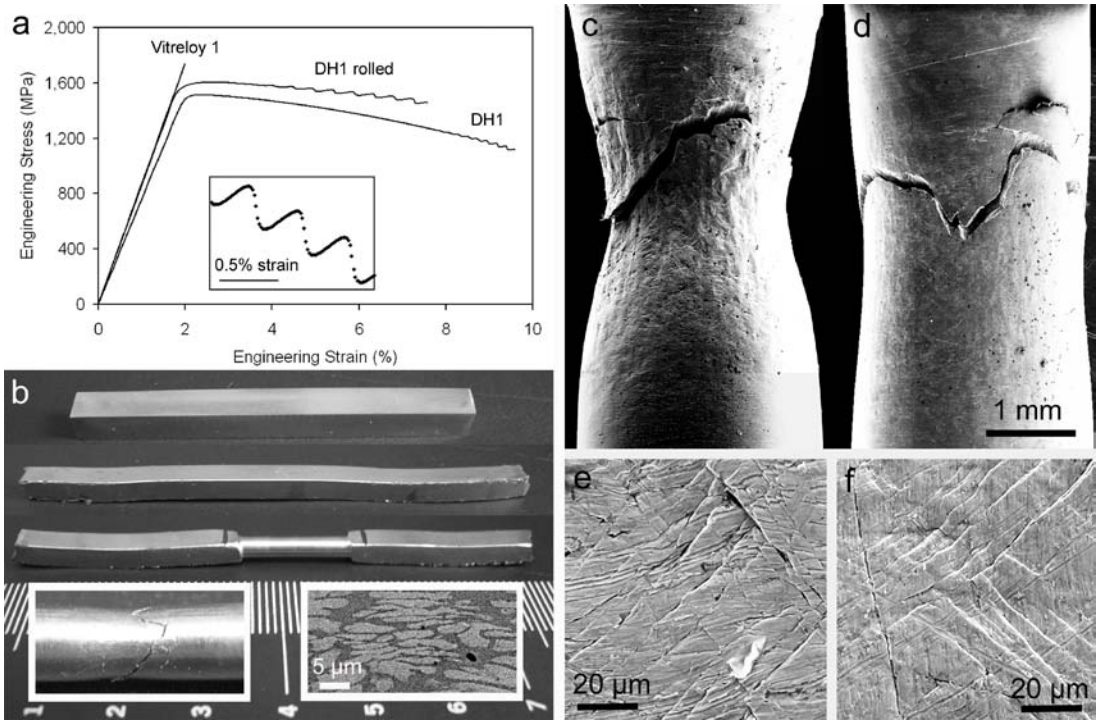

Figure 5.3 – (a) Room-temperature tension testing of a rolled sample of DH1, a nominal sample of DH1, and Vitreloy 1. Stress-strain offsets, shown in the inset, demonstrate stabilization of shear bands in the rolled sample. (b) Images of the unrolled, rolled, and machined samples of DH1 used to generate (a). Broad necking in the 3 mm gauge section after tension testing and the elongated dendrites are shown in the inset. (c) SEM micrograph of the severe necking in unrolled DH1 contrasted with (d) the broad necking in rolled DH1. Shear band formation during tension testing on the surface of (c–d) are shown in (e) for unrolled DH1 and (f) for rolled DH1. In both cases, the extent of deformation is similar.

References

1. Hannink, R. H. J., Kelly, P. M., Muddle, B. C., *J. Am. Ceram. Soc.* **83**, 461(2000).
2. Hofmann, D. C., Suh, J.-Y., Wiest, A., Duan, G., Lind, M.-L., Demetriou, M. D., Johnson, W. L., *Nature* **451**, 2085 (2008).
3. Hays, C. C., Kim, C. P., Johnson, W. L., *Phys. Rev. Lett.* **84**, 2901 (2000).
4. Szuecs, F., Kim, C. P., Johnson, W. L., *Acta Mater.* **49**, 1507 (2001).
5. Duan, G., Wiest, A., Lind M.-L., Li, J., Rhim, W.-K., Johnson, W. L., *Adv. Mater.* **19**, 4272 (2007).
6. Schroers, J., *JOM* **57**, 35 (2005).
7. Schroers, J., Paton, N., *Adv. Mater. Proc.* **164**, 61 (2006).
8. Schroers, J., Johnson, W. L., *Appl. Phys. Lett.* **84**, 3666 (2004).
9. Fan, G. J., Fecht, H. J., Lavernia, E. J., *Appl. Phys. Lett.* **84**, 487 (2004).
10. Chu, J. P., Wijaya, H., Wu, C. W., Tsai, T. R., Wei, C. S., Wadsworth, J., *Appl. Phys. Lett.* **90**, 34101 (2007).
11. Lee, M. H., Park, J. S., Kim, J.-H., Bae, D. H., Kim, W. T., Kim, D.H., *Mater. Lett.* **58**, 3312 (2004).
12. Yokoyama, Y., Inoue, K., Fakaura, K., *Mater. Trans.* **43**, 3199 (2002).
13. Yokoyama, Y., *J. Non-Cryst. Solids* **316**, 104 (2003).
14. Park, J. S., Lim, H. K., Kim, J.-H., Chang, H. J., Kim, W. T., Kim, D. H., Fleury, E., *J. Non-Cryst. Solids* **351**, 2141 (2005).
15. Park, J. S., Lim, H. K., Kim, J.-H., Park, J. M., Kim, W. T., Kim, D. H., *J. Mater. Sci.* **40**, 1937 (2005).

16. Conner, R. D., et al., *Acta mater.* **52**, 2429 (2004).

17. Liu, Y. H., Wang, G., Wang, R. J., Zhao, D. Q., Pan, M. X., Wang, W. H., *Science* **315**, 1385 (2007).

18. Yao, K. F., Ruan, F., Yang, Y.Q., Chen, N., *App. Phy. Lett.* **88**, 122106 (2006).

Chapter 6

New Titanium-Based Glass-Dendrite Composites with Tensile Ductility

6.1 Commentary

This chapter describes new titanium-based BMG composites, with the same density as structural crystalline titanium alloys, that are also low cost and contain a reduced beryllium concentration. Unlike Chapter 4 where we tuned the composites for maximum fracture toughness and tensile ductility, in this work we develop composites with low density as the major design objective. Each alloy is designed to have the lowest possible density while still retaining at least 5% tensile ductility. This chapter represents the first demonstration of the following: (1) titanium-based BMG composites with tensile ductility, (2) BMG composites with density less than 5.0 g/cm^3 with tensile ductility, (3) alloys with less than 1.0 weight % beryllium with tensile ductility. Owing to their low density and cost this new class of alloys will likely be far more successful as commercial engineering materials than the alloys we presented in Chapter 4.

6.2 Background on Nanostructure-Dendrite Composites

Recently, titanium-based nanostructure-dendrite composites have been reported which are said to exhibit increased toughness over bulk metallic glasses (BMGs) and other nanostructured materials (see [1]). This work has spawned an

entirely new field of nanoeutectic-oriented metallurgy, with dozens of publications touting the benefits of such materials over BMGs (see, for instance, [2–14]). However, upon further investigation of this new field, we note that uniaxial compression tests are typically the only mechanical tests used to characterize the perceived toughness and enhanced plasticity of the nanostructured composites. The geometry of the compression test, where closing stresses and friction arrest slip, has resulted in the overstatement of toughness in these new materials. It appears that the nanostructure-dendrite composites are very similar to BMG composites, but with a eutectic matrix that failed to form a glass during rapid cooling. The crystallized matrix, or nanostructured eutectic as it is often called, is typically comprised of brittle intermetallics, and fails with no apparent plasticity in bending or tension tests. When nanostructure-dendrite composites are loaded in an unconfined manner, as with the uniaxial tension test, cracks move unimpeded through the brittle matrix and global ductility is absent. In contrast, if the matrix is frozen as a glass, the length scale of the deformation is larger, allowing microstructural stabilization mechanisms to become possible. In the current work, we demonstrate several new titanium-based glass-dendrite composites, all of which exhibit at least 5 percent tensile ductility, low cost, and densities comparable to high-performance crystalline titanium alloys (4.97–5.15 g/cm^3). We observe a remarkable similarity in mechanical properties (such as tensile ductility, yield strength, and fracture toughness) between the new glassy-composites and high-strength crystalline titanium alloys (such as Ti-6Al-4V) — all with a significantly lower Young's modulus. The current work demonstrates

that titanium-based BMG composites can be competitive with crystalline titanium alloys for structural applications where high strength and toughness are a necessity.

6.3 Designing Two-Phase Composites

Two-phase composites based in titanium and zirconium are relatively easy to produce, owing to the extremely low solubility of many metals and metalloids with body centered cubic (b.c.c.) titanium/zirconium. For example, copper, nickel, and beryllium all exhibit low solubility in b.c.c. titanium, and additions of these elements typically cause b.c.c. titanium-based dendrites to form in a continuous crystalline matrix. In cases where the matrix is designed around a glass-forming composition, a two-phase glass-dendrite composite can be formed. Recently, it has been shown that with proper control over the shear modulus (G) of the dendritic phase and the size of the dendrites, extensive toughening and ductility can be achieved [14]. Deformation in the glass matrix, manifested by narrow shear bands, can be confined to interdendric regions, resulting in the formation of a multiplicity of shear bands and global ductility [14]. In the case where the glass matrix does not vitrify into a bulk glass, a brittle nanostructure-dendrite composite forms, accompanied by a large increase in G. Based on nearly two decades of research with BMGs, we note that a crystallized or partially crystallized metallic glass is *always* more brittle than a fully amorphous one. This can typically be attributed to hard intermetallic phases that often appear near glass-forming regions, which rapidly increase G. Plasticity is always enhanced in glass-forming alloys when G is minimized, and partial crystallization always results in an increase in G. Under compressive loads, however, plasticity can appear similar for both composites. In the nanostructure-dendrite alloy

$Ti_{60}Cu_{14}Ni_{12}Sn_4Nb_{10}$, 14.5% compressive plasticity is observed [1] while in the glass-dendrite alloy $Zr_{56.2}Ti_{13.8}Nb_{5.0}Cu_{6.9}Ni_{5.6}Be_{12.5}$, 8% compressive plasticity is observed [15–16]. However, their behavior in tensile loading is far different. While the glass-dendrite composites have been shown to exhibit up to ~ 13% tensile ductility [14], nanostructure-dendrite composites fail in an apparently brittle manner with no global ductility. Shear bands that form in the nanostructured eutectic matrix develop into catastrophic cracks at much shorter lengths than in BMGs, leading to failure on a continuous path through the matrix. The crystalline phases act as nucleation sites for shear bands, which typically form at lower stresses than in monolithic glasses. Despite claims of increased toughness and ductility in several publications on nanostructure-dendrite composites, tension tests are noticeably absent [1–14].

Developing titanium-based ductile-phase BMG composites is challenging, owing to several design criterion which must be satisfied to achieve tensile ductility. The necessary steps are (1) finding a highly processable titanium-based BMG, (2) creating a two-phase microstructure of glass plus b.c.c. dendrites, (3) lowering the shear modulus of the dendritic phase relative to the glass matrix, and (4) coarsening and homogenizing the microstructure. Additionally, to make the alloys commercially competitive with crystalline titanium alloys, density and cost must be minimized. We note that among these four essential design criteria to obtain tensile ductility, nanostructure-dendrite composites possess only one: low dendrite shear modulus. This can be attributed to the addition of b.c.c. stabilizing elements such as tantalum, niobium, and tin (which simultaneously increases their density).

Currently, the only ductile-phase BMG composites available are based in the relatively dense and expensive element zirconium [14–16]. The first in-situ BMG composite, $Zr_{56.2}Ti_{13.8}Nb_{5.0}Cu_{6.9}Ni_{5.6}Be_{12.5}$ (in atom %), exhibits density of 6.4 g/cm^3 and is comprised of greater than 70 weight % zirconium [15–16]. Recently, improved alloys, such as $Zr_{36.6}Ti_{31.4}Nb_7Cu_{5.9}Be_{19.1}$, were demonstrated to have densities of 5.6–5.8 g/cm^3 by increasing the amount of titanium and removing nickel [14]. However, these alloys too are comprised of greater than 50 weight % zirconium. To design new titanium-based composites, we first notice that new low-density titanium-based BMGs have recently been discovered exhibiting densities that range among common engineering titanium alloys (4.59–4.91 g/cm^3), but with more than double the specific strength [17]. These new BMGs, based in the ternary Ti-Zr-Be glass-forming system, represent great improvements over zirconium-based BMGs in terms of cost and density, yet they posses several drawbacks relative to conventional crystalline titanium alloys. Although the alloys can be produced in thicknesses well above the “bulk” range (typically < 1 mm), they are not considered “highly-processable” that is, they do not have glass-forming ability greater than 1 cm and cannot be produced amorphously in ingot form. Two titanium-based BMGs exhibit a similar critical dimension of 6 mm [17], $Ti_{45}Zr_{20}Be_{35}$ and $Ti_{40}Zr_{25}Be_{35}$. In addition, as with all monolithic BMGs, these alloys exhibit no tensile ductility in bulk samples and limited bending ductility in beams less than 1 mm thick.

6.4 New Ti-Based Bulk Metallic Glass Composites

To design a composite structure around the ternary Ti-Zr-Be system, we first increase the atom % of titanium plus zirconium proportionally to 70%. At and above

this concentration, the liquid undergoes phase separation during rapid cooling, with dendrites nucleating and growing below the liquidus temperature. As the dendrites grow, they deplete the remaining liquid of titanium and zirconium until an equilibrium concentration is reached, typically near a eutectic (which corresponds well with glass-forming compositions), causing the liquid to vitrify upon subsequent undercooling. The volume (or molar) fraction of dendrites embedded in the glass matrix is directly related to the low solubility of beryllium and copper in b.c.c. (or β) titanium and zirconium. The alloy $Ti_{40}Zr_{30}Be_{30}$, for example, forms a two-phase microstructure of glass plus b.c.c. dendrites upon rapid cooling and has glass-forming ability up to 7 mm. Despite the appropriate microstructure for tensile ductility, this alloy exhibits the same catastrophic failure associated with single-phase BMGs. This is expected, based on our previous discussion that significant tensile ductility can only be achieved in BMG matrix composites when the shear modulus (G) of the inclusion is lower than G of the glass, such that deformation is promoted in the dendritic phase and shear band lengthening is suppressed in the glass phase [14]. In $Ti_{40}Zr_{30}Be_{30}$, the dendrite is a b.c.c. Ti-Zr phase (G > 40 GPa), while the glass is a Ti-Zr-Be phase (G ~ 35 GPa). To increase the tensile ductility and resistance to crack propagation, β-stabilizers must be used to reduce G in the dendritic phase. These stabilizers exhibit an electronic softening phenomenon that dramatically lowers G, typically as low as 20–30 GPa.

Before we can reduce G in the dendritic phase we must first improve the glass-forming ability of the ternary system so that it can be produced in ingot form. Our processing strategy to coarsen and homogenize the microstructure, called semi-

solid processing, typically requires critical dimensions of at least 1 cm. It is well known from our work with Vitreloy-type BMGs ($Zr_{41.2}Ti_{13.8}Cu_{12.5}Ni_{10}Be_{22.5}$, Vitreloy 1) that the additions of late transition metals such as copper, nickel, iron, and cobalt increases the glass-forming ability from several millimeters to several centimeters [18]. We notice that copper and nickel phase-separate preferentially into the glass matrix, forming typically less than 1 atom % in the dendrite. This is important because some metals and metalloids (like aluminum, for example) will divide between the two phases and increase G in the dendrite. For this work, we select copper as the late transition metal both for its strong affinity towards the glass matrix and because copper has been shown to enhance the fracture toughness of monolithic BMGs. The alloys reported herein contain only 3–5 atom % copper, and yet glass-forming ability for each alloy is greater than 2 cm when cooled from one side in ingot form, demonstrating the profound effect of adding a late transition metal.

In contrast to the addition of late transition metals, we notice that the β-stabilizers (that have complete solubility with b.c.c. titanium and zirconium) separate preferentially into the dendrite, forming typically less than 5 atom % in the glass matrix. Their addition can reduce G in the dendrite phase without compromising glass forming or the fracture toughness of the BMG phase. We have previously succeeded in creating ductile phase composites with the addition of the β-stabilizers niobium, tantalum, and molybdenum, but these elements are extremely dense, which raises the overall density of the composites substantially. In this work, we investigate the addition of the low-density β-stabilizer vanadium. We start by designing a

composite with roughly 50% glass phase by volume, which can be achieved when the atomic percent of beryllium and copper sum to ~ 20% and the titanium and zirconium are equal. We systematically add vanadium until G of the dendrite drops below G of the glass and toughening is observed. We then reduce the amount of zirconium, which reduces the fracture toughness of the glass phase, until some compromise between mechanical properties and density is reached. The first alloy we present is $Ti_{48}Zr_{20}V_{12}Cu_5Be_{15}$ (DV1 in atom %), with ρ = 5.15 g/cm^3, produced by the semi-solid processing method. DV1 separates into 53% glass with composition $Ti_{32}Zr_{25}V_5Cu_{10}Be_{28}$ and 47% b.c.c. with composition $Ti_{66}V_{19}Zr_{14}Cu_1$, as determined through energy dispersive X-ray spectrometry (EDS). These values have an estimated error of 5%. DV1 is our most highly optimized alloy and exhibits 12.5% total strain to failure at 1.4 GPa of maximum stress in room temperature tension testing, see Figure 6.1(a). Despite having low density and a large volume fraction of glass, DV1 exhibits extensive shear band stabilization, evidenced by the jagged nature of the tension test just prior to failure. Each drop in stress is associated with a normally catastrophic shear band being arrested by the microstructure, leading to significant necking (43% reduction in area, shown in the inset of Figure 6.1(a)). The necking instability is associated with dense patterns of primary, secondary, and tertiary shear bands that are visible on the surface (Figure 6.1(c)).

We use the optimized structure of DV1 to design three more alloys that sample the new Ti-Zr-V-Cu-Be system. First, we investigate the effect of increasing the volume fraction of glass to create a high-strength composite. By directly replacing titanium with beryllium we can increase the volume fraction of glass to

70%, retain 9.5% total strain to failure, but increase the ultimate tensile strength to 1.6 GPa. This alloy, $Ti_{44}Zr_{20}V_{12}Cu_5Be_{19}$ (DV2), is the highest strength (combined with the largest fraction of glass) alloy we have yet observed that still exhibits greater than 5% tensile ductility. The high strength, combined with low density (5.13 g/cm^3), puts the specific strength of DV2 (defined here as maximum stress divided by density) at 314 MPa cm^3/g, which, for the first time, approaches the specific strength of Vitreloy-type monolithic BMGs [18].

In an attempt to minimize density, we also report two alloys with increased volume fraction of b.c.c. phase, $Ti_{56}Zr_{18}V_{10}Cu_4Be_{12}$ and $Ti_{62}Zr_{15}V_{10}Cu_4Be_9$ (DV3 and DV4, respectively). DV3 and DV4 exhibit densities of 5.08 and 5.03 g/cm^3 with 46% glass and 40% glass, respectively. It is noteworthy to mention the similarity in the amounts of titanium with previously reported nanostructured composites [1]. SEM micrographs of the necking in DV1–4 can be seen in Figure 6.1(d), with the typical microstructures shown in Figure 6.1(e). While unexplained, the microstructure of DV4 is substantially larger than the other similar alloys. This results in a lower yield strength but increased ductility. The microstructure of DV4 represents evidence that by taking two similar BMG composites and increasing the scale of the dendrites, tensile ductility can be enhanced.

We note that there appears to be a limit of 5.0 g/cm^3 in the minimization of density using the Ti-Zr-V-Cu-Be system. We could not find a configuration of the elements that would allow us to pierce this density barrier while still obtaining extensive tensile ductility. By observing the success of non-beryllium containing BMGs, such as $Zr_{57}Nb_5Cu_{15.4}Ni_{12.6}Al_{10}$ (Vitreloy 106) [19], and high-strength

crystalline titanium alloys containing vanadium, such as Ti-6Al-4V (in weight %), we note that aluminum is a beneficial addition to both systems. Therefore, we attempt to add aluminum to our BMG composites to lower density. It should be noted that previous Zr-Ti-Nb-Cu-(Ni)-Be composites cannot be alloyed with aluminum, owing to undesirable phases that form between aluminum and niobium. Our new alloy system lacks niobium, so we were able to systematically add aluminum to explore the effects on glass forming and tensile ductility. With the addition of up to 10 atom % aluminum, glass forming was not affected. Unfortunately, aluminum is a powerful α-stabilizer for titanium and even small additions dramatically increase *G*. If the aluminum content exceeds ~ 3 atom %, tensile ductility rapidly falls to zero. We further report two aluminum containing alloys $Ti_{60}Zr_{16}V_9Cu_3Al_3Be_9$ and $Ti_{67}Zr_{11}V_{10}Cu_5Al_2Be_5$ (DVAl1 and DVAl2, respectively). Aluminum typically exhibits some solubility in b.c.c. titanium, so it partions equally between both phases. Therefore, small additions of aluminum can be used to supplement copper for improving glass-forming ability, resulting in alloys with density less than 5 g/cm^3 (4.97 g/cm^3 for both DVAl1 and DVAl2). Minimizing density requires reductions in the amount of zirconium, which leads to alloys with lower volume fractions of glass to retain tensile ductility (31% and 20% in DVAl1, and DVAl2, respectively). It is noteworthy to mention that DVAl2 contains 62% titanium by weight and only 0.9% beryllium by weight. Figure 6.2(d) demonstrates that large samples can be created from DVAl2 and significant bending ductility is observed in up to ~ 4 mm thick beams, despite being nearly beryllium free.

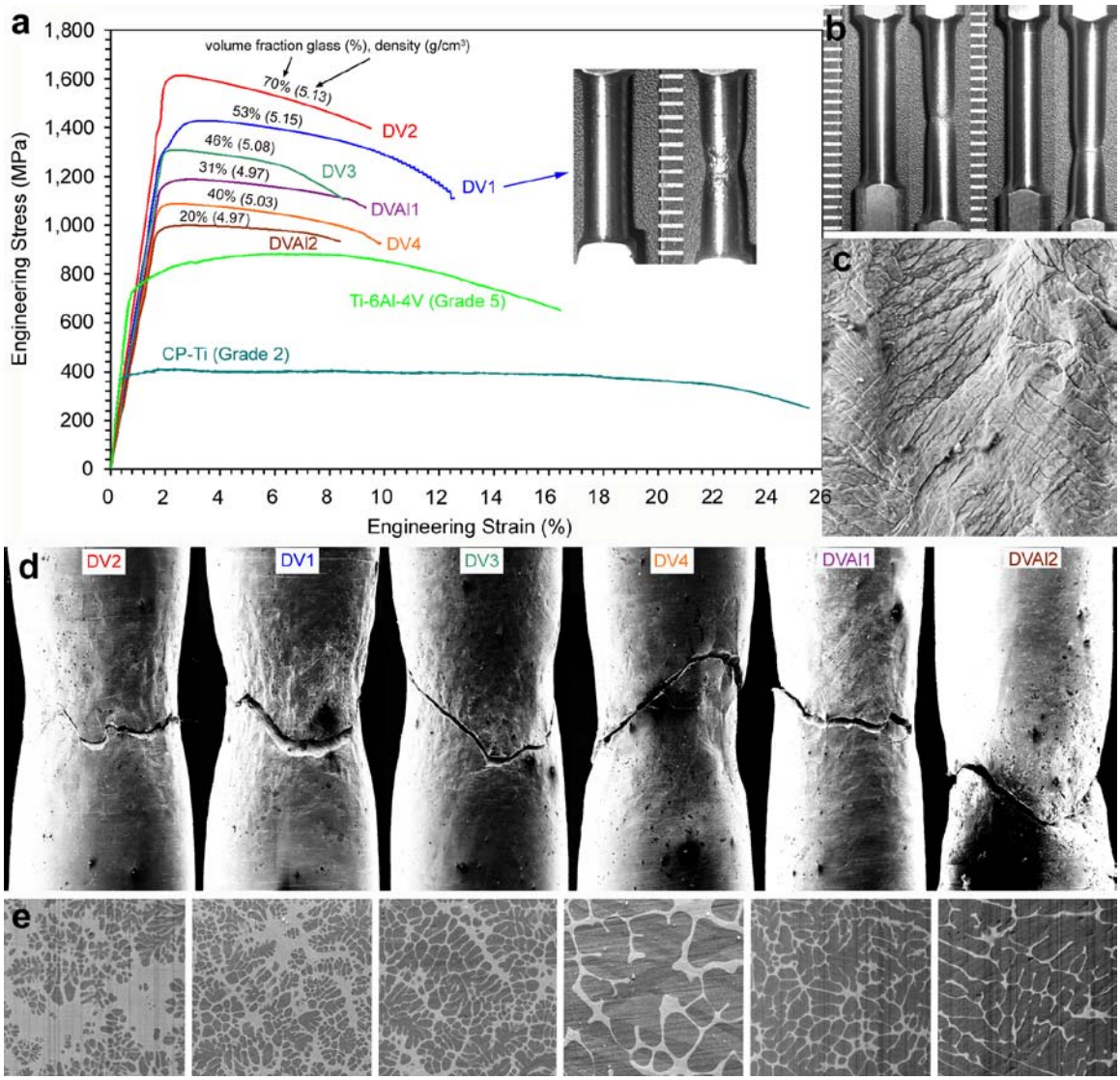

Figure 6.1 – Tensile ductility in titanium-based metallic glass composites. (a) Room-temperature tension tests for the six BMG composites developed in this work compared with commercial pure titanium and Ti-6Al-4V. A maximum stress of 1.6 GPa is obtained and each alloy exhibits > 5% tensile ductility. An example of necking in the alloy DV1 is shown in the inset. (b) Optical images of necking in commercial pure titanium (left) and Ti-6Al-4V (right). (c) Dense shear band pattern on the tensile surface of DV1. (d) SEM micrographs showing necking in the six BMG composites along with their respective microstructure shown in (e).

As a direct comparison between the new BMG composites and their nearest competitors, crystalline titanium alloys, we have included tension tests in Figure 1(a) for commercial pure titanium (CP-Ti or Grade 2) and Ti-6Al-4V (Ti-6-4 or Grade 5 annealed). As expected, CP-Ti exhibits low ultimate strength (~ 400 MPa) but extensive elongation (~ 25%). Ti-6-4 in the annealed condition, on the contrary, has ultimate strength of ~ 850 MPa combined with ~ 16% total strain. Ti-6-4 was selected both because of its low density (4.43 g/cm^3) but also because it accounts for the majority of commercial titanium applications. Both tests were done in the same 3 mm diameter as the BMG composites with the same sample geometry, shown in Figure 6.1(b). By enlarging the tension tests on the titanium alloys from Figure 6.1(b), it is clear that both alloys exhibit global deformation resulting from motion of dislocations throughout the entire gauge length, and that the reduction in area at the neck is less than 30%. In contrast, BMG composites exhibit almost no global deformation but have large reductions in area at the point of fracture. Although not shown, we notice that the tensile ductility and yield strength of the titanium-based BMG composites is nearly identical to some common high-strength crystalline titanium alloys. Ti-6-4 in the standard condition (as opposed to the annealed condition), for example, has an ultimate strength of ~ 1.1 GPa and ~ 10% elongation, leading to a specific strength of 264 MPa cm^3/g — higher than four of the BMG composites, but lower than DV1 and DV2. The tension tests are remarkably similar, considering the glassy composites have significantly lower Young's modulus (78–94 GPa versus ~ 115 GPa), larger elastic limit (~ 2% versus ~ 1%), and exhibit

deformation through millions of tiny stabilized cracks, instead of through dislocation-based plasticity.

Despite their similar mechanical properties, the solidus temperature of the BMG composites differs dramatically from crystalline titanium alloys. Owing to the presence of a glass matrix, which is typically designed around a deep eutectic, the BMG composites exhibit a solidus temperature that is ~ 900 K lower than their crystalline counterparts (and ~ 200 K lower than nanostructured composites). In the BMG composites, the solidus temperature occurs at the onset of melting of the glass-forming phase. Just above solidus, the dendrites simply float in a glass-forming liquid, creating a semi-solid solution, and net-shape casting (into copper molds for instance) is easily attainable. On the contrary, titanium alloys must typically be machined into net-shaped parts, adding enough post-production cost in some cases that it negates the cost of the starting materials. The low processing temperatures of the composites allow for rapid prototyping of parts and a cost savings over crystalline titanium alloys.

As a further comparison between the new BMG composites and crystalline titanium alloys, plane-strain fracture toughness measurements were performed on three of the best alloys — DV1, DV3, and DV4. Figure 6.2(a) demonstrates the semi-solid processing method used to homogenize and coarsen the dendrites, which vastly improves fracture toughness. In our previous publication [14], we related maximum bending thickness of BMGs with fracture toughness, K_{1C}. As a way of verifying our K_{1C} measurements we clamp large ingots of the composites in a vise, and bend them with repeated hammer strikes. The maximum thickness in which

significant bending is observed is related to K_{1C} through the size of the plastic zone at the tip of a crack. From Figure 6.2(c) we see that DV4 (front of Figure 6.2(c)) can be bent to more than 90° at 3 mm, while at 4 mm significant cracking is observed. DV3 (middle of Figure 6.2(c)) fractures closer to 30° at 3 mm. K_{1C} measurements were performed in 3-mm-thick plates, in conformance to the relaxed thickness requirements of the ASTM standards. K_{1C} values of 43.8, 47.4, and 61.6 MPa $m^{1/2}$ were recorded for DV1, DV3, and DV4, respectively. It is noteworthy to mention that the high-strength crystalline alloy Ti-6-4 in the standard condition exhibits K_{1C} = 43.0 MPa $m^{1/2}$ — again, very similar to what is observed in the BMG composites. As a method of comparing bending ductility between the new BMG composites and previously reported nanostructure-dendrite composites, we show a 3-mm-diameter rod of the alloy $Ti_{60}Cu_{14}Ni_{12}Sn_4Nb_{10}$, prepared using ultra-pure starting materials with oxygen content less than 25 ppm, in the same geometry and with the same processing technique as in [1]. This alloy was demonstrated to have 14.5% plastic strain in compression [1], and yet we note that the alloy is brittle when bent with no plasticity (Figure 6.2(b)). This supports our earlier claim that brittle phases form when a BMG is insufficiently cooled, creating a material with no apparent toughness.

The last part of this work focuses on the necessity of beryllium in the composites. After investigating hundreds of alloys, we have not found a highly processable BMG composite that is beryllium free. Two-phase crystalline composites without beryllium can be easily obtained in our BMG composites by replacing beryllium with copper, but we notice these alloys are extremely brittle.

Figure 6.3(a) is a differential scanning calorimetry (DSC) scan comparing DV2 with a titanium-based non-beryllium composite (a nanostructure-dendrite composite), $Ti_{52}Zr_{18}V_{12}Cu_{15}Al_3$. Despite having little or no glass, the beryllium-free alloy exhibits a sharp increase in solidus temperature (from 950 K to 1160 K), indicating the eutectic phase is no longer a bulk glass former. Although not shown, we notice that the non-beryllium composite yields under compressive loads but is still very brittle, as with all other nanostructure-dendrite composites.

Highly processable zirconium- and titanium-based BMGs have been developed using two primary strategies: deep eutectics and atomic size mismatch. The best glass formers are based in the Zr-Be system (2.5 cm maximum) and the Pd-P system (7 cm maximum thickness), and they attribute their glass forming to both the deep eutectics and the presence of small atoms such as phosphorus and beryllium. The deep eutectics allow for rapid undercooling, while the atomic size mismatch frustrates crystallization. The most highly processable non-beryllium zirconium-based BMGs, Vitreloy 106 and 105 ($Zr_{52.5}Ti_5Cu_{17.9}Ni_{14.6}Al_{10}$), both exhibit up to 1.5 cm glass-forming ability and use only the second strategy. Aluminum is a small metalloid, which improves glass forming, but typically raises melting temperature. Vitreloy 105 and 106 have solidus temperatures at ~ 1100 K, versus ~ 900 K in beryllium-containing alloys, which accounts for the reduction in glass forming. Many attempts have been made to create ductile phase composites based on Vitreloy 105 and 106, but we feel such strategies are not possible, based on our previous discussion. Both alloys contain 10 atom % aluminum, which is partially soluble in b.c.c. zirconium. Despite the fact that in-situ formed composites based on

these alloys are extremely prone to crystallization, any dendritic phase will contain a substantial amount of aluminum, which will raise *G*. To illustrate this, we report that a highly processable BMG composite exists in $Ti_{62}Zr_{20}Be_9Fe_6Al_4$, with microstructure similar to the other alloys reported here. An X-ray diffraction pattern exhibiting b.c.c. peaks superimposed on a glassy background is shown in Figure 6.3(b), along with an SEM micrograph of the microstructure shown in the inset. Although glass forming is quite high, this alloy exhibits no tensile ductility and is very brittle in bending, also shown in the inset of Figure 6.3(b). The presence of aluminum stiffens the dendritic phase (i.e., raises *G*) and ductility is compromised. The dendritic phase for this alloy was determined to be $Ti_{72.3}Zr_{19.3}Fe_{3.4}Al_5$, which has $G \sim 45$ GPa, while in contrast the glass matrix has $G < 40$ GPa. This alloy demonstrates that even when the matrix is frozen into an amorphous state, toughening does not necessarily occur. Currently, we do not know of any highly processable zirconium- or titanium-based BMGs without the presence of beryllium or aluminum.

The compositions (both in weight % and atom %) and the mechanical properties gathered on the new composites are listed in Table 6.1.

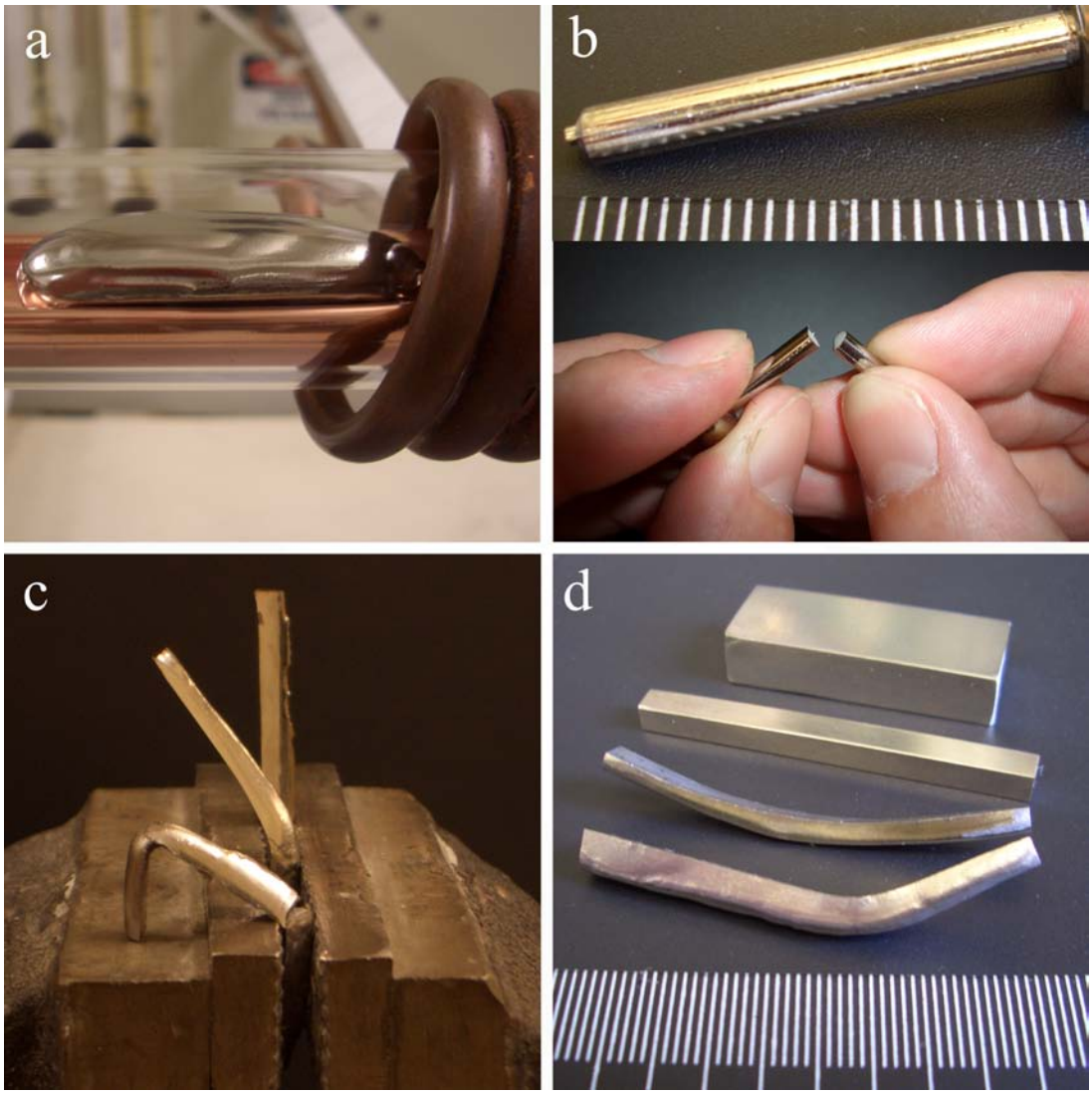

Figure 6.2 – Bending ductility in new titanium-based BMG composites. (a) 25 gram ingot of DV1 undergoing semi-solid processing in a water-cooled copper boat. (b) A 3-mm-diameter rod of a nanostructure-dendrite composite $Ti_{60}Cu_{14}Ni_{12}Sn_4Nb_{10}$ (from [1]) demonstrating that it fractures with no plasticity in bending despite having extensive compressive plasticity. (c) Beams of DH4 (front) and DH3 (middle) bent in a vise, illustrating bending ductility. (d) Several samples of the alloy DVAl2 demonstrating large glass-forming ability and bending ductility. This alloy contains only 0.9 weight % beryllium (5 atom %).

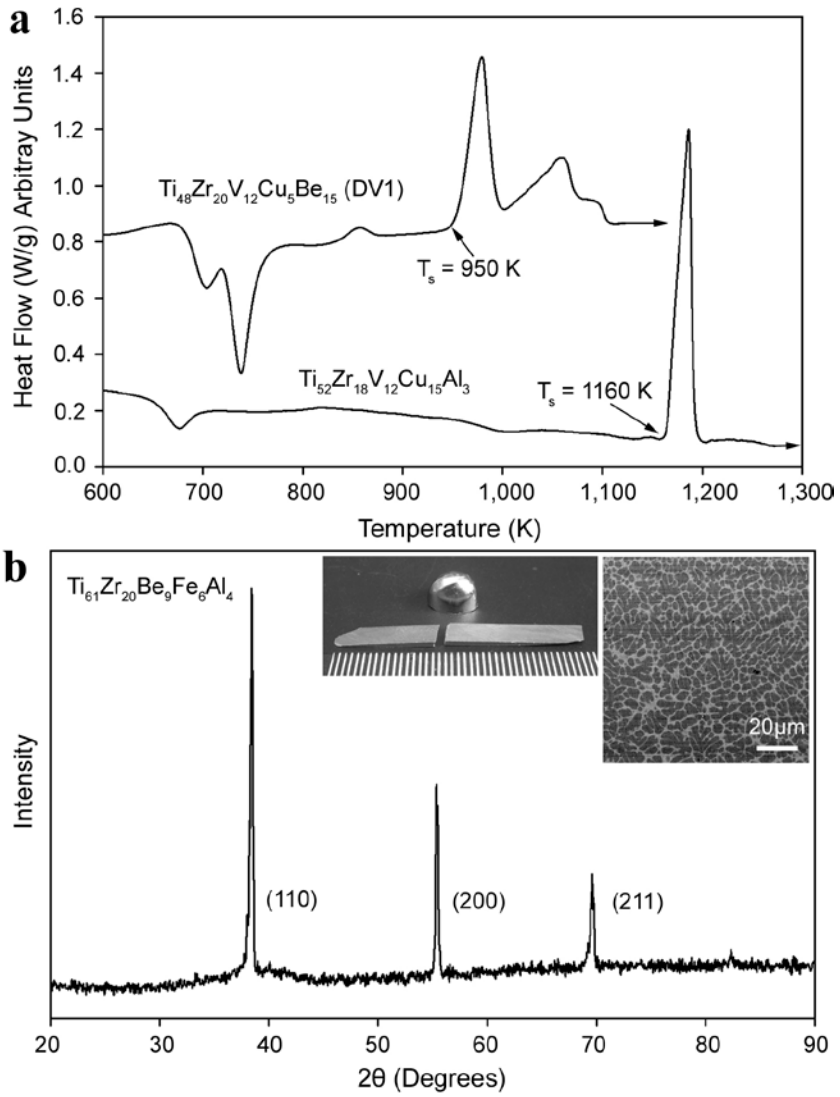

Figure 6.3 – Importance of microstructure on tensile ductility. (a) DSC scans of the BMG composite DV1 compared to an alloy where the beryllium is removed, $Ti_{52}Zr_{18}V_{12}Cu_{15}Al_3$. Solidus temperature increases by more than 200 K when the beryllium is removed, indicating why glass forming is absent. (b) X-ray diffraction pattern of a BMG composite, $Ti_{61}Zr_{20}Be_9Fe_6A_{l4}$, showing a b.c.c. pattern on a glassy background (SEM image of microstructure shown in the inset). Despite the proper microstructure for ductility, the alloy is brittle (shown in the inset), demonstrating the profound effect of the dendrite shear modulus on ductility.

Table 6.1 – Mechanical properties of new titanium-based metallic glass composites. BMG composites are shown with crystalline titanium counterparts in both weight percent and atom percent. Reported values are density (ρ), yield stress (σ_y), ultimate tensile stress (σ_{max}), yield strain (ε_y), total strain (ε_{tot}), specific strength (σ_{max}/ρ), reduction of area (RoA), Young's modulus (*E*), shear modulus (*G*), Poisson's ratio (υ), and solidus temperature (K).

			BMG	bcc	ρ	σ_y	σ_{max}	ε_y	ε_{tot}	σ_{max}/ρ	RoA	K_{1C}	*E*	*G*	υ	T_s
name	**atomic %**	**weight %**	**(%)**	**(%)**	**(g/cm^3)**	**(MPa)**	**(MPa)**	**(%)**	**(%)**	**(MPa cm^3/g)**	**(%)**	**(MPa m$^{1/2}$)**	**(GPa)**	**(GPa)**		**(K)**
DV2	$Ti_{44}Zr_{20}V_{12}Cu_5Be_{19}$	$Ti_{41.9}Zr_{36.3}V_{12.1}Cu_{6.3}Be_{3.4}$	70	30	5.13	1597	1614	2.1	9.5	315	34	na	94.5	34.8	0.358	956
DV1	$Ti_{48}Zr_{20}V_{12}Cu_5Be_{15}$	$Ti_{44.3}Zr_{35.2}V_{11.8}Cu_{6.1}Be_{2.6}$	53	47	5.15	1362	1429	2.3	12.5	277	43	43.8	94.2	34.4	0.368	955
DV3	$Ti_{56}Zr_{18}V_{10}Cu_4Be_{12}$	$Ti_{51.6}Zr_{31.6}V_{9.8}Cu_{4.9}Be_{2.1}$	46	54	5.08	1308	1309	2.2	8.6	258	31	47.4	84.0	30.5	0.379	951
DV4	$Ti_{62}Zr_{15}V_{10}Cu_4Be_9$	$Ti_{57.3}Zr_{26.4}V_{9.8}Cu_{4.9}Be_{1.6}$	40	60	5.03	1086	1089	2.1	9.8	217	42	61.6	83.7	30.4	0.377	940
DVAl1	$Ti_{60}Zr_{16}V_9Cu_3Al_3Be_9$	$Ti_{55.8}Zr_{28.4}V_{8.9}Cu_{3.7}Al_{1.6}Be_{1.6}$	31	69	4.97	1166	1189	2.0	9.3	239	27	na	84.2	31.0	0.360	901
DVAl2	$Ti_{67}Zr_{11}V_{10}Cu_5Al_2Be_5$	$Ti_{62.4}Zr_{19.5}V_{9.9}Cu_{6.2}Al_1Be_{0.9}$	20	80	4.97	990	1000	2.0	8.4	201	28	na	78.7	28.6	0.376	998
Ti-6-4a	$Ti_{86.1}Al_{10.3}V_{3.6}$	$Ti_{90}Al_6V_4$ (Grade 5 Annealed)	na	na	4.43	754	882	1.0	16.4	199	42	100.0	113.8	44.0	0.342	1877
Ti-6-4s	$Ti_{86.1}Al_{10.3}V_{3.6}$ [Ref]	$Ti_{90}Al_6V_4$ (Grade 5 STA)	na	na	4.43	1100	1170	~1	~10	264	na	43.0	114.0	44.0	0.330	1877
CP-Ti	Ti_{100}	Ti_{100} (Grade 2)	na	na	4.51	380	409	0.7	25.5	91	46	66.0	105.0	45.0	0.370	~1930

6.5 Conclusion

We conclude by noting that the new titanium-based BMG composites presented here greatly extend the potential uses for metallic glasses by reducing their cost and density while still retaining characteristics of predictable and non-catastrophic failure. The new composites contain all the benefits of the best monolithic metallic glasses (high strength, high elastic limit, low processing temperatures) but simultaneously exhibit similar mechanical properties to the most common high-strength crystalline titanium alloys. This work demonstrates that tensile ductility, as opposed to compressive plasticity, is the critical design criterion that leads to toughening. As we have discussed, extending these discoveries to other metallic glass systems, especially those that are beryllium free, is not a trivial matter. Future work in this area will need to focus on creating two-phase glassy/crystalline microstructures where the shear modulus of each phase can be altered independently. Ultimately, we would like to see high-toughness BMG composites utilizing the low cost of iron.

6.6 Experimental Method

The alloys used in this work were prepared from titanium and zirconium crystal bar and other elements with purity greater than 99.5%. Master ingots of titanium-vanadium were prepared by plasma arc melting, and other elements were pre-alloyed and added later. Semi-solid processing was performed using the method described in [14]. Tension tests and fracture toughness tests were done in accordance with ASTM standards, where applicable (also described in [14]). Samples of crystalline titanium alloys were supplied by McMaster Carr.

References

1. He, G., Eckert, J., Löser, W., Schultz, L.*Nature Materials* **2**, 33 (2003).
2. Das, J., Ettingshausen, F., Eckert, J. *Scripta Mater.* **58**, 631 (2007).
3. Yang, J., Ma, J. Q., Liu, W. M., et al. *Scripta Mater.* **58**, 1074 (2008).
4. Xu, W., Wu, X., Sadedin, D., et al. *Appl. Phy. Lett.* **16**, 1 (2007).
5. Park, J. M., Sohn, S. W., Kim, T. E., et al. *Scripta Mater.* **57**, 1153 (2007).
6. Zhang, L. C., Lu, H. B., Mickel, C., et al. *Appl. Phy. Lett.* **91**, 051906 (2007).
7. Zhang, L. C., Das, J., Lu, H. B., et al. *Scripta Mater.* **57**, 101 (2007).
8. Eckert, J., Das, J., He, G., et al. *Mater. Sci. & Eng. A.* **449**, 172 (2007).
9. Das, J., Kim, K. B., Xu, W., *Mater. Sci. & Eng. A.* **449**, 747 (2007).
10. Das, J., Eckert, J., Theissmann, R. *Appl. Phy. Lett.* **89**, 261917 (2006).
11. Kuhn, U., Mattern, N., Gebert, A., et al. *Intermetallics.* **8**, 978 (2006).
12. Scudino, S., Das, J., Stoica, M., et al. *Appl. Phy. Lett.* **88**, 201920 (2006).
13. Das, J., Kim, K. B., Baier, F., et al. *Appl. Phy. Lett.* **87**, 161907 (2005).
14. Hofmann D. C., Suh, J.-Y., Wiest, A., et al. *Nature* **451**, 1085 (2008).
15. Hays, C. C., Kim, C. P. & Johnson, W. L. *Phys. Rev. Lett.* **84**, 2901 (2000).
16. Szuecs, F., Kim, C. P. & Johnson, W. L. *Acta Mater.* **49**, 1507 (2001).
17. Duan, G., Wiest, A., Lind, M.-L., et al. *Scripta Mater.* **58**, 465 (2008).
18. Peker, A. & Johnson, W. L. *Appl. Phys. Lett.* 63, 2342 (1993).
19. Lin, X. H., Johnson, W. L., Rhim, W.K., *Mater. Sci. Trans.* **38**, 473 (1997).

Chapter 7
High Toughness Metallic Glass Composites as Structural Materials

7.1 Commentary

In this chapter, we investigate the possibility of using the ductile-phase reinforced bulk metallic glasses in the Zr-Ti-Nb-Cu-Be system from Chapter 4 as structural materials. The mechanical properties of the titanium-based composites from Chapter 6 are very similar to crystalline titanium alloys, so we won't discuss them in this chapter. Unlike the titanium-based composites, the zirconium-titanium composites in this chapter have large fracture toughness, room-temperature tensile ductility > 10%, and plastic zone sizes that exceed 1 mm. However, unlike the alloys from Chapter 6, the composites here all have higher density (5.6–5.8 g/cm^3 vs. 4.9–5.2 g/cm^3). We draw comparisons between the glass-dendrite composites and other engineering materials.

7.2 Introduction

For more than fifteen years bulk metallic glasses (BMGs) have been at the frontier of materials research [1–2]. Unfortunately, they have not been widely used in the high-strength engineering applications for which they have so much potential. This is due in part to the fact that the near-theoretical strength observed in these new alloys is negated by brittle failure and a complete lack of tensile ductility in unconfined

loading [7]. This has caused the engineering demand for BMGs to favor secondary properties, such as their low melting temperatures and formability, leading to niche applications [4–5]. Despite strength, BMGs are also known for large elastic limits (~ 2%) [6], a lack of microstructure (allowing for very sharp knife edges), high hardness, specific strength [7], linear-elastic fracture toughness (K_{1C}), extremely high linear-elastic toughness (G_{1C}) [8], and several other specific properties. The aim of this chapter is to investigate whether newly discovered *designed composites* (based on ductile-phase reinforced BMGs) have the design criteria necessary to become structural materials and in some cases replacements for crystalline metals.

Several BMG systems were originally designed as replacements for common materials. Platinum-, palladium-, and gold based BMGs were produced as jewelry [9], it was hoped iron-based BMGs would replace some steel applications, and Zr-Ti BMGs were designed to replace titanium alloys. In fact, the first highly processable BMG, $Zr_{41.2}Ti_{13.8}Cu_{12.5}Ni_{10}Be_{22.5}$ (Vitreloy 1), was developed under DOE and NASA funding to create new aerospace materials, applications where crystalline Ti-alloys are abundant [2]. This work was never realized, however, with the discovery that BMGs exhibit highly localized shear band patterns and no global deformation in room-temperature tension testing. Ductile-phase-reinforced BMGs, where a shear-soft dendrite forms in the glass matrix, alleviated some of this problem by presenting a barrier to shear band extension, leading to ~ 3% tensile ductility [8–9]. To improve properties, the solution involved optimizing the composition and microstructure of metallic glass matrix composites by increasing K_{1C} in the glass matrix and matching its plastic zone size with the length scale of the dendrites [13]. A new series of alloys

was developed in this method with high K_{1C} and near-benchmark G_{1C}, due to the reduced stiffness. Three standout alloys from this series were presented in Chapter 4, DH1–3 ($Zr_{36.6}Ti_{31.4}Nb_7Cu_{5.9}Be_{19.1}$, $Zr_{38.3}Ti_{32.9}Nb_{7.3}Cu_{6.2}Be_{15.3}$ and $Zr_{39.6}Ti_{33.9}Nb_{7.6}Cu_{6.4}Be_{12.5}$, respectively) and were also shown to have > 10% room-temperature tensile ductility with yield strengths of 1.2–1.5 GPa [13]. Figure 7.1 is an example of several of the interesting properties of DH1–3. Figure 7.1(a) shows two 3-mm-diameter tension tests in DH2–3 exhibiting extensive necking. SEM images of the necking are shown in Figure 4.1. Figure 7.1(b) shows a 3-cm-long and 1.5-cm-thick ingot of DH1 cooled on an arc melter, demonstrating the high glass-forming ability of the composites. To demonstrate the bending ductility of DH1, we take a 5-mm-square beam ~ 20 mm long and bend it in a three-point-bend configuration. Even with a low aspect ratio of 4:1, extensive bending is observed. The most ductile monolithic BMGs do not show substantial bending ductility in beams larger than 3 mm square. The difference between monolithic BMGs and our alloy DH3 (the high-toughness alloy) is shown in Figure 7.1(d) a 3-mm-square beam 50 mm long was clamped in a vise and bent with repeated hammer strikes until an angle of > 90° was obtained. The sample exhibits some cracking, owing to the crystalline skull which was not completely removed, and yet the sample has not fractured under the extreme deformation. Further deformation for DH3 is shown in Figure 7.1(e–f), where an 8-mm-thick ingot directly from the arc melter was bent with repeated strikes from a steel pipe.

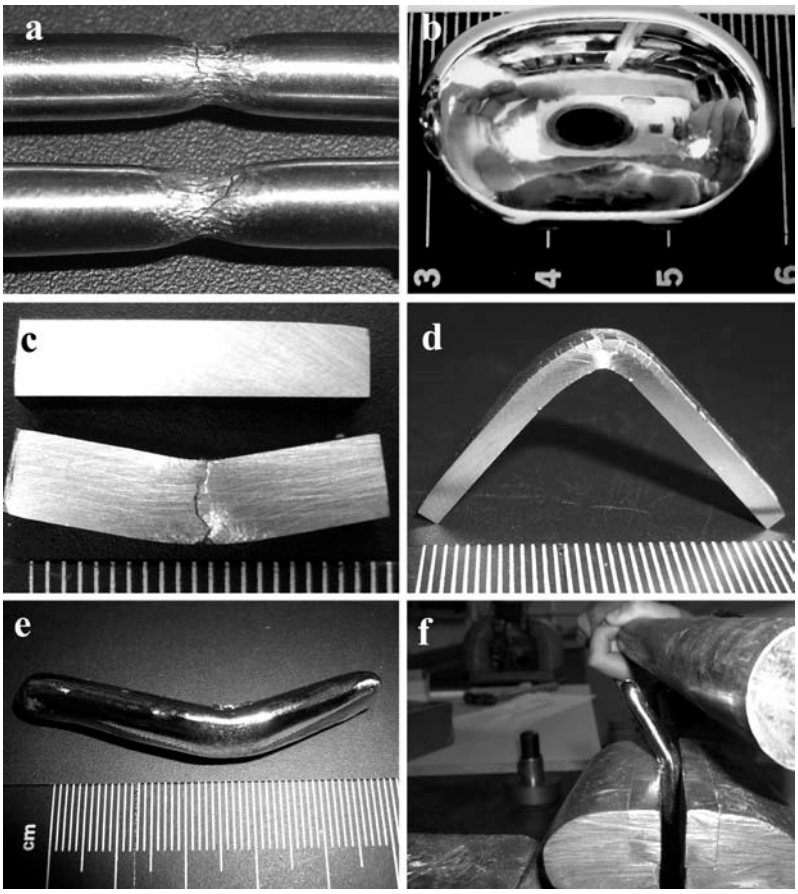

Figure 7.1 – (a) Room-temperature tension test in 3-mm-diameter samples of DH2 (top) and DH3 (bottom) showing extensive necking. (b) as cooled 1.5-cm-thick ingot of DH1 demonstrating a near-mirror finish. (c) 5-mm-square beams of DH1 unbent and bent in a three-point-bend configuration showing extensive plastic strain, despite the low aspect ratio. (d) 3-mm-square beam 50 mm long of DH3 demonstrating extensive bending ductility. In the same dimensions, the toughest monolithic BMGs can only exhibit < 5% bending strain. (e) An 8-mm-thick ingot directly after semi-solid processing bent to a severe angle after repeated strikes with a steel bar (f). It should be noted that bending was stopped before the sample fractured.

7.3 Comparing Properties with Other Engineering Materials

Several factors determine whether or not DH1–3 are adequate as structural material. Crystalline Ti alloys, for example, are used primarily for their high strength and fracture toughness combined with low density and stiffness [13]. The benefits of using BMG-matrix composites (DH1–3) over other suitable crystalline materials are best illustrated with a plot of fracture toughness (K_{1C}) versus yield strength (σ_y). Figure 7.2 is a plot used for selection of materials and shows broad ranges of areas occupied by metals, ceramics, and polymers. The metallic glasses that are plotted (Pd-, Pt-, Zr-, Cu-, Zr-Ti- and Fe- based BMGs) have K_{1C} values that range over two orders of magnitude (1–100 MPa $m^{1/2}$) all with $\sigma_y > 1$ GPa. It should be noted that many of the fracture toughness values for BMGs do not accurately report K_{1C} (which strictly measures plane-strain conditions). Many of the high-fracture toughnesses reported are measured in ribbons, where plane stress effects inflate fracture toughness. The highest value for K_{1C} in a monolithic metallic glass is 50–60 MPa $m^{1/2}$. Although it has been pointed out that the highly toughened composites from Chapter 4 were measured in plane-stress conditions, we have recently shown that these values are still accurate estimations. The diagonal contour lines in Figure 7.2 are the plastic zone sizes (also known as the process zone) which are defined as $d = K_{1C}^2/\pi\sigma_y^2$ (mm) [8]. The plastic zone size is a crucial property for determining the suitability of a material for a structural application. If the size of d is much smaller than the sample size, fast fracture occurs and the material appears brittle. Conversely, if d is sufficiently large, ductile fracture is observed and the material fails gracefully. Much of Figure 7.2 demonstrates what is expected intuitively in the behavior of materials. For instance,

lead alloys fail in a ductile manner and have $d \sim 1$ m, despite their low K_{1C} (10–20 MPa $m^{1/2}$). Polymers have extremely low K_{1C} (< 10 MPa $m^{1/2}$), yet they exhibit failure that ranges from ductile to almost glass-like. This is explained by their plastic zone size, which ranges from 0.2–100 mm. Steel is among the most versatile of all engineering materials due to its high fracture toughness (typically > 100 MPa $m^{1/2}$) and its broad range of yield strengths (100–1000 MPa) and plastic zone sizes (5–500 mm). Ti alloys however, occupy a much smaller region of Figure 7.2, exhibiting $K_{1C} \sim$ 50–100 MPa $m^{1/2}$, $\sigma_y \sim$ 0.8–1.5 GPa and $d \sim$ 1–5 mm. Ti alloys are typically known for their low density and high strength, combined with considerable toughness, but Figure 7.2 demonstrates that their use as a structural material is limited to relatively small samples (typically < 1 cm thick) because they exhibit small plastic zone sizes. Ti alloys are thus not attractive as steel replacements for many applications because they exhibit brittle failure above a certain sample size. Despite this drawback, Ti alloys have a wide variety of uses that are not limited to niche applications. Although monolithic BMGs can exhibit high K_{1C} (~ 100 MPa $m^{1/2}$) they are confined to the region in Figure 7.2 where d < 1 mm, due to their high strengths. This means that BMGs are worse than some ceramics in terms of their plastic zone size. This "size effect" in BMGs is well documented in bending tests, where samples below a thickness of 1 mm show substantial plasticity but exhibit brittle failure when the sample size is increased above 1 mm [22–24]. Thus, as structural materials, BMGs are not attractive.

The increased K_{1C} obtained in the ductile-phase reinforced BMGs (DH1–3) allows them to pierce the d = 1 mm barrier observed in monolithic BMGs without

sacrificing yield strength. Figure 7.2 shows that DH3 is an especially good structural material due to its similar yield strength to some crystalline Ti alloys (such as Ti-6Al-4V), but with higher K_{1C} (173 versus 43 MPa $m^{1/2}$) and larger d (8 versus 1 mm). Even with lower values for K_{1C} (the highest reportable ASTM value we currently have is 140 MPa $m^{1/2}$ based on limitations in sample thickness), the composites still have a plastic zone size larger than 1 mm. This explains why the bending ductility in the composites (Figure 7.1) is superior to any known monolithic metallic glasses.

7.4 Production

Unlike iron, which is abundant in nature, titanium does not occur naturally and must be produced by the expensive Kroll process [13], among others. This causes crystalline Ti alloys to be several times more expensive than steel. The BMG composites DH1–3 are comprised of ~ 25% by weight Ti and typically 50% by weight Zr. Lab-scale BMG composites are produced under vacuum to prevent oxygen embrittlement; however, commercial BMGs are not. Although both titanium and BMG composites react vigorously with oxygen, the production of common structural components (billets, sheets, bars, tubes, plates) will undoubtedly be more complex with the BMG composites, mostly due to glass crystallization issues. Despite this, DH1–3 and other Vitreloy-type BMGs can be produced commercially at nearly the same cost as high-performance Ti-alloys. This is done by utilizing commercial-grade and recycled starting materials, which seem to have little effect on glass-forming ability or mechanical properties.

Crystalline Ti alloys are frequently used in high-temperature applications, such as aircraft engines, helicopter exhaust ducts, fire walls, and external spacecraft components. One might think BMG composites that have a glass transition temperature ~ 620 K are unfit for such uses, but on the contrary, many Ti alloys lose their strength when heated to > 700 K, even though they melt at ~ 2000 K [13]. Another criticism of the BMG composites is their density relative to crystalline Ti alloys. Although we have recently produced Ti-based BMG composites with densities similar to crystalline Ti alloys, the composites in this chapter are not significantly less suitable. Figure 7.3 is a plot of K_{1C} versus density over a wide range of engineering materials. Typically, Zr-based monolithic BMGs exhibit density > 6 g/cm^3 and have a wide range of K_{1C} values. The alloys DH1–3 have a lower density (5.6–5.8 g/cm^3), due to increased Ti content, and have among the highest K_{1C} values for materials with that density. In terms of specific strength, defined as yield strength divided by density, the composites are very similar to crystalline Ti alloys. DH1–3 and Ti-6Al-4V have specific strengths of 0.20–0.28 GPa cm^3/g and 0.25 GPa cm^3/g, respectively.

7.5 Conclusion

The recently developed high-toughness BMG composites seem well suited for structural applications. Many industries could benefit from fracture-resistant metals with high strength, large elastic limit, and relatively low density.

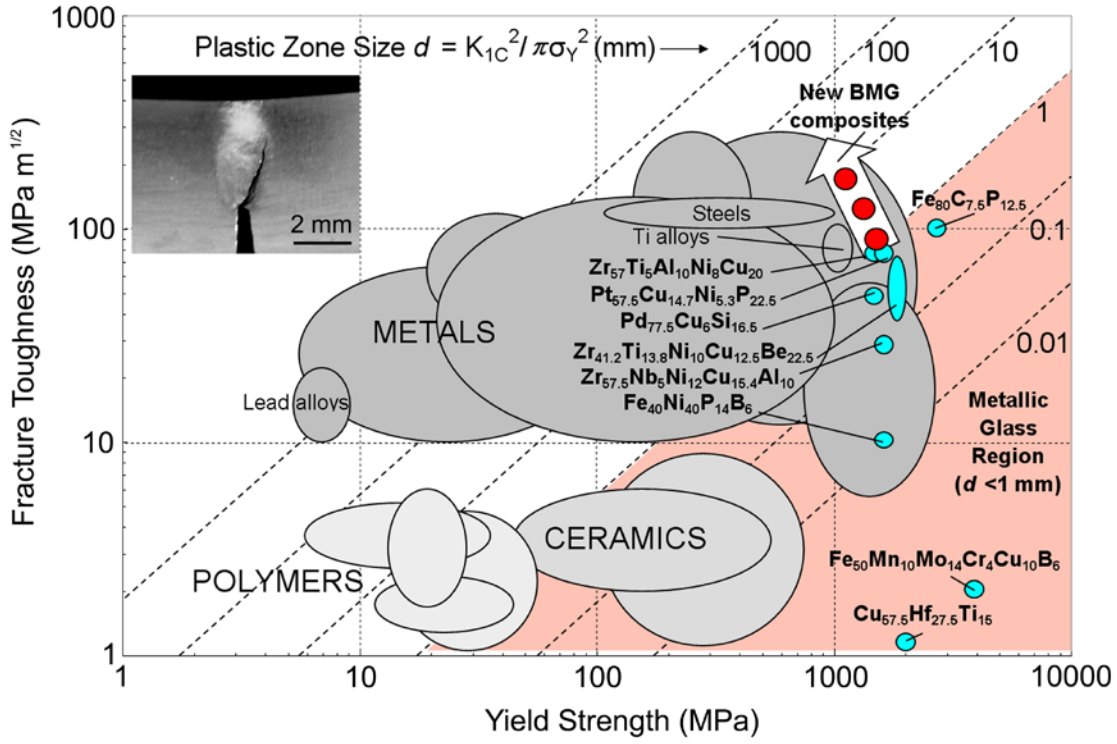

Figure 7.2 – Ashby plot of fracture toughness versus yield strength showing general classes of engineering materials and metallic glasses. Diagonal contour lines are plastic zone sizes and crack arresting in DH1 is shown in the inset. The BMG composites pierce the 1 mm plastic zone barrier that confines all monolithic BMGs.

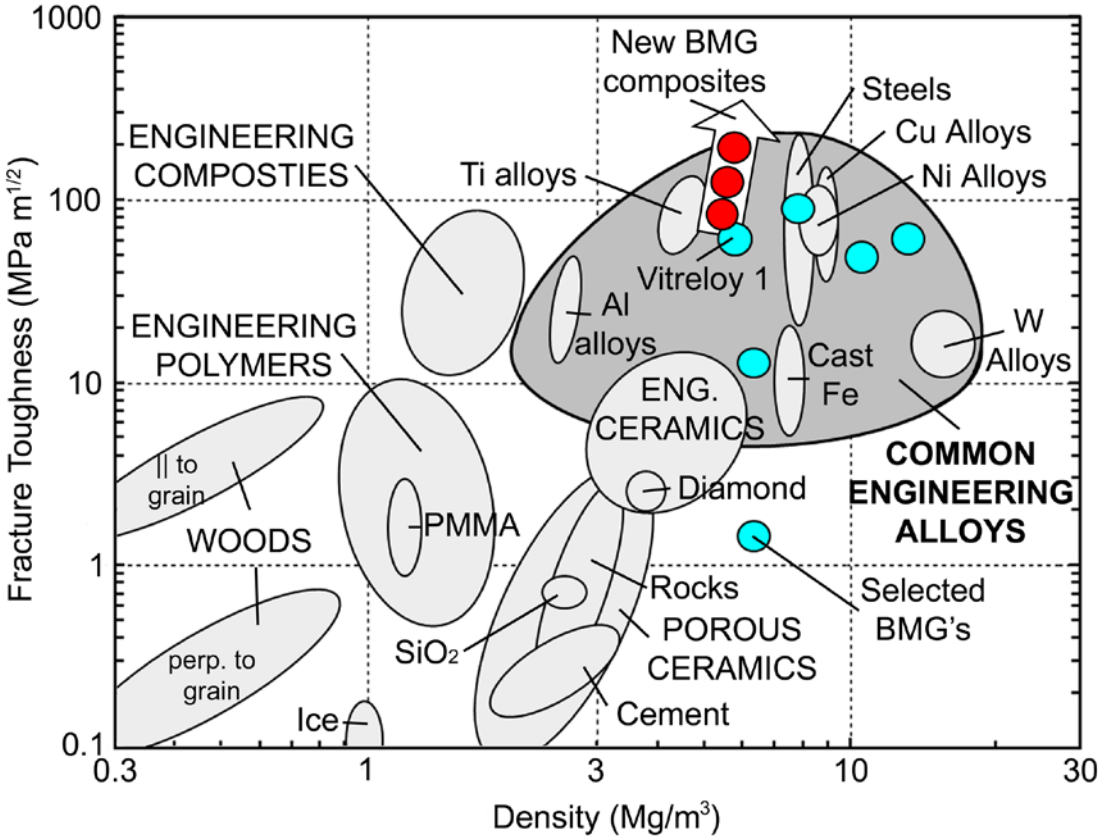

Figure 7.3 – Ashby plot of fracture toughness versus density showing general classes of engineering materials and metallic glasses. The BMG composites have high fracture toughness with density similar to crystalline titanium alloys.

References

1. Telford, M., *Mater. Today* **7,** 36 (2004).
2. Greer, A. L., Ma, E., *MRS Bulletin* **32**, 611 (2007).
3. Rao, X., et al. *Mater. Lett.* **50**, 279 (2001).
4. Inoue, A., Nishiyama, N., *MRS Bulletin* **32**, 651 (2007).
5. Schroers, J., et al. *J. Microelectromechanical Sys.* **16**, 2 (2007).
6. Greer, A. L., *Science* **267**, 1947 (1995).
7. Salimon, A. L., et al. *Mater. Sci. and Eng. A* **375-377**, 385 (2004).
8. Ashby, M. F., Greer, A. L., *Scripta Mater.* **54**, 321 (2006).
9. Schroers, J., Johnson, W. L., *Appl. Phys. Lett.* **84**, 18 (2004).
10. Peker, A., Johnson, W. L., *Appl. Phys. Lett.* **64**, 2342 (1993).
11. Hays, C. C., Kim, C. P., Johnson, W. L., *Phys. Rev. Lett.* **8**, 2901 (2000).
12. Szuecs, F., Kim, C. P., Johnson, W. L., *Acta. Mater.* **49**, 1507 (2001).
13. Hofmann, D. C., Suh, J.-Y., Wiest, A., et al. *Nature* **451**, 1085 (2008).
14. Barksdale, J., *The Encyclopedia of the Chemical Elements.* (Reinhold Book (Corporation, Skokie, 1968).
15. Conner, R. D., Paton, N. E., Nix, W. D., Johnson, W. L., *J. Appl. Phys.* **94**, 904 (2003).
16. Conner, R. D., Li, Y., Nix, W. D., Johnson, W. L., *Acta Mater.* **52,** 2429 (2004).

Appendix A (Supplementary Material for Chapter 4)

This appendix contains a substantial amount of work that I was unable to organize into coherent chapters. It begins with the supplementary material used to support the claims from Chapter 4 and continues with other material that is currently unpublished.

In Chapter 4, we've identified the factors responsible for the ductility and toughness of these BMG matrix composites, particularly (1) a homogenous microstructure and (2) the optimization of length scales L and S that prevent shear bands from extending to distances that would lead to crack opening. Further, we show that the shear modulus of the dendritic phase is significantly lower than the matrix. This results in deformation initiating within the dendrites. It allows extensive deformation without fracture and enhancement of toughness and tensile ductility. This paper is the first to explain the mechanism of toughening and experimentally use this knowledge to optimize engineering properties. Additionally, while the new composites appear to be of similar composition to earlier-reported in-situ composites, they are based in a completely different glassy matrix. The matrix material of the previous composites was similar to Vitreloy 1, a somewhat low fracture toughness glass while the new composites are based in GHDT, a high fracture toughness, low shear modulus BMG with the largest supercooled liquid region ever discovered. The alloys are similar in composition but far different in properties.

The Ashby map included in the original manuscript (Figure 4.4) depicts useful property combinations of known materials. The present materials are exceptional

among known engineering materials. Alloys with the most similar mechanical properties and density to DH1-3 are high-performance Ti-alloys. As a side note, commercially manufactured BMGs are clearly not prohibitively costly since they are already in broad use in cell phone cases, electronic cases, sports equipment, etc., produced by Liquidmetal Inc., in California. These materials are comparable in cost with commercial Ti alloys.

The b.c.c. phase develops by crystal nucleation, dendrite development, and subsequent dendrite “tree” growth. The topology of a dendrite tree is an embedded and isolated crystal within a surrounding matrix. Growing dendrites never impinge or become conjoined. The final morphology is that of isolated crystals in a glass matrix. The dendritic crystals do not form a percolating path and do not comprise a continuous matrix; rather the remaining liquid/glass is the only continuous phase. Deformation in both phases is seen in Figure 2(d-e) of Chapter 4. Plastic deformation begins in dendrites at stress levels far below the yield stress of the glass. As deformation initiates in the dendrite, stress is transferred to the surrounding glass and shear bands are subsequently initiated in the glass phase, as stress concentration there is greater. These shear bands lengthen and extend under further deformation. The local shear bands have an orientational relationship related to the easy slip directions of the local dendrite. Thus, the orientation of shear bands formed around a single dendrite tree has a crystallographic relationship with the dendrite. The mis-orientation of neighboring dendrites inhibits extension of the shear band patterns from the region around one dendrite tree to that of a neighboring tree, since neighboring dendrite orientations are uncorrelated. This limits the extension of the shear bands around one dendritic domain

to lengths on the order of L or S. When these lengths are less than R_p, shear bands do not evolve into opening cracks and fracture is avoided. This is the basic mechanism behind the exceptional ductility and toughness of the materials.

The micrographs in Figure 4.1 represent small, two-dimensional images of the alloys and do not represent the full microstructure, only an example of it. After taking many SEM micrographs we loaded the figures into image analysis software in Matlab and analyzed phase fractions (using the contrast). After averaging over many of the images, we obtained the percentages listed in the manuscript.

We have several other independent methods of assessing the glass volume fraction. These include DSC analysis of the heat released when the glass matrix crystallizes, X-ray diffraction analysis, and rule of mixture analysis of elastic properties, all of which lead to estimates of the glass volume fraction consistent with image analysis. We have DSC scans of the three alloys DH1–3 and the glass matrix material from DH1, which is very similar to the matrix of the alloys DH2–3. Each alloy shows clear glass transition temperatures and eutectic crystallization events with the composites having a slightly smaller supercooled liquid region. This is the exact trend observed in previous work on in-situ BMGs. By dividing the heat of crystallization in DH1 by the DH1 matrix (a single-phase glass) we obtain 58.7% glass, 50.0% glass, and 32.7% glass for DH1–3 respectively. The values obtained through image analysis were 58%, 49%, and 33%, respectively. Microprobe analysis has demonstrated that Be does not partition into the dendrite, so by reducing the overall atomic percentage of Be in the composites, the volume fraction of the glass phase *must* decrease.

Based on the (1) image analysis, (2) DSC analysis of glass "heats of crystallization," (3) X-ray diffraction results, etc., which are mutually consistent, we have an exceptionally high level of confidence in our estimates of the volume fractions of the two phases.

The apparent fine white particles in backscattered SEM images of the microstructures were artificially created during contrast enhancement. The glass matrix is fully amorphous. The dendrites and the glass matrix have similar compositions, so when obtaining backscattered images in the SEM, there is little contrast difference. To clearly demonstrate the microstructure, we enhanced the contrast of the micrographs, creating the appearance of a grainy texture which does not exist. From the high-resolution TEM micrographs, the glass matrix is amorphous down to atomic resolution. This is also verified by the amorphous diffraction pattern.

We also demonstrate that the glass matrix is amorphous in several other ways. First, we have calculated the dendrite composition and the glass matrix composition through EDS and have produced a sample of the matrix alloy for DH1 (which is similar to the glass matrix of DH2–3). The alloy is a clear bulk glass former, as verified by X-ray and DSC. The DSC scan demonstrates that the DH1 matrix alloy exhibits a large (122 K) supercooled liquid region and a large eutectic crystallization event, both typical of an excellent bulk glass former. The X-ray diffraction scan is further evidence that the alloys DH1–3 contain two phases, one b.c.c. crystalline and the other glassy. We have XRD scans of the dendrite material, which exhibits clear b.c.c. peaks, the glass matrix material, which exhibits two broad diffuse halos typical of a bulk metallic glass, and the composite DH1, which is a superposition of the two.

No other crystalline peaks are visible in the composite and the broad diffuse background is still present, indicating only the b.c.c. and glassy phases. The evidence for only two phases is unambiguous. The X-ray scans are similar for DH2–3. We have also included backscattered SEM micrographs with unaltered contrast taken at higher magnification from the alloy DH1.

We present further evidence of the two-phase mixtures in DH1–3 by plotting shear modulus versus the volume fraction of b.c.c. phase, as calculated through image analysis and DSC. We have produced and measured the shear modulus for the glass matrix of DH1, the dendrite material of DH1, and the composite DH1. As discussed in the manuscript, the glass matrix has a higher shear modulus than the b.c.c. dendrite, and the composite shear modulus follows a rule-of-mixtures average of the two. Calculating the volume fraction of b.c.c. phase from this method yields 44% dendrites, in excellent agreement with the phase fraction estimated by the other methods. This analysis is also valid for DH2–3, though the matrix and dendrite have slightly different composition.

There seems to be a misunderstanding of the interdendrite spacing S. The interdendrite spacing is the distance from the center of a single dendrite tree to the center of an adjacent one, while the dendrite size, L, is the total spanning length of a single dendrite tree. It should be noted that the entire tree with its arms and trunk comprise at least a semi-coherent single b.c.c. crystal. Further, two neighboring dendrite trees are single crystals of differing orientation. Since nucleation of dendrites is a random process producing equiaxed crystal orientation, the orientations of neighboring dendrite trees is uncorrelated, unlike neighboring arms of a single

dendrite tree which, tend to have the same orientation. Both S and L are difficult to estimate from two-dimensional images because dendrites are three-dimensional tree-like structures. The 10 μm distance alluded to by the referee is the characteristic spacing of the dendrite arms in a single dendrite tree, commonly called the "arm spacing." Indeed, this is about 10 μm. The value of the dendrite tree size, L, can only be measured accurately from two-dimensional images when the slice passes through the center of a dendrite tree. The images make dendrite tree sizes appear to vary far more than they actually do because two-dimensional cross sections cut dendrite trees at various distances from the center, making the dendrite projection appear smaller than the actual dendrite size. Nevertheless, by surveying two-dimensional micrographs we can estimate the spanning length of a typical dendrite to be in the range of 60–120 μm, roughly an order of magnitude greater than the arm spacing of the dendrite tree.

In addition, as the TEM images in Figure 4.1 demonstrate, there is no heterogeneous nature of the glass phase. The plasticity and benchmark toughness are *not* an intrinsic property of the bcc material. The b.c.c. material typically actually exhibits yield strength of ~ 700 MPa and fracture toughness less than 100 MPa $m^{1/2}$. The new properties demonstrated in the composites far exceed both those of the BMG matrix material and those of the b.c.c. dendrite. This clearly shows that the combination of the two phases leads to the benchmark properties.

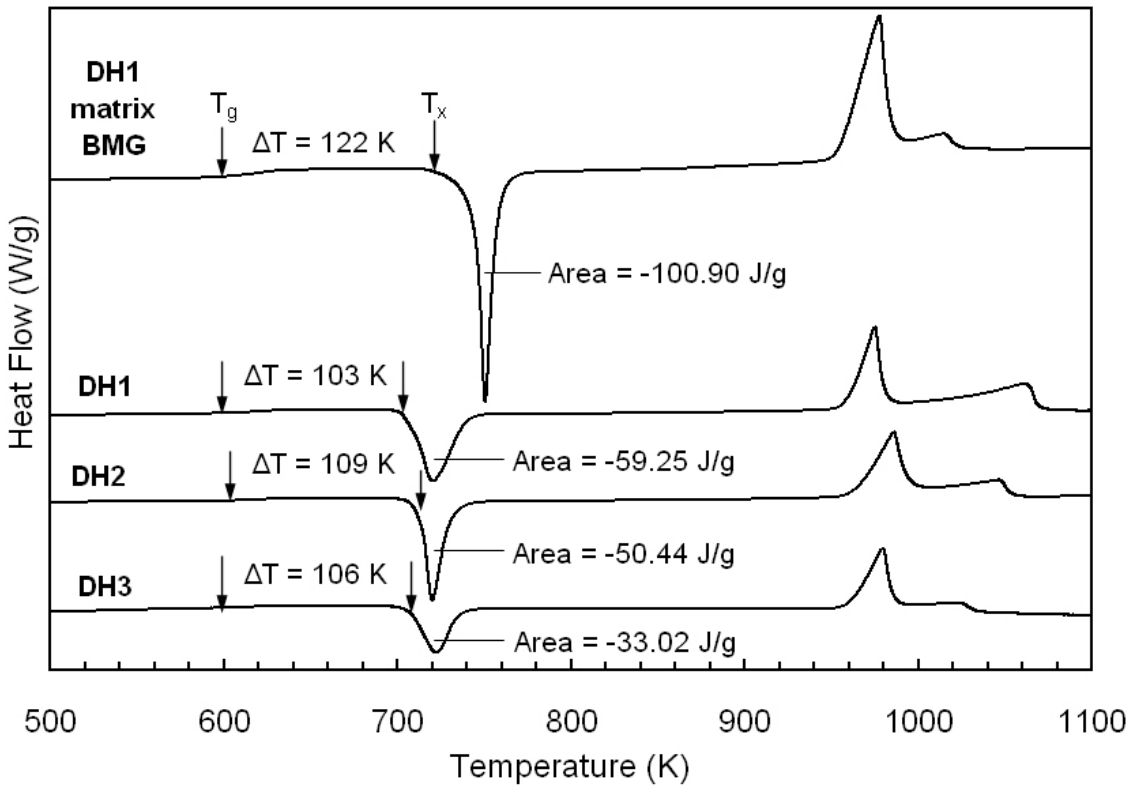

Figure A1 – DSC curves from the alloys DH1–3 and the glass matrix of DH1. In each alloy, a clear glass transition is visible along with a eutectic crystallization event. The heat of crystallization in DH1–3 relative to the heat of crystallization in the matrix alloy is an estimation of the volume fraction of glass. This method verifies image analysis done using computer software. The DSC tells us that the alloys are, in fact, comprised of glass, and the volume fraction of glass is less than that of a fully amorphous sample.

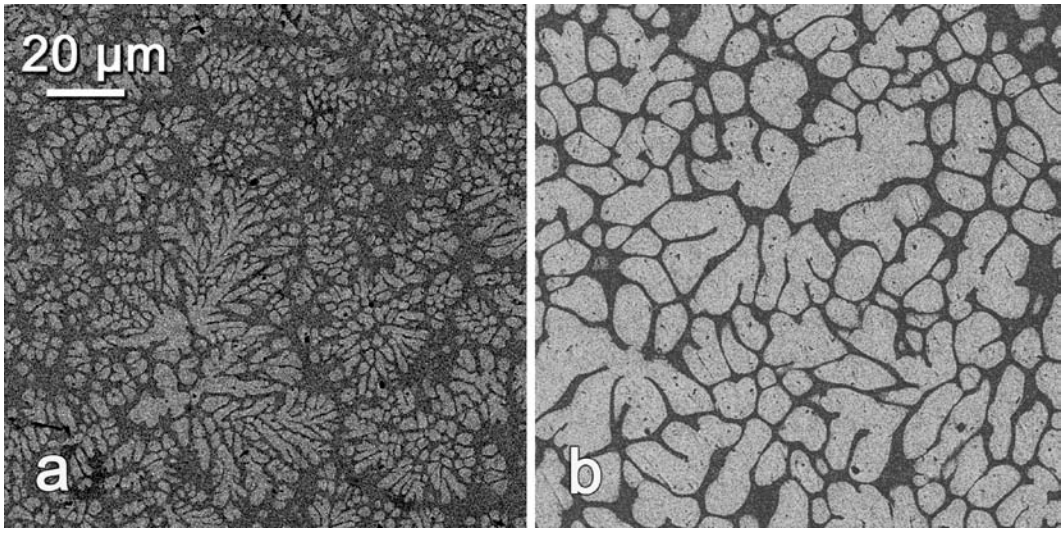

Figure A2 – (a) Contrast adjusted backscattered SEM micrograph of DH1 with composition $(Zr_{45.2}Ti_{38.8}Nb_{8.7}Cu_{7.3})_{80.9}Be_{19.1}$, and (b) a higher-volume fraction alloy with composition $(Zr_{45.2}Ti_{38.8}Nb_{8.7}Cu_{7.3})_{91}Be_{9}$. Since Be does not partition into the dendrite, reducing the Be in the total alloy composition leads to a smaller volume fraction of glass phase. This illustrates why the alloys DH1–3 have increasing volume fraction of dendrites, even though selected SEM micrographs may appear to show otherwise. As a note, the contrast has been increased to differentiate the two phases, making it appear as though the glass phase has a heterogeneous instead of amorphous microstructure. The scale bar applies to both images. Partitioning works because Be is not soluble in b.c.c. titanium and zirconium. This is the key feature to be used in other systems to design composites. For example, B is not soluble in f.c.c. Fe or Ni.

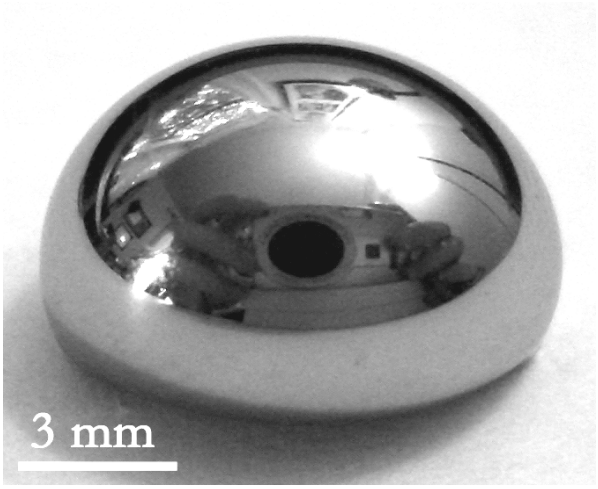

Figure A3 – (a) 7-mm-thick fully amorphous ingot of the matrix BMG for the alloy DH1, demonstrating that it is a bulk glass former. This BMG has similar composition to the matrix alloys of DH2–3 and exhibits a lustrous, mirror-like finish when cooled in ingot form on the arc melter. The matrix alloy of DH1 was cooled fully amorphous up to 7 mm on the water-cooled Cu boat, and is estimated to have a critical casting thickness of 1.5 cm in quenched cooling. The X-ray diffraction pattern for this BMG shows two broad, diffuse halos, typical of an amorphous BMG. This figure is used to contest the claim that the matrix material is not amorphous. We show here that it is an excellent bulk glass former.

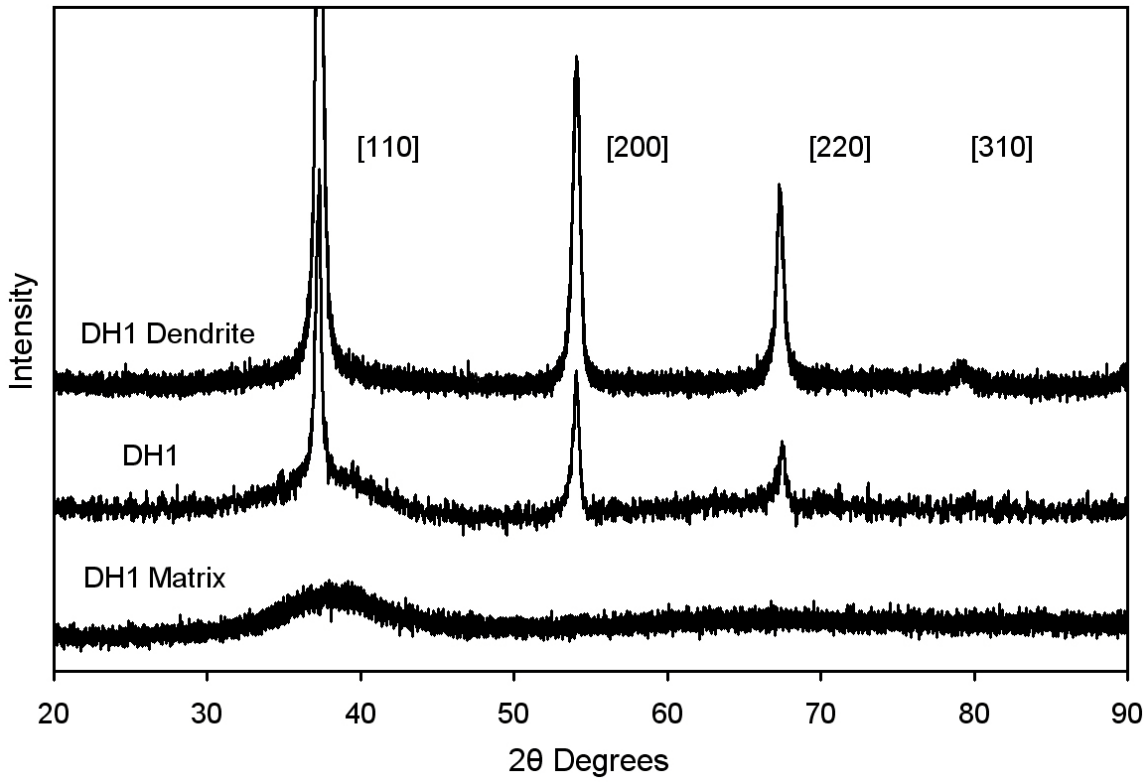

Figure A4 – X-ray diffraction data for DH1 showing the b.c.c. dendrite material, the fully amorphous glass matrix, and the composite, which is a superposition of the two. DH1 is thus a combination of a glass matrix and a b.c.c. dendrite. If the glass matrix were partially crystalline, erroneous peaks would be visible in the X-ray scan of DH1. This holds true for DH2 and DH3, although not shown. Additionally, the amorphous background from the glass matrix is still visible in the scan from DH1. This scan demonstrates that two phases are present, but it does not say anything about the mechanical properties of the phases other than that they are b.c.c. plus glass. Shear modulus data is also needed.

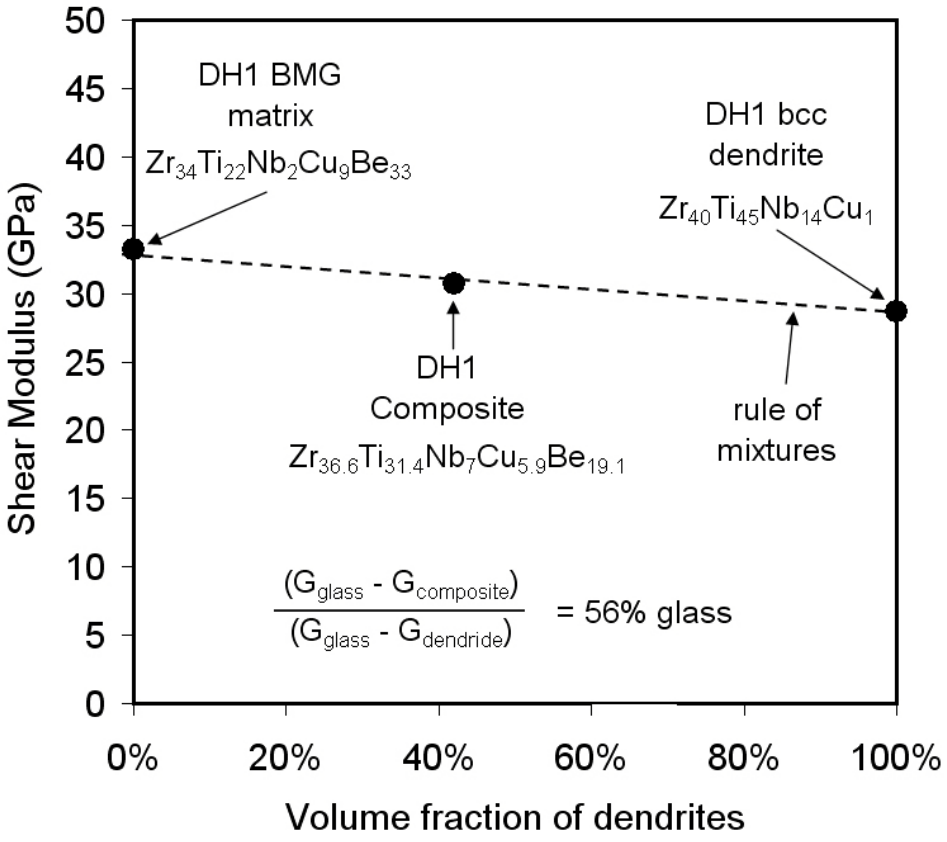

Figure A5 – Plot of shear modulus versus volume fraction of dendrites for the alloy DH1, its glass matrix, and its dendrite. The glass matrix has a higher shear modulus (~ 33 GPa) than the b.c.c. dendrite (~ 28 GPa), indicating that the dendrite is a soft inclusion. The composite DH1 is a rule of mixtures average of the glass matrix and the dendrite, indicating that it is truly a two-phase alloy. Calculating the volume fraction of glass by this method yields 56%, in excellent agreement with image analysis and DSC scans. The results are similar for DH2–3 with slightly different slopes due to the different compositions of glass matrix and dendrites. Note that the dendrite material is titanium rich and the glass matrix is zirconium rich. Also note that the estimated error in these measurements is 0.2 GPa.

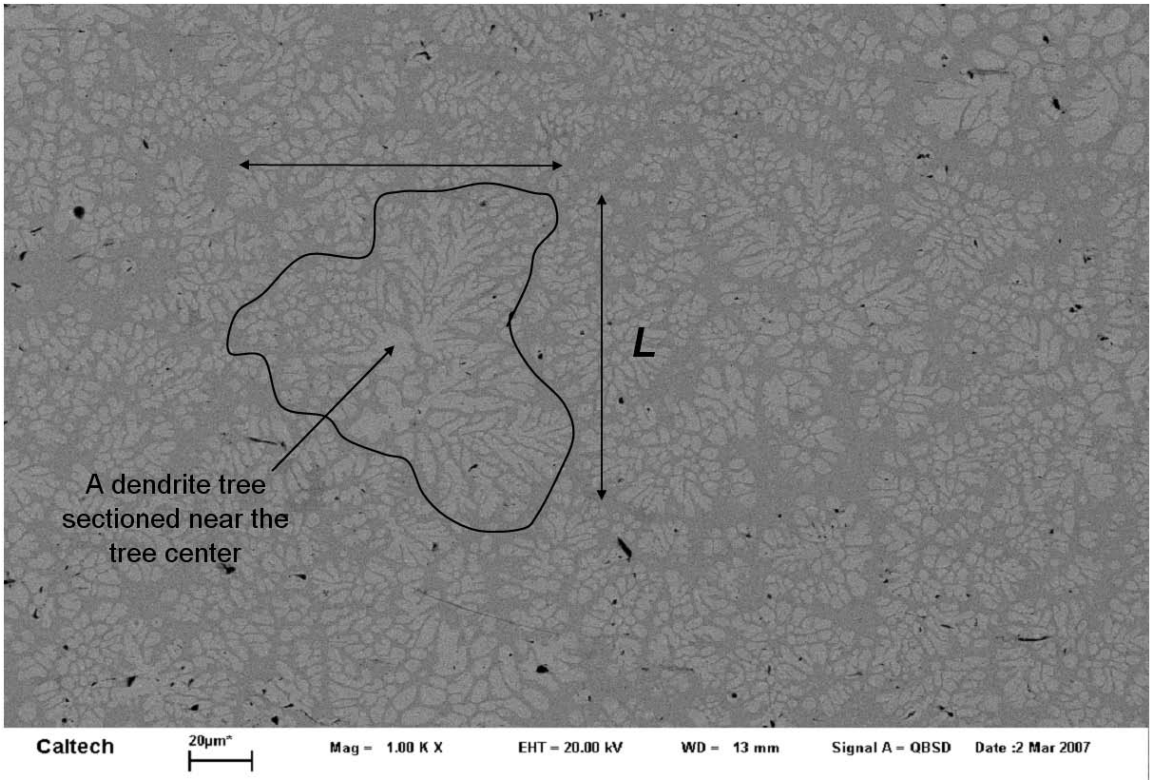

Figure A7 – Backscattered SEM micrograph of the microstructure of DH1. A single dendrite tree which has been cross-sectioned near its central nucleation point is illustrated with the dark curve. An estimate of the spanning length, *L*, is indicated by the arrows ($L \sim 100$ µm). Other dendrite cross sections capture only portions of the trees. This figure is used to support the length scale claims made in Chapter 4 and to dispute the claims made by a reviewer that the dendrites were smaller than reported.

Figure A8 – Optical images of large ingots of Vitreloy 1 and DH1. (a) Bars produced on the water-cooled Cu boat of Vitreloy 1 (top) and DH1 (bottom). The ingot of DH1 is > 5 cm long and 1 cm thick. (b) Arc-melted ingots of Vitreloy 1 (left) and DH1 (right). Both ingots have masses > 25 g and have thickness > 1.2 cm. These ingots do *not* represent the critical thickness of DH1–3 but merely reflect ingot sizes used. This figure is used as a demonstration of the large glass-forming ability of this system.

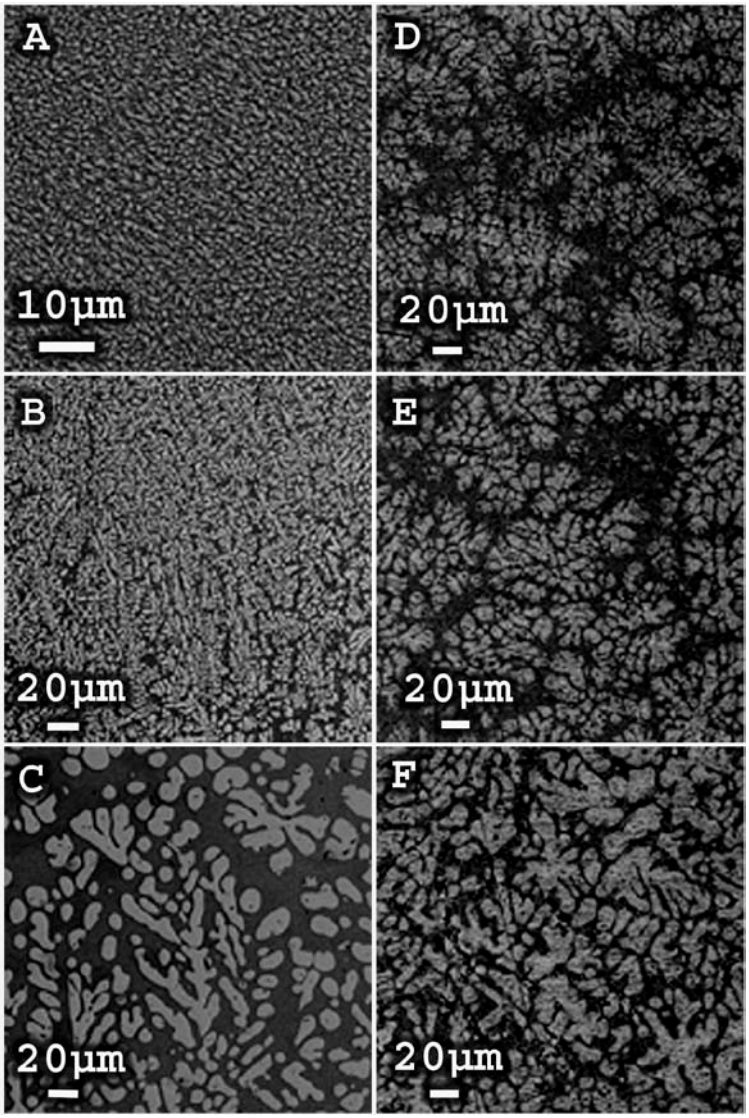

Figure A9 – Comparison of uncontrolled microstructure versus semi-solid processing. (a-c) Backscattered SEM micrographs from an approximately 7-mm-thick ingot of an in-situ composite cooled on an arc melter (reproduced from S. Lee, *thesis; Caltech*, 2005). (a) Taken from the top of the ingot showing a dendrite size of 0.4–0.6 µm. (b) Taken from the middle of the ingot showing a dendrite arm size of 2–4 µm. (c) Take from the bottom of the ingot showing a dendrite arm size of 8-12 µm. (d-e) Backscattered SEM micrographs from a 7-mm-thick bar of DH2 produced on the water-cooled Cu boat in the semi-solid region. (d) Taken from the top of the bar. (e) Taken from the middle of the bar. (f) Taken from the bottom of the bar. The dendrite arm size varies from 5–15 µm throughout the ingot. This image demonstrates that semi-solid processing produces a more uniform microstructure which varies minimally with cooling rate. Since tensile ductility rapidly falls with dendrite size, the more homogeneous microstructure of DH2 leads to a highly toughened composite.

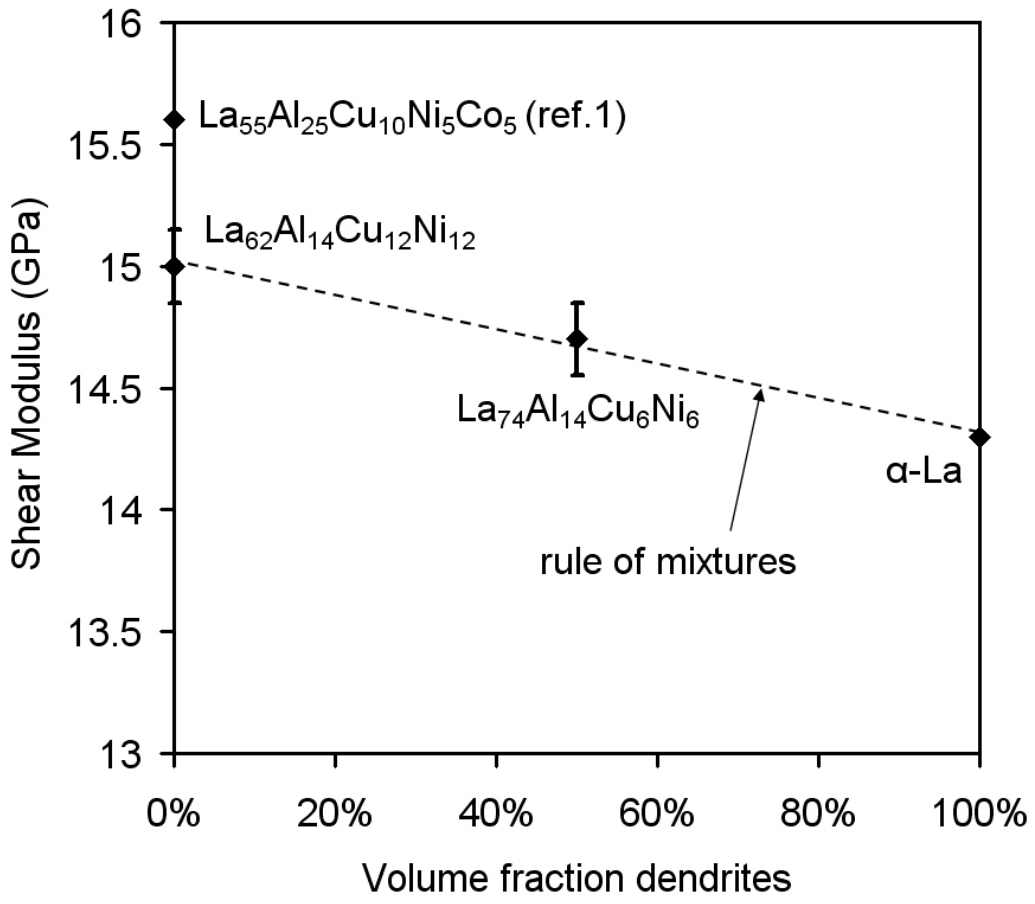

Figure A10 – Plot of shear modulus versus volume fraction of dendrites for a La-based metallic glass, its glass matrix, and its dendrite (Yi Li's group, 2005). The glass matrix has a higher shear modulus (~ 15 GPa) than the dendrite (~ 14.3 GPa), indicating that the dendrite is a soft inclusion. This system exhibits ~ 5% ductility in tension. The concept of a soft dendrite was not discussed in this paper but fortunately, the pure La is softer than the glass matrix, leading to ductility.

Appendix B (Fracture Toughness Revised)

This appendix contains recently obtained data regarding fracture toughness of the alloy DH3 from Chapter 4. In that chapter, we attempted to quantify the fracture toughness of our ingots and we ran into several problems. First, the literature on BMGs seems to overstate the true fracture toughness (K_{1C}) of these brittle materials. Values are commonly reported up to 100 MPa $m^{1/2}$, and yet further examination of these measurements reveals that they are performed predominantly in plane-stress conditions. Plane-stress values can be up to twice as high as plane-strain measurements, and K_{1C} is supposed to be measured in plane-strain. Second, we initially had sample limitations on our alloys, based on the geometry of the Cu boat. To make the comparisons fair, we measured K_{1C} for the composites in the same dimensions as we measured monolithic BMGs. Unfortunately, the ASTM standards for fracture toughness indicate that for every sample thickness there is a maximum value for K_{1C} that can be reported. Tougher alloys require larger samples. In Chapter 4, we claimed the alloy DH3 had an estimated $K_{1C} \sim 170$ MPa $m^{1/2}$. This value, however, requires a 6-cm-thick sample for the value to be valid.

Recently, a renowned fracture mechanics group claimed that our estimations were completely unreliable. They claimed that once the ASTM standard value for a particular thickness is reached, any value above that is completely miscellaneous. The group claimed that increasing the thickness of our alloys would reduce the measured value dramatically. To defend the claims from our publication, we produced thicker

samples and measured the fracture toughness. We produced a 4.2-mm-thick sample and a 4.8-mm-thick sample. Additionally, we also measured a sample directly from the arc melter, without undergoing semi-solid processing, to quantify the effect of changing the microstructure. In this thesis, we will not go into detail about actual K_{1C} measurement, only the results. More detail can be found in Jin-Yoo Suh's Caltech thesis.

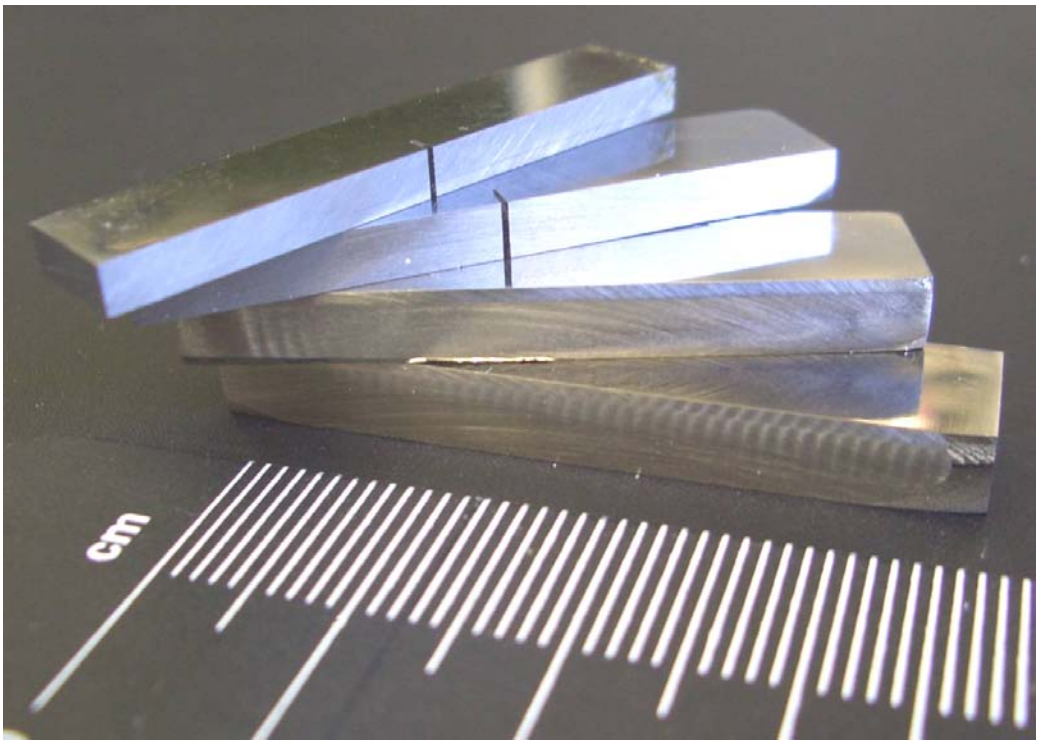

Figure B1 – Different thickness samples used for fracture toughness experiments. As we discover, our measurements of fracture toughness are nearly independent of thickness but rely heavily on semi-solid processing.

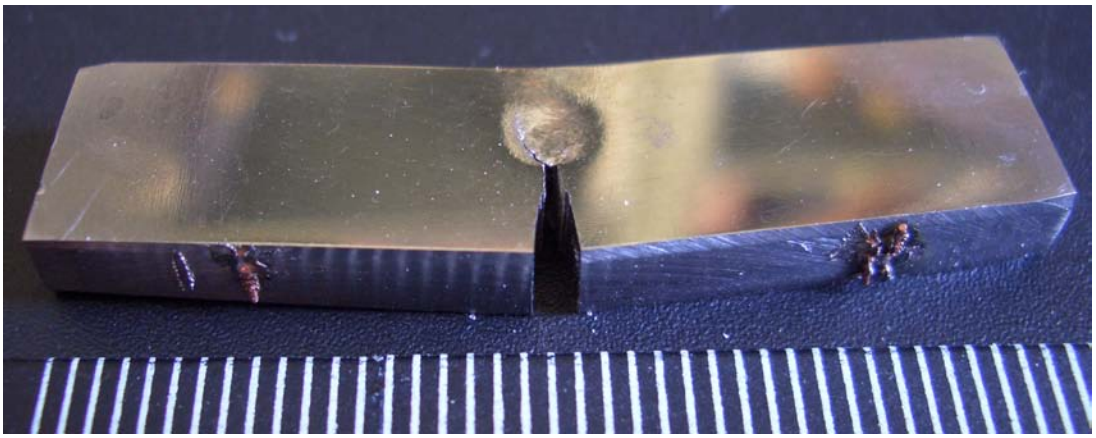

Figure B2 – A 4.2-mm-thick K_{1C} specimen of the alloy DH3. Even at the larger thickness (compared to 2.5 mm in Chapter 4) the sample demonstrates complete crack arrest and exhibits a plastic zone several millimeters in size. The plastic zone seems to be even larger than in the thinner 2.5 mm sample. The measured K_{1C} is 170 MPa $m^{1/2}$, which exceeds the sample limitations. The maximum reportable K_{1C} for this sample is ~ 125 MPa $m^{1/2}$.

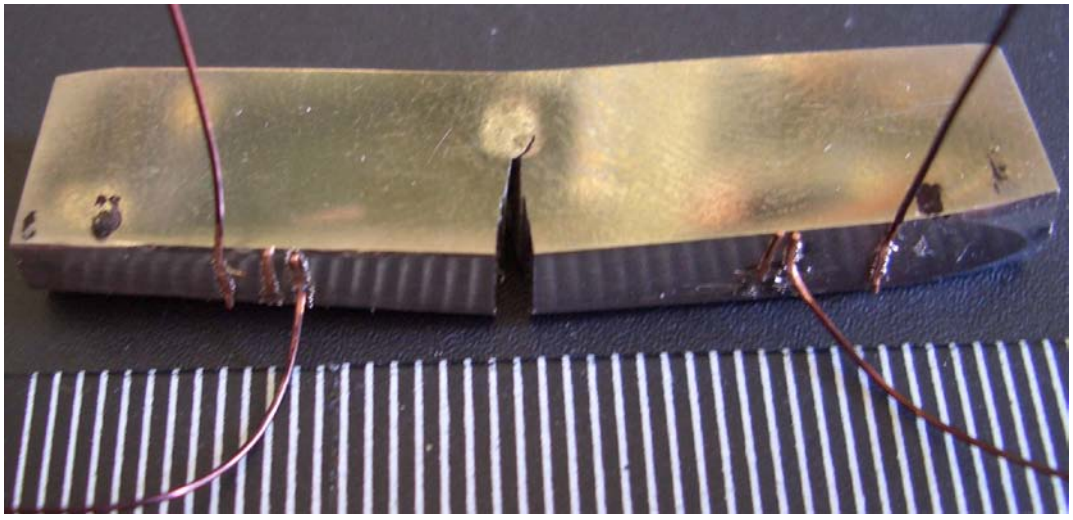

Figure B3 – A 4.8-mm-thick specimen of DH3 with wires attached for electrical resistance measurements used to track crack growth. Even at this much larger thickness, complete crack arrest is observed. The measured K_{1C} is 168 MPa $m^{1/2}$, which exceeds the sample limitations. The maximum reportable K_{1C} for this sample is ~ 140 MPa $m^{1/2}$. Currently, this is the highest fracture toughness value that we can obtain. We have recently produced a 5.5-mm-thick sample, which will allow us to measure K_{1C} values in excess of 150 MPa $m^{1/2}$. This sample is still under investigation.

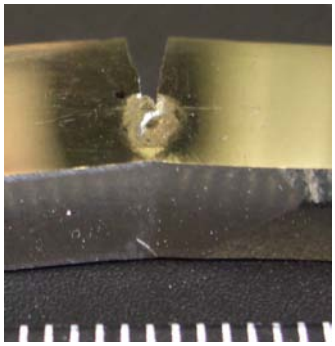

Figure B4 – A 5.3-mm-thick sample of the alloy DH3 directly from the arc melter without semi-solid processing. Crack arrest is still observed but with lower resistance to fracture. The measured value of K_{1C} is 103.5 MPa $m^{1/2}$, which satisfies the ASTM requirement for thickness. The toughest monolithic BMGs have K_{1C} that doesn't exceed ~ 50–60 MPa $m^{1/2}$. This demonstrates that even with uncontrolled microstructures, BMG composites are approximately twice as tough as monolithic ones.

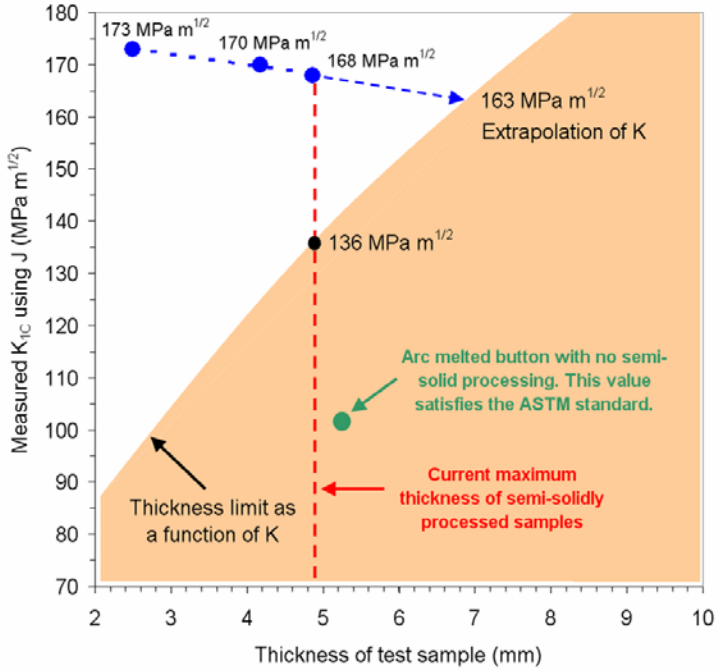

Figure B5 – Plot of K_{1C} (using the J-Integral method) as a function of sample thickness. The blue values represent invalid measurements due to sample thickness and the pink area represents valid ASTM standard thicknesses. The BMG composite DH3 directly from the arc melter is shown with the green value. Although not rigorous, our extrapolation indicates that K_{1C} will likely be ~ 163 MPa $m^{1/2}$, lower than the 173 MPa $m^{1/2}$ that we reported in Chapter 4. However, both values are estimations. Regardless, the fracture toughness of the new composites seems to exceed engineering titanium alloys and approaches toughened steels.

Appendix C (Miscellaneous Data)

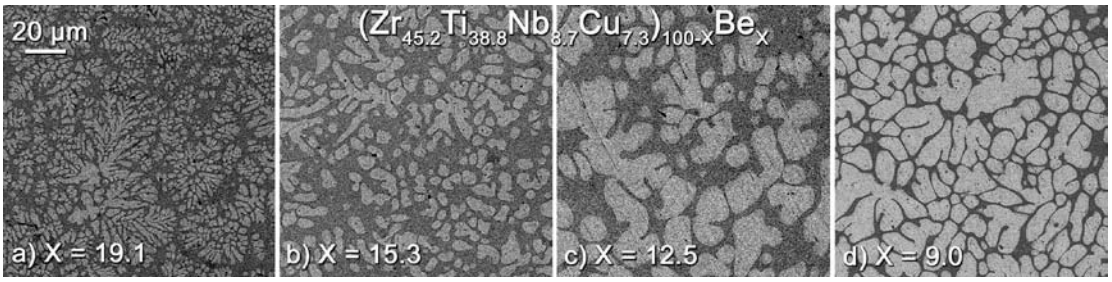

Figure C –. Backscattered SEM micrographs showing systematic variation of the at. % of Be, X, with (a) X = 19.1, (b) X = 15.3, (c) X = 12.5, and (d) X = 9. The dendrites are the lighter contrast and the glass matrix is the darker. EDS analysis was used detect the composition of the dendrite and a combination of computer assisted image analysis and DSC scans were used to estimate the volume fraction of dendrites. The alloys DH1–5 have 41%, 52%, 67%, 76%, and 80% β-phase by volume, respectively. Phase separation occurs because Be is not soluble as is b.c.c. titanium or zirconium. One might think that heterogeneous nucleation would cause the glass-forming phase to crystallize, however there are no stable Be phases that could form.

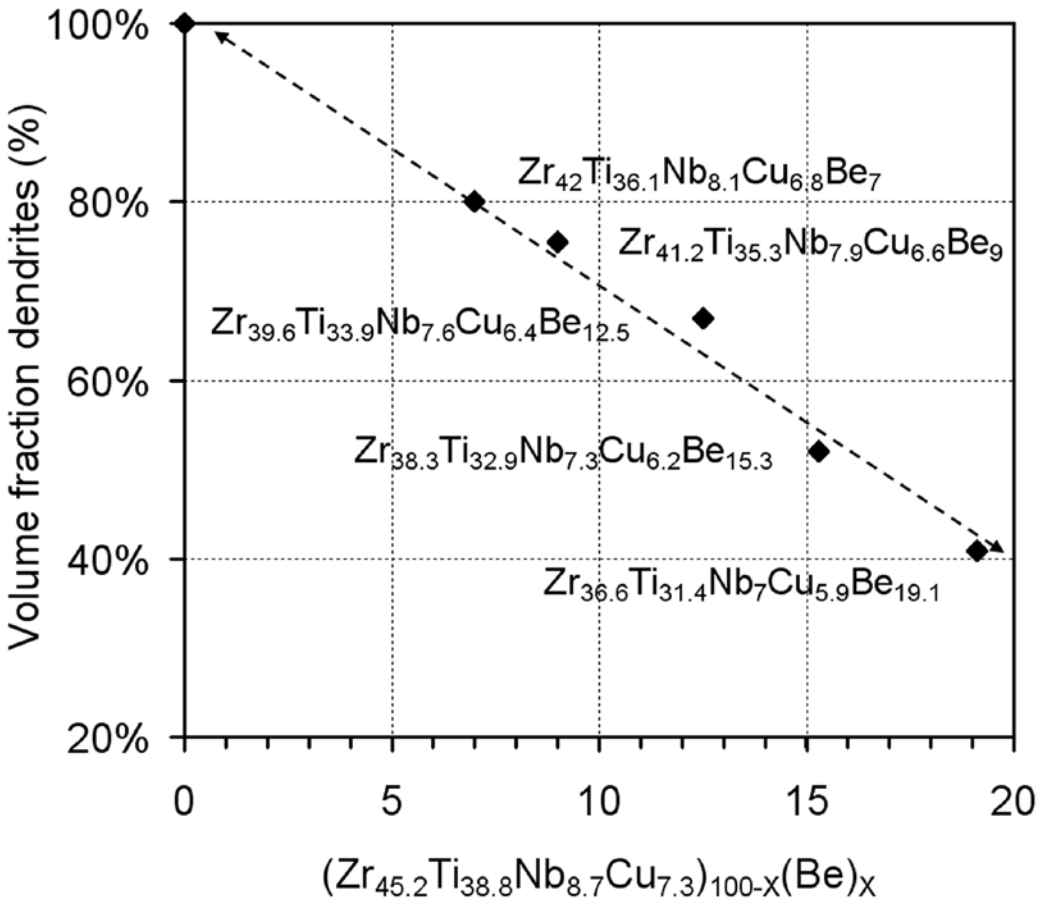

Figure C2 – A plot of volume fraction of β-phase dendrites versus at% of Be, X, in $(Zr_{45.2}Ti_{38.8}Nb_{8.7}Cu_{7.3})_{100-X}(Be)_X$ for 5 alloys. From the plot, it is clear that the volume fraction of β-phase follows an approximately linear trend from 40–100%. This indicates that the microstructure and mechanical properties of these alloys can be controlled by varying a single component, Be, even though both Cu and Be favor the glass matrix over the dendrite. Increasing the volume fraction of β-phase has been shown to increase fracture toughness and tensile ductility while decreasing yield strength.

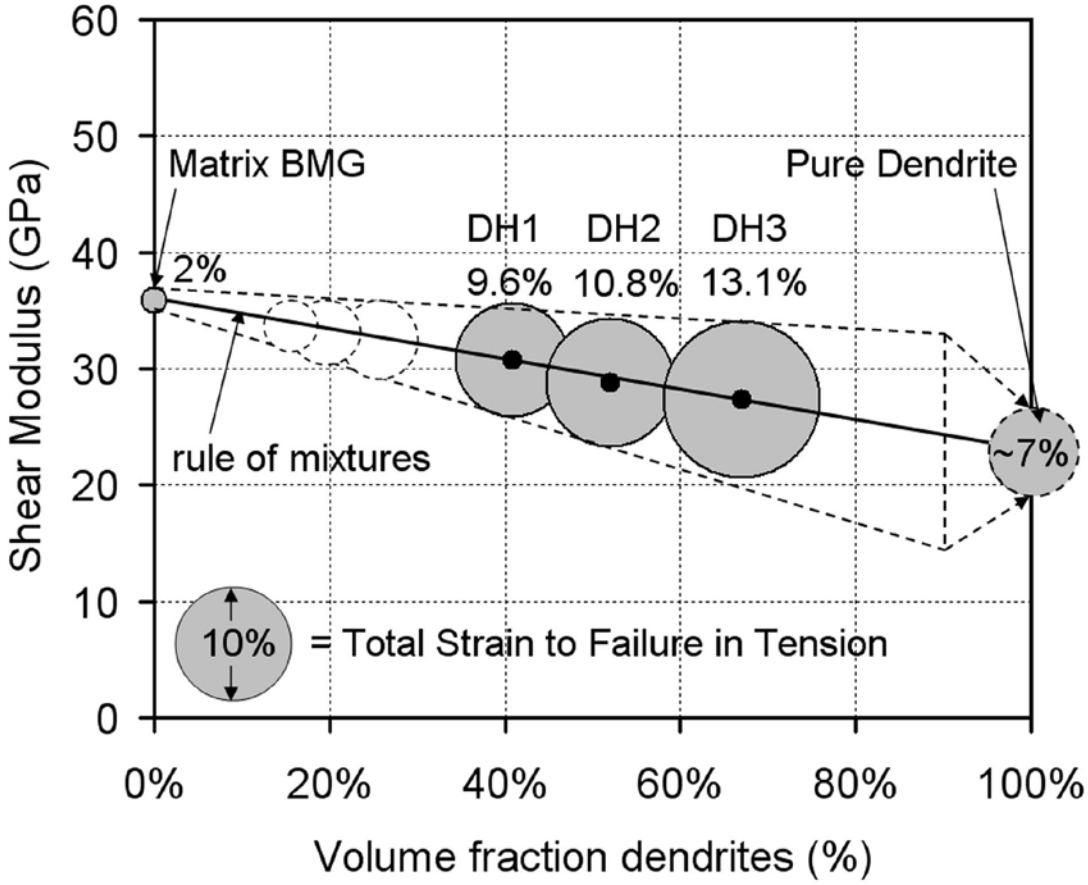

Figure C3 – Schematic plot of shear modulus versus volume fraction of β-phase dendrites for the alloys DH1–3. The black line indicates a rule of mixtures average between BMG matrix and the shear-soft dendrites. The diameter of the circles represents the total strain to failure during room temperature uniaxial tension testing. The dashed lines are estimations of the total strain to failure of alloys that are not shown. The total strain to failure is typically ~ 2% for metallic glasses and ~ 7% for the dendrite material. The dendrites in the composites suppress tensile instability and limit shear band extension, allowing for total strain to failure that is larger than the pure dendrite material (9.6%, 10.8%, and 13.6% for DH1–3, respectively).

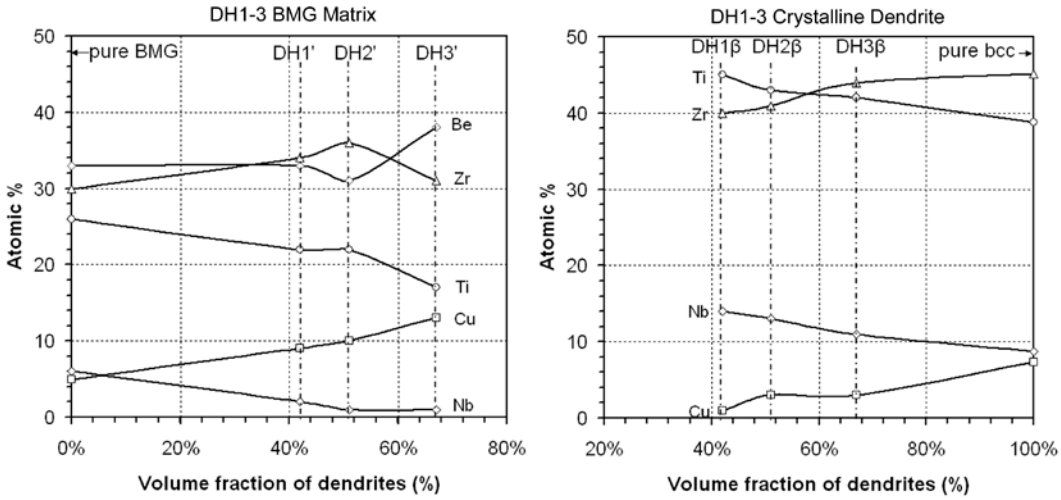

Figure C4 – Plots of atomic percentage versus volume fraction of dendrites to illustrate the compositional differences obtained during chemical partitioning for the dendrites and glass matrix of the alloys DH1–3. The dashed trend-line for the alloys DH1–3 is useful for estimating both the pure β-phase alloy and the parent BMG of this system. From the plot, the dashed line indicates that if the glass phase were removed, the resulting alloy would be similar to $Zr_{45.2}Ti_{38.8}Nb_{8.7}Cu_{7.3}$, representing X = 0 the plot. The trend also predicts a BMG $Zr_{30.4}Ti_{26.1}Nb_{5.9}Cu_{4.9}Be_{32.7}$ as the parent glass matrix, similar to the original BMG $Zr_{35}Ti_{30}Cu_{8.25}Be_{26.75}$ with ~ 6% Nb and increased Be. EDS analysis was used on the alloys DH1–3 to determine the composition of the β-phase and the glass matrix. For each alloy the atomic percentage of the constitutive elements is plotted as a function of the volume fraction of dendrites with DH1'–3' (DH1β–3β) representing the glass matrix (dendrites) of the alloys DH1–3. The plot illustrates how the composition of the glass matrix and the dendrites change relative to the estimated pure glass and pure dendrite. The compositions of the dendrites follow a clear trend starting from the pure β-phase alloy $Zr_{45.2}Ti_{38.8}Nb_{8.7}Cu_{7.3}$. With decreasing volume fraction of β-phase the dendrites favor Ti over Zr, becoming Ti-rich at ~ 56%. Thus the alloys DH1 and DH2 have Ti-rich dendrites while the alloy DH3 has a Zr-rich dendrite. Nb content steadily increases from the pure β-phase material to DH1, while Cu sharply drops to ~ 1 at%, where it remains for all three alloys. As an estimation it can be said that the composition of the dendrite for DH1-3 is a shear-soft (G ~ 23 GPa) alloy of Zr-Ti with ~ 15 at% Nb. The composition of the glass matrix does not follow such a clear trend, however. The at.% of Be and Zr remain relatively constant between 30-38% while the Ti (Cu) content decreases (increases) as the volume fraction of β-phase approaches 70%. Analogous to the lack of Cu in the β-phase material, the Nb typically has ~1 at% in the glass matrix. As an estimation, the glass matrix for DH1–3 is a Zr-Ti-Cu-Be BMG with typically ~ 10 at% Cu. This implies that the glass matrix should exhibit some of the same beneficial properties as were discovered in $Zr_{35}Ti_{30}Cu_{8.25}Be_{26.75}$ (large supercooled liquid region and high fracture toughness). Note that this plot is an estimation and there is likely an error of about 5% in the measured values.

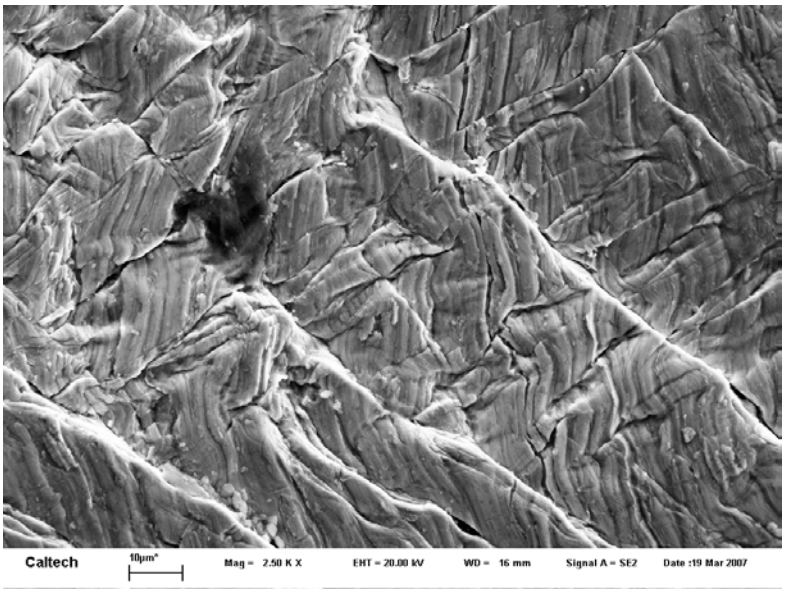

Figure C5 – SEM micrograph from the tensile surface of the composite DH3 after testing. A hierarchy of shear bands is visible with primary bands ~ 40 μm wide, secondary bands ~ 10μm wide, and tertiary bands < 2 μm wide. This is among the finest shear band spacing ever observed in BMG research and it is from a tension test, not a compression test.

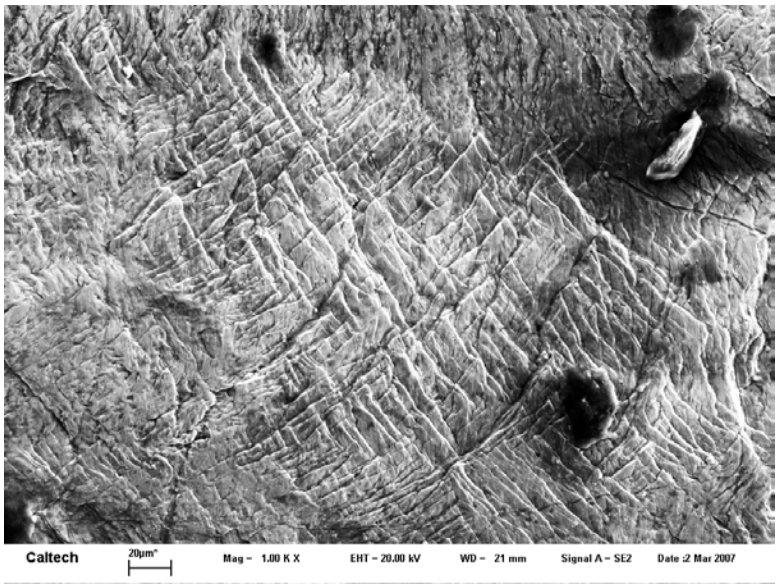

Figure C6 – SEM micrograph from the tensile surface of the composite DH2 after testing. A dense pattern of shear bands is visible, indicating a large amount of plastic strain has occurred.

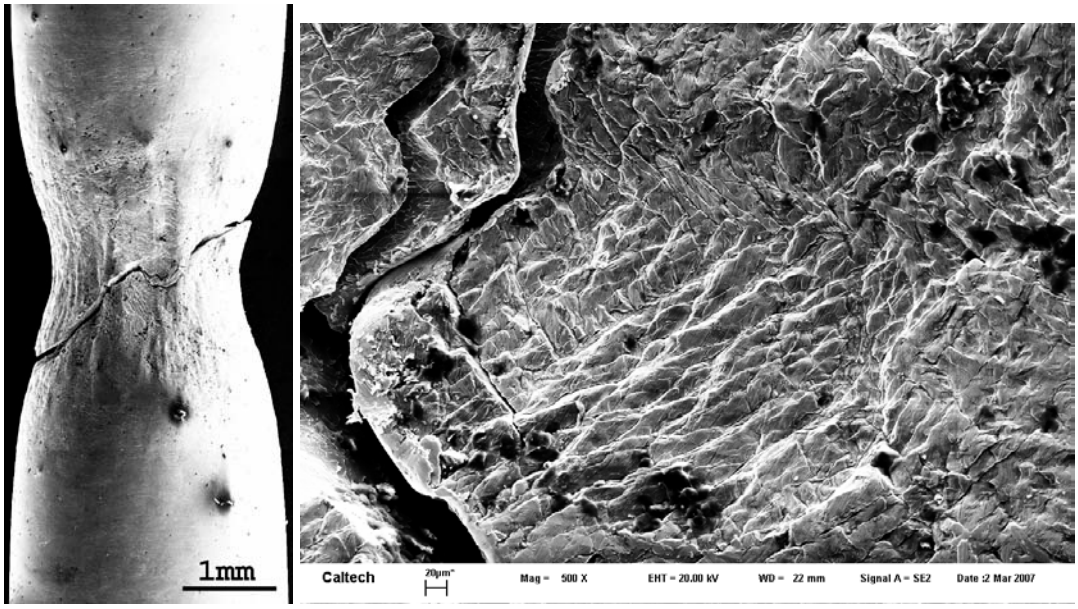

Figure C7 – (left) Extensive necking during a tension test of the in-situ composite LM2A2 from S.Y. Lee's Caltech thesis (2005) produced by the semi-solid processing method. The alloy displays ~ 13.5% tensile ductility and a dense "stair-step" shear band pattern (right). The semi-solid processing has more than doubled the tensile ductility reported in S.Y. Lee's thesis for this alloy.

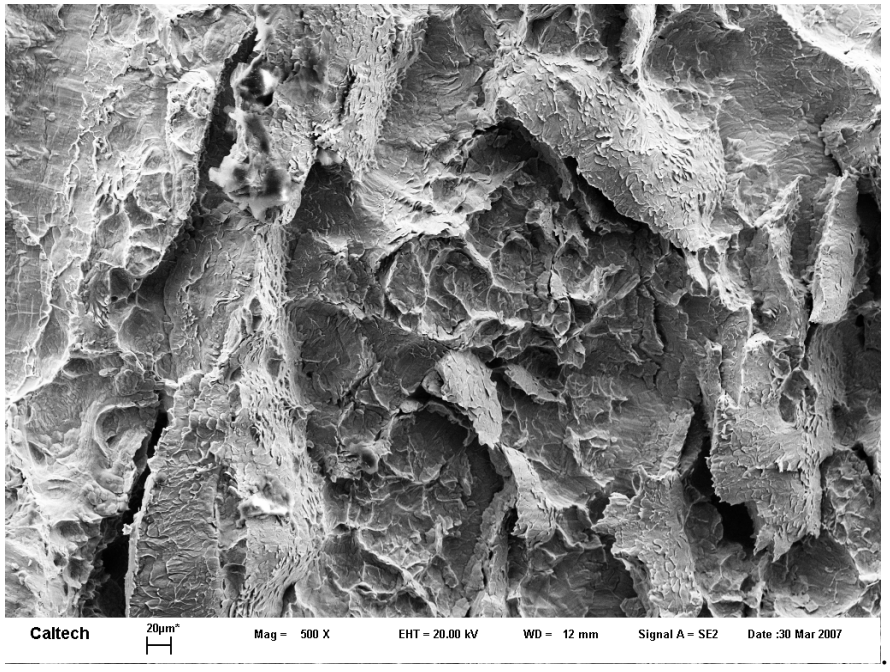

Figure C8 – SEM micrograph from the fracture surface of a Charpy impact test in DH3. Despite the high strain-rate test, the alloy has a jagged fracture, indicative of high toughness.

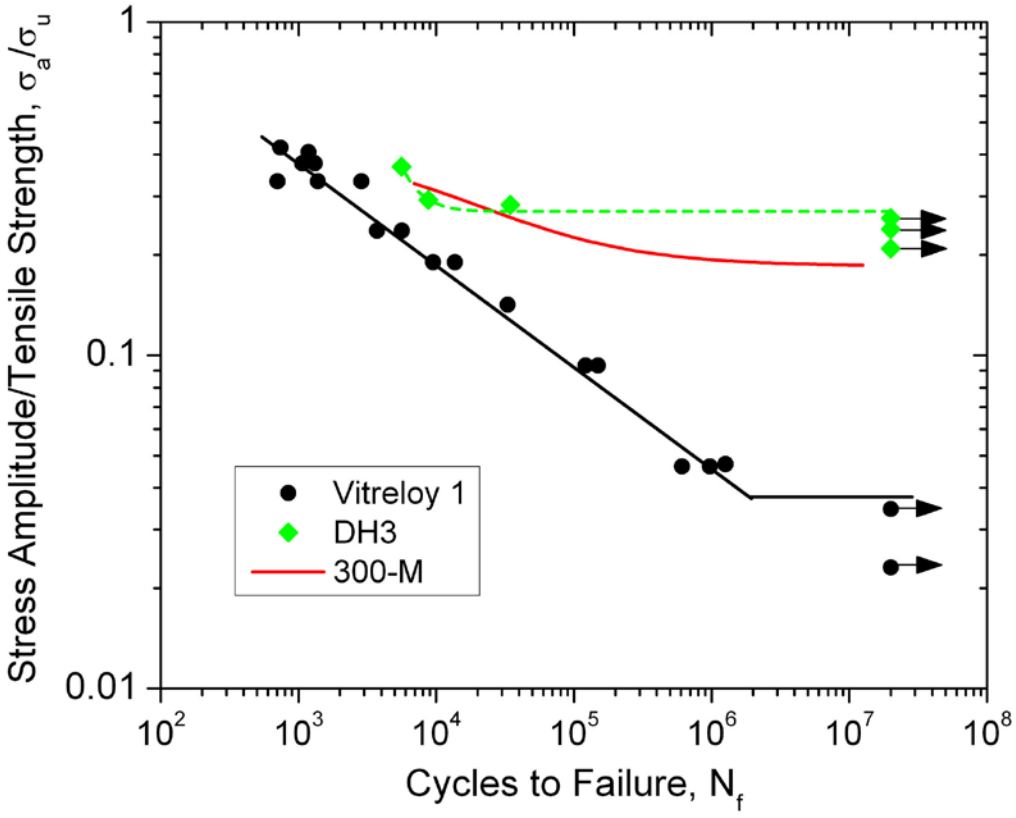

Figure C9 – Fatigue life data for the alloy DH3 compared with the monolithic BMG Vitreloy 1 and fracture-resistant 300-M steel. This work was completed at Lawrence Livermore National Laboratory by M. Launey in collaboration with our group. The preliminary fatigue data show that DH3 has a higher fatigue limit than high strength steel. Fatigue is among the most important measurements for structural materials and the alloy DH3 has among the highest value of fatigue for any known structural engineering materials.

Figure C10 – An example of how tension tests were produced from porosity-free ingots by machining. More recent tension samples were produced by cutting the cylindrical ingot into a square bar and then lathing a cylindrical gauge section 3 mm in diameter and 15 mm long into it. Then the specimens were loaded into large clamping grips on the load frame. The geometry allowed the grips to hold a flat part of the sample while the gauge section allowed for a standard ASTM cylindrical tensile test.

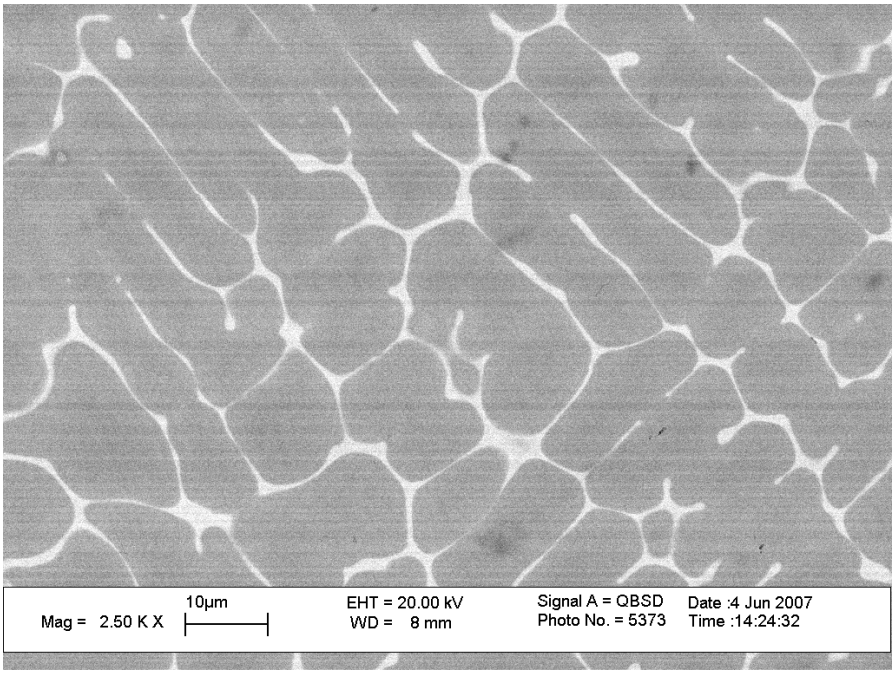

Figure C11 – Backscatterd SEM micrograph of a metallic glass reinforced alloy (MGRA), which is an alloy with < 10% glass phase by volume. The dendrites remain isolated and the glass matrix is still continuous, although it now forms into ~1 µm thick webs. This alloy still has a substantially higher strength than the pure dendrite material, ~ 900 MPa vs. ~ 600 MPa.